PhD 14094

DIELECTRIC MEASUREMENTS FOR ORGAN CRYOPRESERVATION

Timothy Paul Marsland

UNIVERSITY
LIBRARY
CAMBRIDGE

A dissertation submitted to the University of Cambridge
for the degree of Doctor of Philosophy

Darwin College
Cambridge

January 1986

Declaration

To the best of my knowledge, the work contained in this dissertation is original except where acknowledgement to others is given. It is the result of my own work and contains nothing which is the outcome of work done in collaboration. The work has not been submitted, in part or whole for any other university degree of diploma. Permission is granted to consult or copy the information contained herein for the purpose of private study, but not for publication.

T P Marsland

Cambridge, January 1986

Acknowledgements

I should like to thank the following individuals:

My supervisor Dr. Stan Evans, for his tireless guidance, support and encouragement throughout the period of my research.

Dr. A C Metaxas for the loan of the Network Analyzer.

Dr. Sylvia Fitton Jackson for arranging financial support.

The workshop staff of the ECR laboratory, especially Mr. Peter Mackenzie who made all the sample holders and probes.

My fellow research students, in particular Wai-Kwong Yeung, Howard Reader, Fannian Kong.

Dr David Pegg and his colleagues in the MRC Cryobiology Group for all their time, help, and suggestions.

The members of the Cambridge Speech Group for use of their word processing facilities.

Keywords: **dielectric measurements, organ preservation, cryopreservation, hyperthermia, microwave measurements, time domain measurements**

Summary

The aim of this area of research is to provide techniques which would allow long-term low temperature storage and subsequent transplantation of human organs, such as the kidney. A major difficulty in organ cryopreservation is that of obtaining rapid warming of the frozen tissue, whilst maintaining a uniform temperature profile. Before cooling, the organ is perfused with a 'cryoprotectant', a solution which reduces freezing injury. Warming rates that can be achieved by thermal conduction cannot exceed about 1K/min without damaging the exterior of the organ. Experimental evidence from a range of cell and organ systems suggest that warming should be much more rapid. One proposed warming technique employs dielectric heating using electromagnetic energy at microwave frequencies. Crucial to the design of any such rapid warming system are the electrical properties of the material to be heated.

This dissertation describes two measurement systems that have been developed for measuring the electrical properties of cryoprotectants and of perfused rabbit kidney tissue. Dielectric measurements were made with both time and frequency domain instrumentation, over a frequency range of 50MHz to 2.6GHz, and a temperature range of -30°C to +20°C. The more successful of the two systems uses an open-ended coaxial probe with a new, simplified, error correction and calibration technique.

The measurements show that electrical properties of perfused tissue are heavily influenced by those of the cryoprotectant in this frequency range. A new low conductivity cryoprotectant has been developed which has more favourable electrical properties. There is a strong suggestion that using such a cryoprotectant, rapid warming may become a practical proposition around 430MHz.

Contents

Notation, Abbreviations and Glossary

Notation

Radius of spherical discontinuity	a
Network Analyzer calibration constants	A_f, A_m, A_p, B_f, B_m, B_p
Magnetic flux density	$\underline{B}$
Velocity of light in free space	c
Specific heat capacity at constant pressure	c_p
Geometrical capacitance of simple applicator	C_a
Fringe field capacitance inside probe	C_f
Scattering matrix to represent connectors	$\underline{C}$
Fringe field capacitance of the open-ended probe	C_o
Length of strip-line sample holder	d
Connector model parameter	d_c
Electric displacement	$\underline{D}$
Power Penetration depth	D_p
Electric field	$\underline{E}$
Scattering matrix to represent error network	$\underline{E}$
Frequency corresponding to data index i	f_i
Frequency of loss peak for a Debye relaxation process	f_p
Normalised conductance of open-ended probe	G_n
Radiation Conductance of open-ended probe	G_o
Magnetic field	$\underline{H}$
Time domain excitation waveform	$i(t)$
Current density	$\underline{J}_f$
Thermal conductivity	k
Error sensitivity for ith measurement of ρ	K_i
Magnetic Polarization	$\underline{M}$
Number of summations for signal averaging	N_a
Scattering matrix for Network Analyzer imperfections	$\underline{N}$
Dipole moment of group of charges	$\underline{p}$
Power deposition per unit volume	P
Plane wave incident power	P_{inc}

Electric Polarization	$\underline{P}$
Scattering matrix to represent open-ended probe	$\underline{P}$
Charge	q
Radial coordinate	r
Normalized impedance of empty sample holder	r
Normalized radius	r'
Impulse reflection coefficients for materials 1,..3	$r_1,..r_3$
Reflection coefficient difference, $\rho_i - \rho_j$	r_{ij}
Connector model parameter	r_c
Measured impulse reflection coefficient	r_m
Reflection and transmission impulse scattering responses	s_{11}, s_{21}
Scattering parameters of microwave two-port network	S_{11}, S_{21}
Measured values of S_{11}, S_{21}	S_{11m}, S_{21m}
True values of S_{11}, S_{21}	S_{11t}, S_{21t}
Time	t
Normalized time	t'
Warming time from T_o to T_h	t_h
Temperature, Kelvin	T
Initial temperature	T_o
Final temperature	T_h
Temperature where maximum power is transferred	T_x
Reflected and transmitted time domain waveforms	w_{11}, w_{21}
Warming rate	W
Initial warming rate at temperature T_o	W_o
Position vector	$\underline{x}$
Normalized admittance of probe for material 1,..4,m	$y_1,..y_4,y_m$
Admittance	Y
Admittance of open-ended probe in contact with material of permittivity ε_i, i = 1,..4,m	Y_i
Admittance of capacitive applicator	Y_L
Characteristic admittance of TEM guiding system	Y_o
Source admittance	Y_s
Admittance of loaded applicator at temperature T	Y_t
Admittance of loaded applicator at temperature T_x	Y_x
Characteristic impedance of TEM guiding system	Z_o
Thermal diffusivity	α
Cole-Cole dispersion parameter	α_{cc}

Temperature coefficient of power absorption	β
Cole-Davidson dispersion parameter	β_{cd}
True reflection coefficient of one port network	Γ
Error corrected reflection coefficient	Γ_m
Activation enthalpy	ΔH
Dielectric decrement of multiterm Debye dispersion	Δ_i
Uncertainty in S_{11} and S_{21}	ΔS_{11}, ΔS_{21}
Local temperature perturbation	ΔT
Error in ith reflection coefficient: magnitude and phase	δm_i, δp_i
Upper bound on magnitude and phase errors	δM, δP
Error in measured permittivity ε_m	$\delta \varepsilon_m$
Error in ith reflection coefficient	$\delta \rho_i$
Permittivity of free space	ε_o
Relative permittivity of reference materials	$\varepsilon_1, .. \varepsilon_4$
Effective dielectric loss	ε_e''
Relative permittivity of dielectric filling of TEM guide	ε_{fill}
Relative permittivity of lossless filling material	ε_i
Relative permittivity of measured material	ε_m
Real and imaginary parts of ε_m	ε_m', ε_m''
Relative permittivity	ε_r
Real and imaginary parts of ε_r	ε_r', ε_r''
Complex relative permittivity	ε_r^*
Static permittivity (dispersion parameter)	ε_s
High frequency permittivity (dispersion parameter)	ε_∞
Complex permittivity of material at temperature T	ε_t^*
Complex permittivity of material at temperature T_x	ε_x^*
Normalized power absorption	η
Temperature in celsius	θ
Temperature distribution (Appendix 1)	θ
Magnetic permeability of free space	μ_o
Relative permeability	μ_r
Density (Appendix 1)	ρ
Reflection coefficient	ρ
Charge density	ρ_f
Measured reflection coefficient of material i=1,..4	ρ_i
Measured reflection coefficient	ρ_m
Effective conductivity	σ
DC conductivity	σ_{dc}

Complex conductivity	$\sigma^{\dagger}$
Effective conductivity at temperature T	σ_t
Effective conductivity at temperature T_x	σ_x
Relaxation times (dispersion parameters)	τ, τ_i
Temperature distribution	ϕ
Electric susceptibility	χ_e
Angular frequency	ω

Abbreviations

ADC	analogue to digital converter
CPA	cryoprotective agent (cryoprotectant)
DAC	digital to analogue converter
DFT	discrete Fourier transform
DMSO	dimethylsulphoxide (Me_2SO)
EM	electromagnetic
FWHM	full-width at half maximum
ISM	industrial, scientific and medical
M	concentration, mol/litre
TE, TM	transverse electric, transverse magnetic
TEM	transverse electromagnetic
PLL	phase-locked loop
VTO	voltage-tuned oscillator

Glossary

applicator Apparatus used to 'apply' an electromagnetic field to a volume of material e.g. a frozen organ.

cryoprotectant Additive to the preservation solution that is perfused through an organ before and during cooling

Network Analyzer An instrument which measures the scattering parameters of microwave networks.

Preface

Chapter 1 identifies the need for organ cryopreservation technology, outlines some of the biomedical problems involved, and reviews previous attempts at rapid warming. Crucial to the design of any electromagnetic rapid warming system, are the dielectric properties of the material to be heated. Chapter 2 explains how dielectric properties control rapid warming, and chapter 3 reviews previous measurements on similar materials, and measurement techniques.

Chapter 4 describes the development of a time domain dielectric measurement system based on a strip-line sample holder. Chapters 5 and 6 describe the theory and practical details of the frequency domain dielectric measurement system which was used to perform the majority of the dielectric measurements on tissue and cryoprotectants. The measurements themselves are described in chapter 7, concluding with recommendations concerning a frequency and cryoprotectant suitable for rapid and uniform warming, and suggestions for further work.

Appendix 1 is an analytical investigation of some of the thermodynamic problems encountered in rapid warming. Appendix 2 is an inventory of materials used, whilst appendix 3 describes the two digital data recorders used for the time and frequency domain measurement systems.

Chapter 1

Low Temperature Preservation of Organs

The work described in this dissertation is intended to be the basis for the design of an experimental system for the electromagnetic rewarming of cryopreserved organs, such as the kidney. This chapter describes some of the biological and biophysical problems encountered in the cryopreservation of cell suspensions and organs in order to explain the need for the development of rapid warming technology, and to identify relevant aspects of the engineering design.

First, the underlying need for long term organ preservation is identified. Sections 2 and 3 summarize the results of a large body of experimental work on the low temperature preservation of cell suspensions, and of whole organs. These summaries are based on the reviews by Burdette and Karow (1978a), Farrant (1980), Pegg and Jacobsen (1983), and Jacobsen and Pegg (1984a). Section 4, reviews some of the techniques for performing rapid warming of cryopreserved organs, and discusses some of the specific engineering problems to be addressed in greater detail in later chapters. Finally, section 5, reviews several recent attempts to rewarm cryopreserved organs using electromagnetic techniques.

1. The Need for Long Term Organ Preservation

Because of recent advances in immunology and surgical techniques, organ transplant surgery is becoming increasingly commonplace; kidney transplantation is a particularly successful example. However, there is a severe shortage of suitable donor organs. A recent survey of 26 of the 28 renal transplant units in the United Kingdom by Sells et al. (1985) quantifies the problem.

In November 1983, 4792 patients were receiving dialysis treatment, and 2393 were on the waiting list for a kidney transplant. During the period 1980-1984, the average theoretical

UNIVERSITY LIBRARY CAMBRIDGE

maximum number of new patients considered suitable for transplant was 2259/year, however, an average of only 1127/year were actually performed because of the scarcity of suitable donor organs. The situation in the rest of Europe, the United States, and Japan is similarly bleak.

The most immediate need is for more donors; this is an ethical and political problem, not a technological one. However the situation would be considerably improved if it were possible to construct 'organ banks' run by a national organization where donor organs could be stored for long periods, possibly months or even years. Even storage periods of a few weeks would make it possible to give the recipient donor-specific treatment to make him tolerant of that particular donor's organ. Organs that are currently required include kidney, heart, liver and pancreas; more would follow if prolonged organ preservation became a practical proposition.

2. Cryopreservation of Cells

To understand some of the basic problems of organ cryopreservation, it is helpful to consider the problems encountered in cell cryopreservation. Techniques for the cryopreservation of cells are well developed and quite successful for many cell types[†] including red blood cells, platelets, lymphocytes and spermatozoa. Most cryopreservation procedures for cells involve the following five stages:

a) Suspend the cells in a 'cryoprotectant' solution.

b) Cool, from physiological temperature to the storage temperature.

c) Store at low temperatures, e.g. in liquid nitrogen.

---

† Numerous examples are documented in Karow A M and Pegg D E, "Organ Preservation for Transplantation" (see bibliography).

d) Rewarm, from the storage temperature to physiological temperature.

e) Remove the cryoprotectant by re-suspending the cells in a suitable culture medium.

The cryopreservation protocol, which effectively describes the details of these five stages, is usually optimized for the survival of a particular cell type, however, there are some important general observations that can be made. As an example, the next section examines the behaviour of a population of isolated mammalian cells suspended in a (water based) culture medium under different cooling and warming rates.

2.1. Cooling and Cooling Rates

Most cell types can be cooled from +37°C to 0°C without injury, rapidly or slowly, though there are some that show sensitivity to rapid cooling. This sensitivity, often called 'cold shock', is proportional to the cooling rate and can best be avoided by slow cooling in this temperature range, although the mechanisms of damage are poorly understood (McGrath 1985).

Although the idea is quite attractive, in general, unfrozen cells cannot be preserved successfully at low temperatures. They are unable to maintain vital transmembrane ionic gradients because of the disproportionate reduction in ion pump activity compared with passive ionic diffusion. So, the temperature must be reduced still further, until this diffusion is stopped.

As the temperature drops, ice nuclei form in the extracellular space; there is a greater tendency for the intracellular contents to supercool. The concentration of the solutes in the external medium rises, and cells lose water by osmotic shrinkage. Most cells can tolerate this shrinkage; however, if the cooling rate is too slow, cells are damaged by exposure to high intra and extracellular concentrations of solutes. Another consequence of slow cooling is the effect of the increased permeability of the membrane to cations, leading to

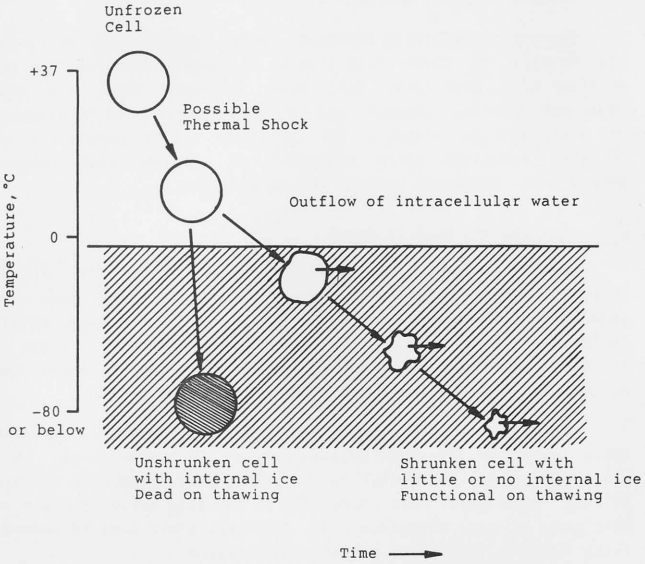

Figure 1.1 Influence of cooling rate on cell survival

If cooling is slow, extracellular ice is formed, and water is removed from the cells osmotically; the cells shrink but survive. If cooling is rapid, water does not have sufficient time to escape, intracellular ice is formed and the cells are dead on thawing. After Farrant (1980).

'solute loading' during freezing.

If cooling is too rapid, so that it does not allow significant osmotic shrinkage of cells, then the cellular water will be unable to escape, and intracellular ice will be formed. After such treatment, most cells are dead on thawing, although there is evidence that the injury only becomes manifest during rewarming since different survival rates are observed when warming conditions are altered. Figure 1.1 summarizes the problems encountered in cooling and freezing cells.

2.2. Preservation at Very Low Temperatures

There is ample evidence that deterioration is imperceptible at -196°C, the boiling point of liquid nitrogen, which is the usual temperature chosen for storage. The only limit seems to be the slow accumulation of natural radiation damage which, even without shielding, would take many thousands of years to reach acute levels (Ashwood-Smith 1980). So prolonged preservation *per se* is merely a refrigeration problem.

2.3. Cryoprotectants

The solution in which the cells to be cryopreserved are suspended contains many additives, including cryoprotectants or 'cryoprotective agents' (CPAs). The function of the cryoprotectant is to protect the cells during cooling and rewarming - i.e. to reduce the damage. There are many different CPAs, chosen for many different reasons, though they seem most effective against slow cooling injury. Although the exact mechanisms of action are still unclear, the cryoprotectant essentially reduces the rate of rise of electrolyte concentration with decreasing temperature. Generally, a CPA must be highly soluble in water, and be of low toxicity. The CPAs that seem to be most popular in the literature are dimethyl sulphoxide (DMSO[‡]) and glycerol. Other CPAs that have been used include methanol, propanediol, and a range of polymers such as dextran, hydroxyethyl starch and polyvinylpyrrolidone (PVP).

‡ An alternative abbreviation is Me_2SO

The final cryoprotectant solution is usually a fairly concentrated solution of one of the above compounds e.g. 2M glycerol, together with a host of other compounds. The solution contains various ions e.g. Na^+, K^+ and Cl^-, together with other compounds e.g. sugars and steroids, so as to produce the same concentration of impermeant species across the cell membrane. The exact recipe used is 'handed down' from experimenter to experimenter - with occasional empirical modifications. Biologists are understandably reluctant to make revolutionary changes to the composition of existing cryoprotectant solutions because of the expense, both in time and other resources, of a proper evaluation of a completely new solution.

2.4. Warming and Warming Rates

There is some evidence that slow warming is to be preferred if there has been slow cooling. This may be because more time is allowed for excess solutes to leave the cells (Pegg and Jacobsen 1983). As noted earlier, with rapid cooling there is a marked sensitivity to warming rate, and rapid warming is preferred. It is thought that the injury caused by slow warming is due to the redistribution and/or growth of ice during rewarming to larger intracellular crystals - a process generally known as recrystallization. One of the clearest findings of cryobiology is that recrystallization is very damaging to cells.

2.5. Interdependence of Parameters in Cryopreservation

From the discussion so far, it is clear that it is impossible to treat the freezing rates and thawing rates in isolation. A particularly striking way to illustrate this interdependence is given by Pegg et al. (1984). They describe experiments in which samples of human red blood cells, suspended in 2M glycerol, were exposed to a wide range of cooling and warming rates. The results of numerous such cryopreservation experiments were presented as a contour plot on which the contours represent lines of constant haemolysis (percentage killed). Figure 1.2 is a reproduction of their illustration.

Figure 1.2 Damage as a function of cooling & warming rates

Isohaemolysis contours for human erythrocytes frozen and thawed in 2M glycerol. The diagrams show results at two levels of cell packing: (a) a haematocrit of 2%, and (b) a haematocrit of 75%. From Pegg et al. (1984). (Haematocrit is defined as 100% x Total Cell Volume / Total Volume)

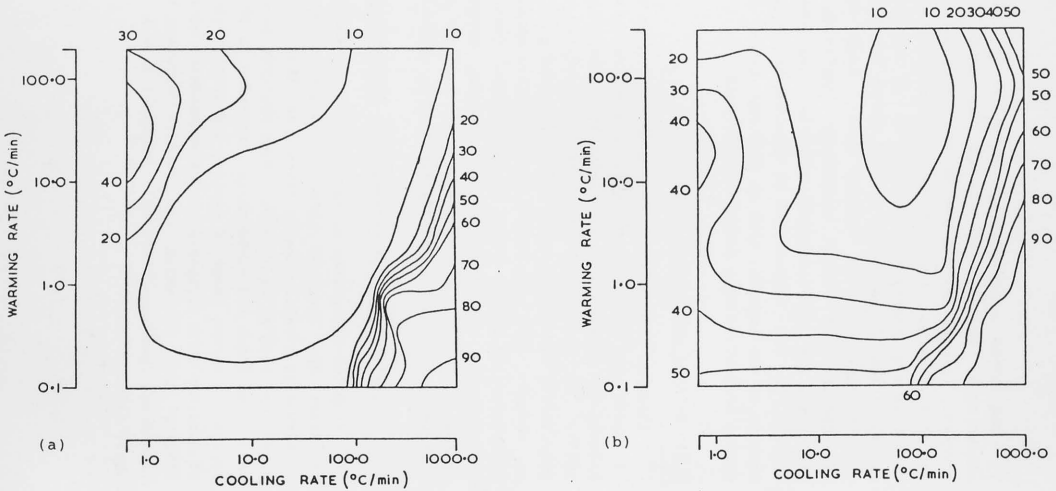

These two contour plots also illustrate the 'packing effect', which is particularly relevant to organ cryopreservation because a packed cell suspension can be thought of as a simple model of an organ. At low packing density, Figure 1.2a shows that, for these cells, survival will be better than 90% if the warming rate is about one tenth of the cooling rate, over three decades of cooling rates. However, at the high packing density the picture changes drastically. Figure 1.2b shows that better than 80% survival can only be achieved with both warming rates and cooling rates between 10 and 100K/min. If warming can be made as rapid as 200K/min, cooling rates as low as 1K/min can be tolerated.

As well as cooling rate, warming rate and the packing effect, the damage contours depend on many other factors, including cryoprotectant composition. The procedures used for the introduction and removal of the cryoprotectant, which may be quite toxic at physiological temperatures, also affects survival rates.

3. Cryopreservation of Organs

3.1. Hypothermic Preservation

Current low temperature preservation techniques allow kidneys to be preserved hypothermically (i.e. above 0°C) for up to 3 days, and heart and liver up to 48 hours. This is obviously too short a period to allow organ banking; it is also too short a period to fully utilize the recent advances in immunology which allow improved donor-recipient matching (Southard and Belzer 1983). Cryogenic organ preservation would allow virtually unlimited storage periods. Cryopreservation of cell suspensions is now routine, but a successful, reproducible, storage protocol has yet to be found for whole organs.

3.2. Difficulties Inherent in Organ Cryopreservation

An organ such as the kidney, is a highly organized population of cells, of many different types and functions. An initial approach to the study of organ cryopreservation is to extrapolate

Figure 1.3 Section through a hypothetical mammalian kidney

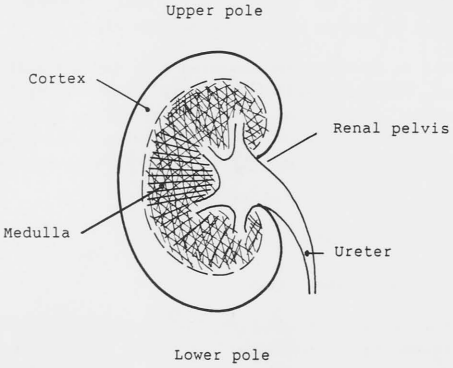

Renal vasculature omitted

	Length (mm)	Width (mm)	Thickness (mm)	Reference
Human	90–150	40–50	30 approx.	Hollinshead 1971
Dog	60–90	40–50	30–40	Christensen 1979
Rabbit	30–40	20–30	20–25	This work

from the related problems of the cryopreservation of cell suspensions. Note that it is unlikely that the problems, or the mechanisms of damage, will be exactly similar. The mere proximity of cells to one another may render the extrapolation from dilute cell suspensions invalid (Pegg 1981). Also, the different cell types in the organ may require different cryopreservation protocols - it may not be possible to obtain high recovery rates for all cell types.

Even if cell recovery is 100%, the organ will not function if the extracellular architecture has been destroyed. An organ is not just a compacted cell suspension - the highly complex extracellular architecture, e.g. the numerous capilliaries and intercellular connections, is also essential to form and function.

3.3. Choice of Model System

Human organs cannot be used for experimentation at this early stage in the development of cryobiology, for obvious reasons. Instead, organs from animals such as the rabbit or dog are used. The canine kidney model is useful in that the physical size of the organ is closer to the human kidney, however, the rabbit is a much more convenient experimental animal than the dog. Figure 1.3 is a section through a hypothetical mammalian kidney, which defines some of the nomenclature used, together with the approximate dimensions of human, dog and rabbit kidneys.

3.4. Choice of Cooling Rate

It is thought that the optimal cooling rate for organ preservation is likely to be very slow by single cell standards, in order to avoid internal freezing - probably less than 0.1K/min (Pegg and Jacobsen 1983, Jacobsen et al. 1984b). This is really quite fortunate, because fast cooling rates are difficult to achieve in whole organs. Cell suspensions can be packed into any convenient shape to obtain high surface area to volume ratios allowing rapid conductive heat transfer with small thermal gradients. However, in whole organs, the surface area to volume ratio is less than 1/cm and rapid cooling produces large

temperature gradients. In experiments using a canine kidney model system, Pegg et al. (1978) found that cooling rates of less than 3K/min produced peak temperature gradients of about 10K/cm. There is no direct evidence that such gradients are damaging in themselves, though their very existence implies a spectrum of cooling rates. Additionally, if the temperature gradients are severe, differential thermal contraction, will lead to damaging mechanical stresses (Rubinsky et al. 1980).

In practice, cooling is performed using various combinations of conduction and convective heat transfer, for which the technology is already well developed (Burdette 1981).

3.5. Choice of Cryoprotectant

Generally, highly concentrated solutions of CPAs seem to lessen the dependence of survival on cooling rate. In order to get such a concentrated CPA solution into intimate contact with the cells throughout the organ in a reasonable time, the vascular system of the organ must be used. Consequently the cryoprotectant must be able to get through the capilliaries and across the plasma membrane rapidly, so high molecular weight compounds e.g. PVP are probably unsuitable. Much experimental work remains to be performed to determine a suitable 'recipe' for the cryoprotectant solution, and a suitable protocol for its addition to, and removal from the organ. Attempts to provide predictive mathematical models of this protocol that would reduce the amount of experimentation required are still at an early stage of development (Rubinsky and Cravalho 1982).

3.6. Choice of Warming rate

The general observations in section 2 concerning optimum cooling and warming rates for cell cryopreservation, suggest that organs that have been cooled slowly should be warmed slowly for best survival. However, the experiments on packed red cell systems with a glycerol based cryoprotectant by Pegg et al. (1984) suggest that damage may be minimized by rapid rewarming. Furthermore, most of the organ rewarming attempts by previous

workers seemed to produce better results with higher warming rates i.e. greater than 10K/min. However, Jacobsen et al. (1984b), in experiments on rabbit kidneys perfused with a 2M glycerol based cryoprotectant solution found that cooling at 1K/hr, followed by warming at 1K/min gave best results; higher warming rates (3.1K/min) were less effective.

For warming by thermal conduction, the surface area to volume ratio considerations still apply and limit the warming rate to perhaps 3K/min. Significantly higher warming rates have been achieved using electromagnetic fields; these experiments are reviewed in detail in a later section.

3.7. Optimum Cooling and Warming Rates

It seems likely that the interdependence of the cooling rate, warming rate and cryoprotectant composition will be even more complex than that of the red cell system illustrated in Figure 1.2. A large volume of experimental work is required, over a wide range of cooling and warming rates, to establish such contours for a particular cryoprotectant and organ system.

3.8. Amorphous Solidification - Vitrification

A different approach to organ preservation has been suggested by Fahy and Hirsch (1982, 1984) which is currently receiving much attention. On cooling to sufficiently low temperatures, highly concentrated solutions of most CPAs normally supercool and solidify (rather than freeze) into a non-structured, highly amorphous, glassy state. Even if substantial quantities of freezing nuclei are present, this glassy state can be obtained. At the glass transition, there is an abrupt cessation of diffusion; there are no ice crystals, no damaging osmotic shifts or concentrating of solutes. The only problem is perfusing the organ with a suitably concentrated cryoprotectant.

Fahy and Hirsch have shown that the CPA concentration needed to achieve 'vitrification' can be reduced by increasing the hydrostatic pressure; this is normally damaging to tissue -

fortunately many cryoprotectants are also baroprotective. Pressures of the order of 1000atm were found to allow a 10% reduction in the CPA concentration required.

Certain CPAs appear to be better than others for vitrification, in that lower concentrations are sufficient for the liquid to glass transition to occur (Fahy and Hirsch 1982). Glycerol appears to be one of the worst, and propanediol one of the best CPAs for these purposes. Another factor that promotes vitrification over ice formation is rapid (non-equilibrium) cooling.

Devitrification

At low temperatures, the rate of formation of ice nuclei is high, but the ice crystal growth rate is low (Hallett 1968). On warming, the situation reverses, the nuclei grow rapidly, so rewarming must be extremely fast to avoid the tissue damage these crystals provoke. This need for ultra-rapid warming is supported by experimental work by Rall and Fahy (1985) on a mouse embryo system. Their experiments were performed at atmospheric pressure, using a suitably concentrated cryoprotectant solution based on DMSO. The embryos were stored for periods from 1 to 30 days at -196°C. Rall and Fahy showed that, for this system, provided the warming rate was rapid i.e. 2500K/min, survival rates of over 83% could be achieved with cooling rates of 20K/min or 2500K/min.

4. Engineering Aspects Of Rapid Warming

There is considerable uncertainty as to what is a suitable preservation protocol for organs. Only approximate ideas about the introduction and removal of the cryoprotectant, which cryoprotectant to use, the rate of cooling, and the rate of warming are available. However, there is a strong suggestion from previous attempts at organ cryopreservation that rapid warming is required; indeed, rapid warming is the only way to recover organs that have been preserved by 'vitrification' (Fahy et al. 1984).

Rapid warming *per se* is not really a problem, although taking a 100g kidney from -80°C to +20°C at, say, 300K/min requires average heat transfer rates of the order of 1 to 2kW. The major difficulty lies in the requirement that warming should be *uniform* as well as rapid. If uniform warming cannot be achieved, organ survival is unlikely; at best, the range of warming rates implied will be detrimental to cell survival, at worst, the organ will be damaged by thermally induced stress, or burning. This requirement is difficult to achieve because of the difference in the thermal properties of biological tissue in the frozen and thawed state.

4.1. Conductive Heat Transfer

Warming by conductive heat transfer has already been eliminated because of the empirical observations (Pegg *et al.* 1978, Burdette 1981) of the large temperature gradients produced by even moderate warming rates, say greater than 3K/min. However, since conductive heat transfer occurs in all warming schemes, it is instructive to examine why these large temperature gradients appear.

Simple conductive heat transfer is described by a diffusion equation, and characterized by a parameter known as the thermal diffusivity. Unfortunately, the thermal diffusivity of frozen tissue is about six times greater than that of thawed tissue. If warming is by conductive heat transfer, the outside of the organ thaws first, thus the inside becomes thermally insulated from the heat source so that it stays frozen whilst the outside is exposed to excessive temperatures, and the risk of burning.

4.2. High Pressure

High pressure can be used to change the temperature of the phase transition from ice to water (Karow 1981), but the pressures needed are very destructive in practice (Ketterer *et al.* 1979). Actual heat transfer is performed using some other technique e.g.

thermal conduction.

4.3. Acoustic Heat Transfer

Acoustic hyperthermia techniques are currently being successfully applied to cancer therapy (Fessenden et al. 1984), and it may become possible to adapt this technology for rapid warming. The major advantage of acoustic heat transfer is that the energy absorbed by biological tissue generally decreases as the temperature increases (Bamber and Hill 1979). This would prevent 'thermal runaway', which is a serious problem in electromagnetic warming (see chapter 2). However, at the power levels required to achieve rapid warming, it is quite possible that acoustic energy will cause the rupture of cell membranes; indeed sonicators used for disrupting cells work on this principle (Ketterer et al. 1979)

4.4. Electromagnetic Warming

Experimental electromagnetic (EM) rewarming of cryopreserved organs has been attempted by several workers. In most such experiments, the organ to be rewarmed is exposed to the EM field generated by an 'applicator', such as a cavity or antenna. Various molecular processes dissipate the energy extracted from the electric field, thereby heating the organ. The dielectric properties of the organ plus cryoprotectant determine the amount of energy extracted from the field. These properties are dependent on the frequency of the EM field, the temperature of the organ, and to some extent, the composition of the cryoprotectant.

Another EM warming technique, also used for cancer hyperthermia therapy (Stauffer et al. 1984), uses small ferromagnetic spheres or 'electroseeds' which are implanted in the tissue to be heated. An external EM field heats the lossy spheres, which heat the surrounding tissue by thermal conduction.

5. Experimental EM Warming of Cryopreserved Organs

The earliest attempt to use EM energy to warm organs rapidly was made in 1957 by Smith (1961). Hamster hearts were perfused with 2M glycerol as a cryoprotectant, cooling was by surface conduction at about 1K/min. Warming was performed using either microwave irradiation (frequency unspecified) or thermal conduction, with warming rates of 100K/min or 10K/min respectively. Neither slow nor rapid warming produced viable organs but there was some electrical activity remaining in those that had been thawed quickly.

Since this pioneering effort, electromagnetic rewarming techniques have been employed by several workers, with little success on large (human size) organs - reviews by Voss et al. (1974), and Burdette and Karow (1978a) provide further examples.

5.1. Successful Cryopreservation ?

The most notable exception to the generally gloomy findings above, is the work of Guttman et al. (1977) on a dog kidney model system. In their study, kidneys were perfused with a DMSO based cryoprotectant, and cooled to -80°C using conduction and intra-arterial helium perfusion at 1-3K/min. Warming was performed with a domestic microwave oven, operating at 2450MHz, giving average warming rates of 50K/min. They were able to recover sufficient renal function in the rewarmed organs to allow reimplantation, and subsequent survival of 8 of the donor animals (who had their other kidney removed one month after reimplantation), achieving an overall success rate of 50%.

Unfortunately attempts to repeat these experiments both by Pegg et al. (1978) and later by Guttman and co-workers (1979, 1980) have been totally unsuccessful. No fully satisfactory explanation of the failure to repeat the original experiments has arisen, although there were considerable uncertainties in the power levels supplied to the organs by the (different) microwave ovens used in all three of the attempts. Microwave ovens are essentially overmoded resonant cavities - the electromagnetic

field, and hence the power deposition, are very hard to predict and very hard to measure inside a rapidly warming organ.

5.2. The Work of Burdette et al.

After much detailed study of the engineering problems involved in electromagnetic rapid warming (Burdette and Karow 1978a), Burdette and his collaborators performed two series of cryopreservation experiments on rabbit, and on dog kidneys (Burdette et al. 1978b, 1980b). One of the most significant features of their work is that they made dielectric measurements of perfused kidney tissue in order to design the electromagnetic warming system. Their dielectric measurement techniques and results are discussed in later chapters; the results of their cryopreservation experiments are described here.

In the first series of experiments (Burdette et al. 1978b), kidneys from rabbits and dogs were perfused with solutions containing various DMSO concentrations, and frozen to -70°C at cooling rates of 0.8-2K/min by conduction. The organs were warmed using a dielectric-loaded waveguide horn operating at 2450MHz, allowing warming rates of about 40K/min to be attained. Now the deposition of microwave energy at 2450MHz is predominantly in the first centimetre or so of thawed tissue - this phenomenon is described in greater detail in chapter 2. To alleviate the non-uniform heating this effect produces in canine kidney, small steel spheres (electroseeds) were implanted in the organ prior to freezing. At the same time as the 2450MHz radiation was applied, the organ was exposed to an RF induction coil operating at 7MHz that heated the electroseeds, and thus the interior of the organ.

No reimplantation of the rewarmed organs was attempted in this series; the post-thaw evaluation was based on observations of the microscopic and macroscopic anatomy. Burdette et al. concluded that use of DMSO improves post-thaw morphology, and that although warming was sufficiently uniform at 2450MHz in rabbit kidneys, electroseeds were essential to transfer energy to the interior of the dog kidneys. They also identified some of the unique temperature measurement problems encountered in the rapid

warming of organs using electromagnetic fields.

In the second series of experiments (Burdette et al. 1980b), canine kidneys were perfused with 0.7M DMSO, and frozen by conduction to -80°C at 0.5-1K/min. Warming was performed using a dielectric-loaded waveguide horn, this time operating at 918MHz, allowing warming rates of 20-60K/min to be achieved. Of the 27 kidneys that were rewarmed, 25 were thawed rapidly and uniformly - post-thaw surface temperature differences were less than 6°C. Burdette et al. showed that warming uniformity was much improved over that produced by the 2450MHz excitation used in the first series. Post-thaw evaluation of renal function was provided by re-implanting 11 of the kidneys in the donor animals, whose other kidney was removed at the same time. None of the kidneys sustained life for a significant period of time, though the authors seemed very optimistic about the degree of uniformity achieved.

In 1982, before starting our work, we contacted Burdette who informed us that because of funding difficulties, he had discontinued his work in this area.

6. Summary

There is a severe shortage of kidneys and other organs for transplantation, which could be alleviated if such organs could be stored at cryogenic temperatures. Such technology is already available for the preservation of cell suspensions e.g. blood components. However, organ cryopreservation has not yet been achieved.

Although there are other biophysical problems, evidence from a wide range of biological systems suggests that uniform, rapid warming is necessary, at rates of up to perhaps 300K/min. Heat transfer by thermal conduction cannot provide uniform warming because of the adverse behaviour of the thermal properties of tissue on thawing. Electromagnetic (EM) warming offers the possibility of depositing the energy throughout the organ,

although careful choice of operating frequency and cryoprotectant are required. The value of the dielectric permittivity of the cryopreserved tissue, and its temperature dependence, are required to design such an EM thawing system.

Experimental attempts to rewarm cryopreserved organs using EM energy have been largely unsuccessful, with the exception of a series of experiments performed by Guttman et al. in 1977, although attempts to repeat these experiments, both by Guttman and others have failed.

7. Bibliography

Ashwood-Smith M J and Farrant J (eds.)
"Low Temperature Preservation in Medicine and Biology",
1980, Tunbridge Wells: Pitman Medical Ltd.
UL 379:1.c.95.310; ISBN 0-272-79557-7

Karow A M and Pegg D E (eds.)
"Organ Preservation for Transplantation",
2nd Ed., 1981, New York: Marcel Dekker
UL 306:2.b.95.481; ISBN 0-8247-1083-5

Marberger M and Dreikorm K (eds.)
"Renal Preservation",
Vol. 8 of International Perspectives in Urology, series ed.
J A Libertino
1983, Baltimore: Williams & Wilkins
UL 306:2.b.95.498; ISBN 0-683-05585-2

Pegg D E and Jacobsen I A (eds.)
"Organ Preservation II",
1979, Edinburgh: Churchill Livingstone
UL 306:2.c.95.447; ISBN 0-443-01781-6

Pegg D E, Jacobsen I A and Halasz N A (eds.)
"Organ Preservation: Basic and Applied Aspects",
1982, Lancaster: MTP Press
UL 306:2.c.95.596, ISBN 0-85200-418-4

Chapter 2

Dielectric Properties and Electromagnetic Heating

One of the major problems in organ cryopreservation is that of producing rapid, uniform warming in cryopreserved organs. Different warming techniques have been tried, with sporadic success, but the most promising approach seems to be warming using electromagnetic fields.

The aim of this chapter is to explain the relevance of dielectric properties to the organ rewarming problem, and to show how these properties control the rate of energy deposition. First an outline of the microscopic origin of the macroscopic dielectric properties is given. Section 2 is a brief account of the origin of dielectric loss and the frequency dependence of the dielectric permittivity in both polar liquids and in tissue. The temperature dependence of the dielectric properties is discussed in section 3. Implicit in any rewarming scheme is an 'applicator' which is used to generate an EM field in the organ. So, section 4 examines two simple applicator geometries to show how the choice of applicator affects the power absorption. Section 5 describes one of the most crucial problems of EM heating - thermal runaway.

1. Dielectric Properties

The dielectric properties of materials characterize the interaction between electric fields and microscopic, atomic and molecular processes. Most standard texts on electromagnetic theory e.g. Lorrain and Corson (1970), or Ramo et al. (1965) explain the origin of dielectric properties in simple dielectrics. There are specialist books on the dielectric behaviour of solids (Jonscher et al. 1983), industrial materials (Metaxas and Meredith 1983), aqueous dielectrics (Hasted 1973) and biological molecules

UNIVERSITY LIBRARY CAMBRIDGE

in solution (Grant et al. 1978).

1.1. Maxwell's Equations

The basis of electromagnetic field theory are Maxwell's equations. When taken together with the constitutive relations of the material, and the boundary conditions at any material interface these equations describe the fields in that material. The macroscopic versions of Maxwell's equations in point form are

$$\text{div}\underline{D} = \rho_f \qquad (2.01a) \qquad \text{curl}\underline{E} = -\frac{\partial \underline{B}}{\partial t} \qquad (2.01b)$$

$$\text{div}\underline{B} = 0 \qquad (2.01c) \qquad \text{curl}\underline{H} = \underline{J}_f + \frac{\partial \underline{D}}{\partial t} \qquad (2.01d)$$

where $\underline{E}$ and $\underline{H}$ are the electric and magnetic fields, $\underline{D}$ and $\underline{B}$ are the electric and magnetic flux densities, $\underline{J}_f$ is the current density and ρ_f is the free charge density. The constitutive relations can be written

$$\underline{D} = \varepsilon_o \underline{E} + \underline{P} \qquad (2.02a) \qquad \underline{B} = \mu_o(\underline{H} + \underline{M}) \qquad (2.02b)$$

$$\underline{J}_f = \sigma_{dc}\underline{E} \qquad (2.02c)$$

where ε_o and μ_o are the permittivity and permeability of free space (constants), and σ_{dc} is the dc conductivity of the material. The quantities $\underline{P}$ and $\underline{M}$ are the electric and magnetic polarization vectors. From a macroscopic point of view, biological tissue is non-magnetic, so $\underline{M} = 0$. Because of free charge movement by ionic conduction, all tissues possess a significant amount of dc conductivity, so σ_{dc} is non-zero. The electric polarization, $\underline{P}$, is the subject of the next section.

1.2. Polarization and Dielectric Properties

The term 'polarization' refers to the perturbation of microscopic charge distributions that occurs when an electric field is applied to any dielectric material. Polarization is quantified in terms of the dipole moment $\underline{p}$ for a particular

structure, which is a function of the charges q_i and their vector separation $\underline{x}_i$ i.e.

$$\underline{p} = \sum_i q_i \underline{x}_i \qquad (2.03)$$

The amount of perturbation, and hence $\underline{p}$, is proportional to the local electric field seen by the charges in the structure, which in turn is a function of the external electric field and the surrounding medium.

There are several polarization mechanisms. Electronic polarization is produced by the electrons that surround all atomic nuclei, and molecular polarization is produced by changes in the charge distribution in bonds between atoms. Orientational polarization occurs in polar dielectrics, in which the molecules possess permanent dipole moments. Normally the dipole moments of the molecules are randomly aligned by thermal agitation; it is only once a field is applied that they begin to align, and the bulk polarization appears. Maxwell-Wagner or 'interfacial' polarization is observed in heterogeneous systems, where charge accumulation occurs at material interfaces. Orientational and Maxwell-Wagner polarization are both particularly important in biological materials.

The macroscopic polarization vector $\underline{P}$ is the net dipole moment per unit volume and is related to the macroscopic electric field $\underline{E}$ by

$$\underline{P} = \varepsilon_o \chi_e \underline{E} \qquad (2.04)$$

where χ_e is the electric susceptibility. The relative permittivity is defined so that $\varepsilon_r = 1 + \chi_e$; substituting (2.04) into constitutive relation (2.02a) gives

$$\underline{D} = \varepsilon_o \varepsilon_r \underline{E} \qquad (2.05)$$

The susceptibility χ_e, and by implication ε_r, are in general, tensor quantities which may also depend on $\underline{E}$. Although many biological materials are anisotropic in terms of their microscopic structure and physical properties, e.g. bone or tendon, for soft

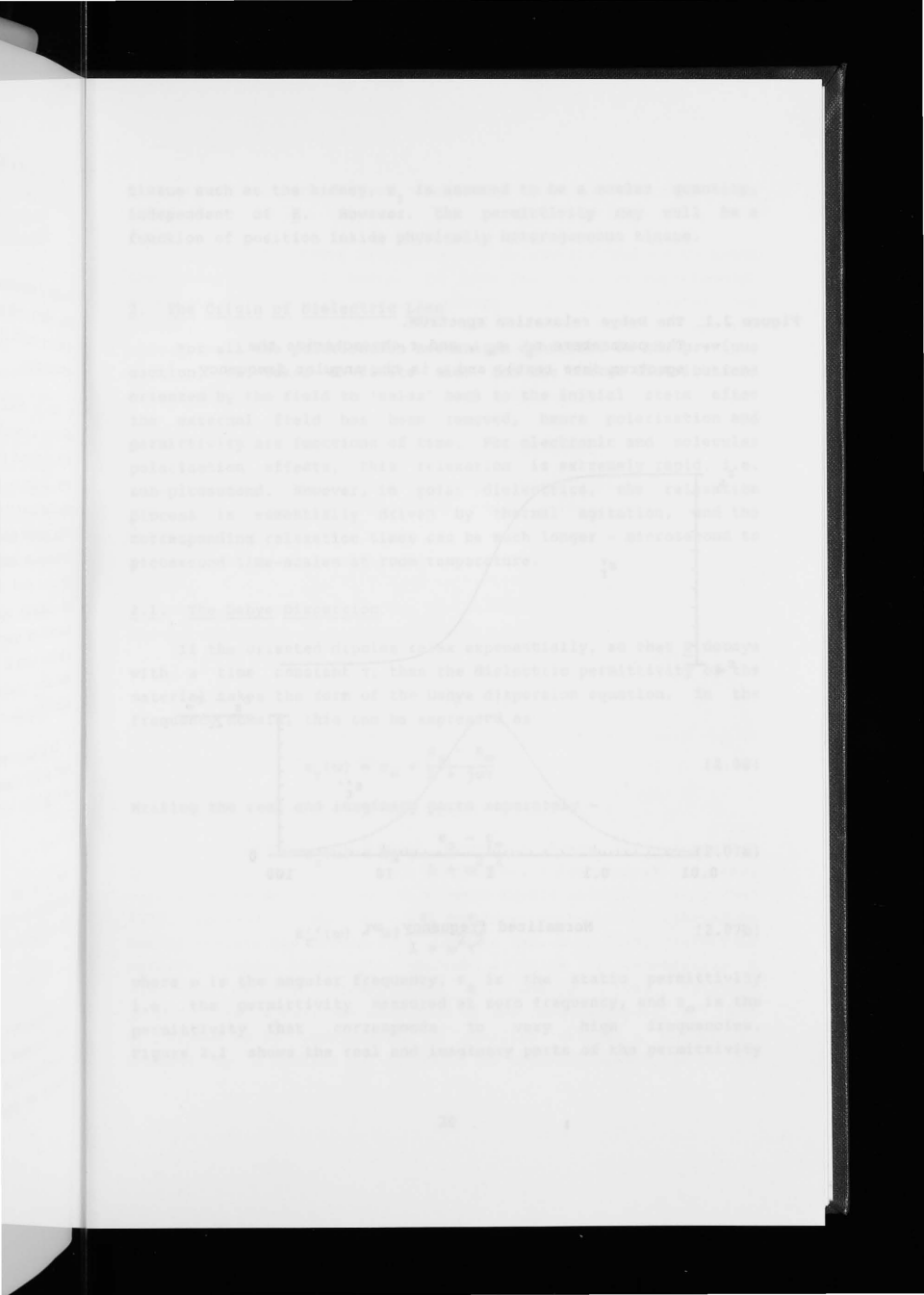

Figure 2.1 The Debye relaxation spectrum.
The parameters ε_s, ε_∞, and τ characterize the spectrum (see text), and ω is the angular frequency.

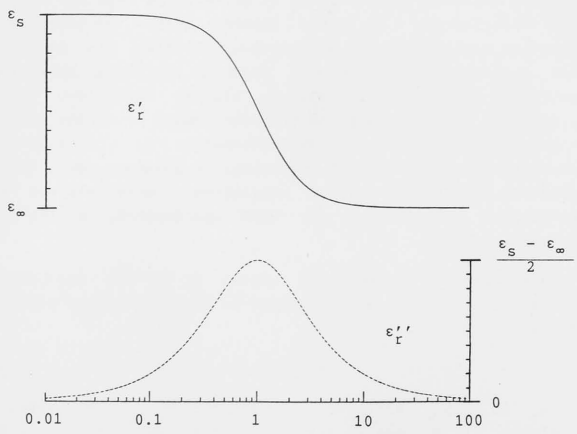

tissue such as the kidney, ε_r is assumed to be a scalar quantity, independent of $\underline{E}$. However, the permittivity may well be a function of position inside physically heterogeneous tissue.

2. The Origin of Dielectric Loss

For all the polarization mechanisms described in the previous section, it takes a finite time for the charge distributions oriented by the field to 'relax' back to the initial state after the external field has been removed, hence polarization and permittivity are functions of time. For electronic and molecular polarization effects, this relaxation is extremely rapid, i.e. sub-picosecond. However, in polar dielectrics, the relaxation process is essentially driven by thermal agitation, and the corresponding relaxation times can be much longer - microsecond to picosecond time-scales at room temperature.

2.1. The Debye Dispersion

If the oriented dipoles relax exponentially, so that $\underline{P}$ decays with a time constant τ, then the dielectric permittivity of the material takes the form of the Debye dispersion equation. In the frequency domain, this can be expressed as

$$\varepsilon_r(\omega) = \varepsilon_\infty + \frac{\varepsilon_s - \varepsilon_\infty}{1 + j\omega\tau} \tag{2.06}$$

Writing the real and imaginary parts separately -

$$\varepsilon_r'(\omega) = \varepsilon_\infty + \frac{\varepsilon_s - \varepsilon_\infty}{1 + \omega^2\tau^2} \tag{2.07a}$$

$$\varepsilon_r''(\omega) = \omega\tau \frac{\varepsilon_s - \varepsilon_\infty}{1 + \omega^2\tau^2} \tag{2.07b}$$

where ω is the angular frequency, ε_s is the static permittivity i.e. the permittivity measured at zero frequency, and ε_∞ is the permittivity that corresponds to very high frequencies. Figure 2.1 shows the real and imaginary parts of the permittivity

plotted against normalized frequency for such a dispersion function.

Although the Debye dispersion was originally derived to model the permittivity of gases, it also describes the experimental behaviour of many polar liquids, though it is less successful for solids. In many cases, there are several molecular species undergoing orientational polarization in the electric field, each with a separate relaxation time, so that a summation of Debye dispersion terms of the form of (2.06) are required.

2.2. The Cole-Cole and Cole-Davidson Dispersions

Some associated liquids are better represented by the one of the two dispersion functions given below. The Cole-Cole dispersion function is

$$\varepsilon_r(\omega) = \varepsilon_\infty + \frac{\varepsilon_s - \varepsilon_\infty}{1 + (j\omega\tau)^{1-\alpha_{cc}}} \qquad (2.08)$$

The Cole-Davidson dispersion function is

$$\varepsilon_r(\omega) = \varepsilon_\infty + \frac{\varepsilon_s - \varepsilon_\infty}{(1 + j\omega\tau)^{\beta_{cd}}} \qquad (2.09)$$

where α_{cc} and β_{cd} (usually $<< 1$) can be interpreted as measures of the 'spread' of relaxation times around τ.

2.3. Complex Permittivity and Complex Conductivity

Time-dependent relaxation phenomena force the frequency domain permittivity to be both complex and a function of frequency - this can be derived from the Kramers-Kronig relations (Jonscher 1983; pp47-52). The real and imaginary parts can be related to energy storage and dissipation inside a region of lossy dielectric material using Poynting's theorem - which is essentially a statement of the conservation of energy. The relative permittivity, $\varepsilon_r(\omega)$, has real part ε_r' and imaginary part $-\varepsilon_r''$, and is assumed to be independent of position within a volume V, bounded by a surface S. Further, the material within the volume

is assumed to possess finite dc conductivity σ_{dc}, and no magnetic polarization. Under these assumptions, Poyntings theorem becomes

$$-\frac{1}{2}\int_S \underline{E} \times \underline{H}^*.\underline{dS} = \frac{1}{2}\int_V (\sigma_{dc} + \omega\varepsilon_r''\varepsilon_o)|\underline{E}|^2 dV$$

$$+ j\omega\frac{1}{2}\int_V (\mu_o|\underline{H}|^2 - \varepsilon_r'\varepsilon_o|\underline{E}|^2)dV \qquad (2.10)$$

The left hand side of this equation is the total complex power flowing across S into V. The first term on the right hand side is the real power dissipated in the medium by $\underline{E}$, the second term represents the reactive power i.e. energy stored in the material. Clearly, the real part of the permittivity ε_r', controls the energy stored in the electric field, and the imaginary part ε_r'' together with the conductivity σ_{dc}, controls energy dissipation (heating) in the material.

Now (2.10) is written in terms of 'known' fields $\underline{E}$ and $\underline{H}$, however, the fields are generated by the sources of charge and current external to the volume V. As a consequence, $\underline{E}$ and $\underline{H}$ are also controlled by the electrical properties of the material, and the geometry of the 'applicator' - the device used to generate the field in the material. Section 4 investigates two simple applicator geometries to get some idea of the effect of the applicator on the power dissipation in a practical warming system.

Equation (2.01d) is the only one of Maxwell's equations that involves $\underline{J}_f$, and for linear isotropic dielectrics, it can be written as

$$\text{curl}\underline{H} = (\sigma_{dc} + j\omega\varepsilon_r\varepsilon_o)\underline{E} \qquad (2.11)$$

It is common to define a complex permittivity[‡], $\varepsilon_r^{\ddagger}$ in which the imaginary part of the permittivity incorporates the conductivity implicitly i.e.

---

‡ Many textbooks on dielectrics use the '*' superscript to denote a complex variable. In this dissertation, '‡' is used for this purpose, to avoid conflict with '*' which is used to denote complex conjugate.

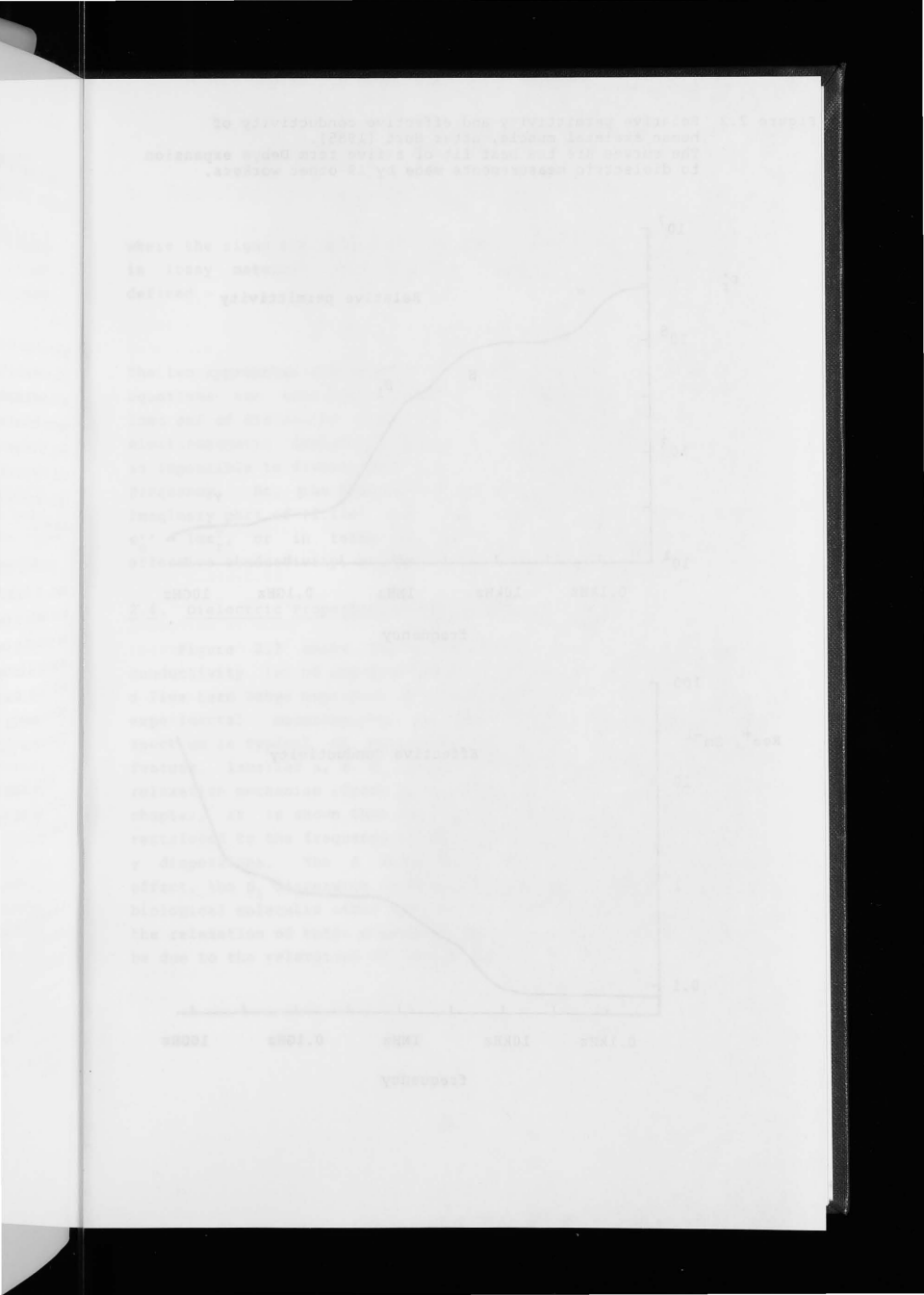

Figure 2.2 Relative permittivity and effective conductivity of human skeletal muscle, after Hurt (1985). The curves are the best fit of a five term Debye expansion to dielectric measurements made by 19 other workers.

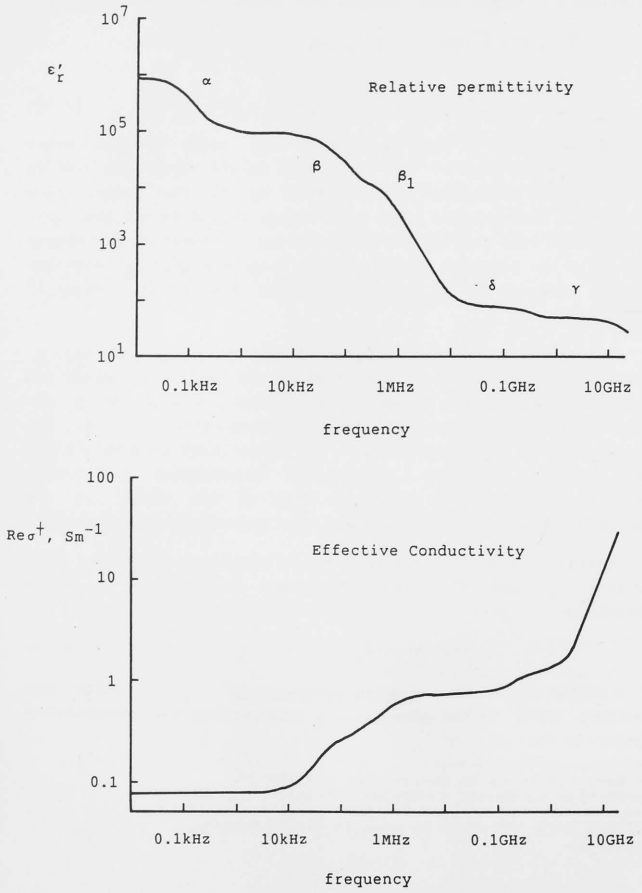

$$\varepsilon_r^+ = \varepsilon_r' - j(\varepsilon_r'' + \frac{\sigma_{dc}}{\omega\varepsilon_o}) \qquad (2.12a)$$

where the signs are chosen so that the imaginary part is negative in lossy materials. Alternatively, a complex conductivity can be defined -

$$\sigma^+ = (\sigma_{dc} + \omega\varepsilon_o\varepsilon_r'') + j\omega\varepsilon_o\varepsilon_r' \qquad (2.12b)$$

The two approaches are formally equivalent as far as Maxwell's equations are concerned, although the mechanisms of conductive loss and of dielectric loss are fundamentally different. For electromagnetic heating of tissue and dielectric measurements, it is impossible to divorce the two loss mechanisms at a single frequency. So, the loss can be described either in terms of the imaginary part of (2.12a) i.e. the effective dielectric loss, $\varepsilon_e'' = \mathrm{Im}\varepsilon_r^+$, or in terms of the real part of (2.12b) i.e. the effective conductivity, $\sigma = \mathrm{Re}\sigma^+$, whichever is more appropriate.

2.4. Dielectric Properties of Biological Materials

Figure 2.2 shows the permittivity (ε_r') and effective conductivity (σ) of muscle fibres. These curves are derived from a five term Debye expansion which was fitted to a large body of experimental measurements by Hurt (1985). This dispersion spectrum is typical of biological materials. Each dispersion feature, labelled α, β, β_1, δ and γ can be assigned to a specific relaxation mechanism (Grant et al. 1978; pp4-6). Later in this chapter, it is shown that the choice of frequency for thawing is restricted to the frequency range which includes the β, β_1, δ and γ dispersions. The β dispersion is due to the Maxwell-Wagner effect, the β_1 dispersion is due to orientational polarization of biological molecules other than water. The γ dispersion is due to the relaxation of water molecules; the δ dispersion is thought to be due to the relaxation of 'bound' water.

3. Temperature Dependence of Dielectric Properties

The temperature dependence of the dielectric properties is of particular importance in this application. Electronic and molecular polarization are relatively independent of temperature; this is not the case for orientational polarization which is an important polarization mechanism in water and other biological materials. For organ thawing, we must also consider the change in dielectric properties produced by the ice to water phase transition.

3.1. Dielectric Properties of Water, Ice and Saline

3.1.1. Dielectric Properties of Liquid Water

The dielectric dispersion of liquid water at 25°C can be represented as a Cole-Cole dispersion with distribution parameter $\alpha_{cc} = 0.014 \pm 0.007$, $\varepsilon_\infty = 4.6 \pm 1.1$, $\varepsilon_s = 78.30 \pm 0.05$, and $\tau = 8.08 \pm 0.2$ps (Grant et al. 1978; pp145-146, Schwan et al. 1976). According to Grant et al., the value of α_{cc} takes a larger value (between 0.025 and 0.045) near 4°C. The high frequency permittivity, ε_∞, varies from 4.0 to 4.5 between 0°C and 60°C. Theoretical considerations suggest that the static permittivity of water should possess a temperature dependence of the form

$$\varepsilon_s = \varepsilon_\infty + \frac{A}{T} \tag{2.13}$$

where A is a constant, and T is the absolute temperature (Grant et al. 1978; p149, Von Hippel 1967). Malmberg and Maryott (1956) made accurate bridge measurements of ε_s for water over 0°C to 100°C. They give an expression, reproduced below, that fits this predicted temperature variation quite well:

$$\varepsilon_s = 87.74 - 0.40008\theta + 0.9398\times10^{-3}\theta^2 - 1.410\times10^{-6}\theta^3 \tag{2.14}$$

where θ is the temperature in °C. In many systems the temperature dependence of the relaxation time τ is of the form

$$\ln(\tau T) = \frac{B}{T} + C \tag{2.15}$$

Figure 2.3 The dielectric permittivity of water around the solid-liquid phase transition: (a) at -0.1°C (Ice I) and (b) at +0.1°C (Liquid Water). The curves were generated using Debye parameters given by Von Hippel (1968) for (a) and Stogryn (1971) for (b).

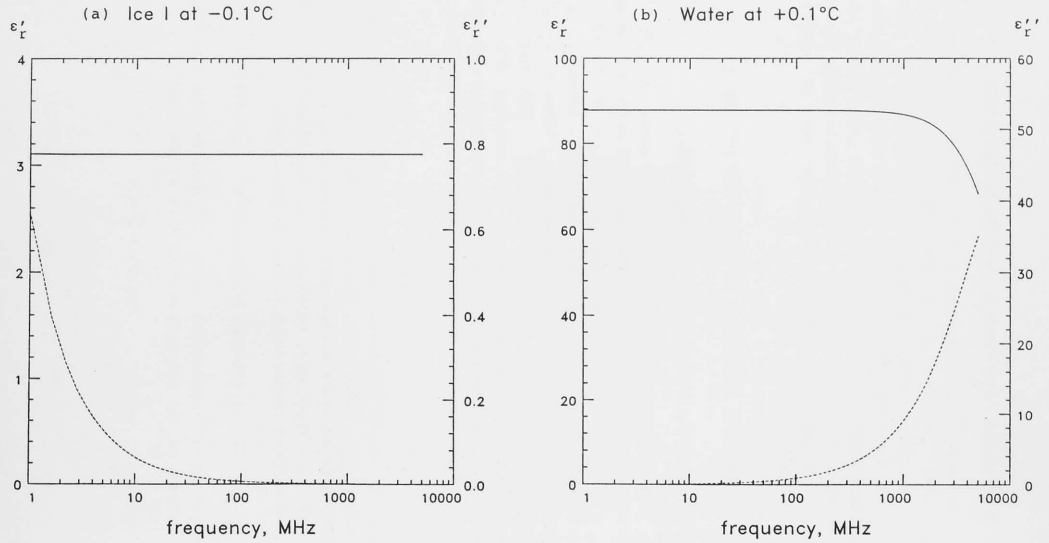

where B and C are constants (Grant et al. 1979). However, in water, the relaxation time decreases with increasing temperature approximately exponentially i.e.

$$\tau = \tau_o \exp(\frac{T_o}{T}) \qquad (2.16)$$

where τ_o = 1.9fs, and T_o = 2500K. These two parameters were obtained by performing a least-square fit of the data from Hasted (1973; p47) over 0 to 30°C; this data is given in Table 2.1 below. T_o is often interpreted in terms of an activation enthalpy for the relaxation process = $\Delta H/R$; here $\Delta H \simeq 21$kJ/mol.

3.1.2. Dielectric Properties of Ice

The dielectric properties of ice I (which is the phase present at atmospheric pressure) can be represented by a Debye dispersion. Table 2.1 gives the Debye dispersion parameters for water and ice I over a range of temperatures around the phase transition.

The static permittivity and high frequency permittivity of water and ice are quite similar, though there is a sharp contrast in the values of the relaxation times, and the activation enthalpy for ice I is about 2.6 times larger than that for water. Figure 2.3 shows the real and imaginary parts of the permittivity of these two states of water plotted over the same frequency range - 1MHz to 10GHz.

3.1.3. Dielectric Properties of 150mM Saline

So far, the effects of ionic conductivity have been ignored; a solution that better approximates biological materials for these purposes is 150mM saline. Stogryn has published a set of formulae that give the complex permittivity of saline as a function of frequency, salt concentration and temperature (Stogryn 1971). These formulae are collected with the dispersion parameters of other materials used in this work in appendix 2. Figure 2.4 shows the temperature and frequency dependence of the real part of the dielectric permittivity, and the effective conductivity of 150mM

Figure 2.4 Relative permittivity, and effective conductivity of 150mM saline calculated from the Stogryn formula (Stogryn 1971). Each parameter has been plotted at four different temperatures over a frequency range of 10MHz to 3GHz.

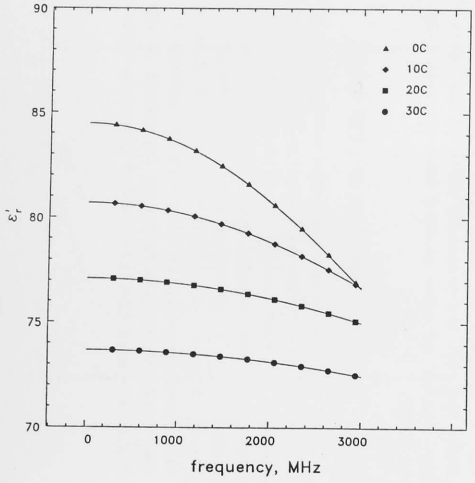

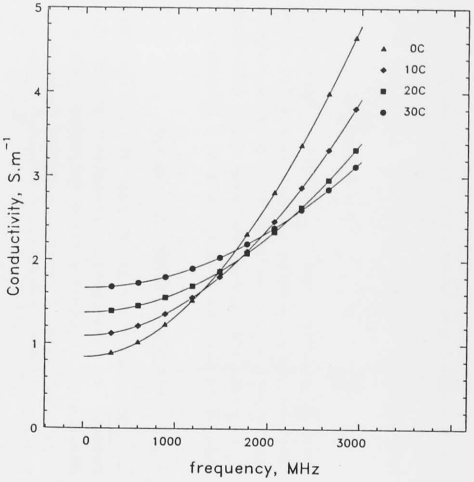

Table 2.1

Dielectric Properties of Ice I and Water

Material	Temperature °C	ε_s	ε_∞	τ ps
Ice I[a]	-32.0	100	3.00	570×10^6
	-20.9	97.4	3.10	164×10^6
	-10.8	95.0	3.08	60×10^6
	-0.1	91.5	3.10	22×10^6
Water[b]	0.1	87.7	4.9	17.6 (17.9)
	10.0	83.8	4.9	12.6 (12.6)
	20.0	80.1	4.9	9.28 (9.3)
	30.0	76.5	4.9	7.17 (7.2)

Notes: 1. Values in parentheses are from Hasted (1973), p47.
2. Activation enthalpies, obtained from least-square fit of the above τ data to equation (2.16), Ice I: $\Delta H \simeq 55$kJ/mol, Water: $\Delta H \simeq 21$kJ/mol.

Sources: a) Von Hippel (1968), b) Stogryn (1971)

saline. The low frequency conductivity appears to increase approximately linearly with temperature. In fact, the Stogryn formula for the dc conductivity of 150mM saline gives

$$\sigma_{dc} = 0.8388 + 2.384\times10^{-2}\theta + 1.152\times10^{-4}\theta^2 \qquad (2.17)$$

where θ is the temperature in °C.

3.2. Temperature Dependence of the Effective Conductivity

The temperature coefficient of the effective conductivity of 150mM saline is positive below 1600MHz, and negative above this frequency. This behaviour can be explained qualitatively for a general Debye dispersion, using equations (2.13), (2.16) to describe the temperature dependence of ε_s and τ respectively.

The effective conductivity can be decomposed into the dc component and the component due to dipolar loss. Differentiating with respect to temperature yields

$$\frac{\partial \sigma}{\partial T} = \frac{\partial \sigma_{dc}}{\partial T} + \omega \varepsilon_o \frac{\partial \varepsilon_r''}{\partial T} \qquad (2.18)$$

The first term on the right hand side, the rate of change of the dc conductivity with temperature is positive, e.g. for 150mM saline (2.17) gives a value of about +0.025. The second term is expanded by differentiating (2.07b) producing

$$\omega \varepsilon_o \frac{\partial \varepsilon_r''}{\partial T} = \frac{(T_o - T)\omega \varepsilon_o}{T^2(1 + \omega^2 \tau^2)} \left(\omega^2 \tau^2 - \frac{T_o + T}{T_o - T} \right) \varepsilon_r'' \qquad (2.19)$$

So the value of the second term in (2.18) is frequency dependent, and more interestingly, **negative** at frequencies below $\omega\tau = 1$ (assuming $T << T_o$).

In fact this temperature dependence can be inferred more or less directly from the temperature dependence of τ - as T increases, τ gets smaller, thus the frequency at which the peak in the loss factor occurs, $f_p = 1/2\pi\tau$ occurs moves up too. At frequencies below f_p, as the temperature increases, the effective dielectric loss decreases, conversely, above f_p, the effective loss increases. For water, f_p = 19.7GHz at 25°C (Schwan et al. 1976); so the temperature coefficient of the water dispersion will certainly be negative for the range of frequencies plotted in Figure 2.4. However the net temperature coefficient includes the positive temperature coefficient of the dc conductivity which dominates at low frequencies. Below about 200MHz in 150mM saline, the negative temperature coefficient of the dipolar loss is almost completely hidden. For ice I, f_p = 0.97kHz at -20.9°C, so even the temperature coefficient of the dipolar loss will be positive.

4. Two Simple Applicator Geometries

Although the dielectric loss controls the power absorption in dielectric materials for given fields E and H, the applicator

Figure 2.5 Capacitive applicator, equivalent circuit admittance, and two possible driving configurations.

(a) Capacitive applicator containing material of complex permittivity $\varepsilon_r^\dagger$.

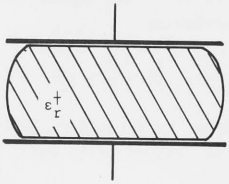

(b) Equivalent circuit admittance, Y_L

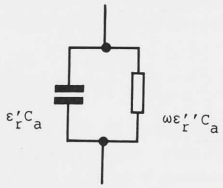

(c) Applicator driven by an ideal voltage source.

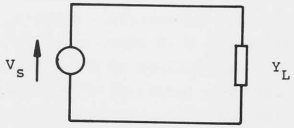

(d) Applicator driven by a current source with source admittance Y_s.

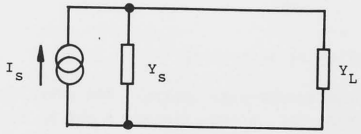

(used to 'apply' the external field) must also be considered. The problem is that, in general, the fields produced in the tissue are controlled by the electrical properties. Unfortunately, there is no general result; so any specific applicator geometry must be investigated individually using Maxwell's equations. This section considers two simple applicator geometries to get some idea of the interaction between the dielectric properties and the absorbed power.

4.1. Capacitive Applicator

Suppose that a block of dielectric material, which has uniform electrical properties, is placed between two metal plates which are connected to a single-frequency power source. If the frequency of the applied field is such that the wavelength in the material is much greater than the dimensions of the block, this system can be described by a single equivalent circuit capacitance, as shown in Figure 2.5. The admittance of the loaded applicator is

$$Y_L = j\omega C_a \varepsilon_r^{\dagger} \qquad (2.20)$$

where ω is the angular frequency, C_a is the geometrical capacitance of the applicator, and $\varepsilon_r^{\dagger}$ is the complex permittivity of the block.

4.1.1. Ideal Voltage Source

If the applicator is driven by an ideal voltage source strength V_s, then the power dissipated in the material at temperature T is

$$P(T) = \frac{1}{2} V_s^2 \omega C_a \varepsilon_t'' \qquad (2.21)$$

where $\varepsilon_t^{\dagger} = \varepsilon_t' - j\varepsilon_t''$ is the complex permittivity of the material at temperature T. In this case, the power is proportional to the effective conductivity, $\sigma_t = \omega \varepsilon_o \varepsilon_t''$, giving a very simple link between the dielectric properties and the absorbed power. It is convenient to normalize the power absorption to the power absorbed at some other temperature T_x where the absorption is a maximum.

This normalized power is defined as η

$$\eta(T) = \frac{P(T)}{P(T_x)} \tag{2.22}$$

so that here

$$\eta(T) = \frac{\varepsilon_t''}{\varepsilon_x''} = \frac{\sigma_t}{\sigma_x} \tag{2.23}$$

where $\varepsilon_x^{\dagger}$ is the complex permittivity at temperature T_x.

4.1.2. Current Generator with Finite Source Admittance

Figure 2.5c shows a power supply consisting of an ideal current source strength I_s, and a source admittance Y_s. This is a more realistic model of a practical power source. In principle, using suitable matching networks, Y_s can be chosen arbitrarily - maximum power is transferred to the load admittance Y_L (the applicator) when $Y_s = Y_L^*$.

Suppose maximum power transfer occurs at temperature T_x so that the source admittance is $Y_s = Y_x^*$. The power dissipated in the material at temperature T will be

$$P(T) = \frac{1}{2} I_s^2 \frac{\mathrm{Re}Y_t}{|Y_x^* + Y_t|^2} = \frac{1}{2} \frac{I_s^2}{\omega C_a} \frac{\varepsilon_t''}{(\varepsilon_x'' + \varepsilon_t'')^2 + (\varepsilon_x' - \varepsilon_t')^2} \tag{2.24}$$

and from (2.22), η is

$$\eta(T) = \frac{P(T)}{P(T_x)} = \frac{4\varepsilon_x''\varepsilon_t''}{(\varepsilon_x'' + \varepsilon_t'')^2 + (\varepsilon_x' - \varepsilon_t')^2} \tag{2.25}$$

This time η is a function of the real and imaginary parts of both complex permittivities. Note that if the power source had been modelled as a voltage source with finite source impedance, the form of (2.24) changes but (2.25) is invariant.

Figure 2.6 (a) Plane wave applicator. We consider a normally incident plane electromagnetic wave impinging on a semi-infinite slab of lossy material.

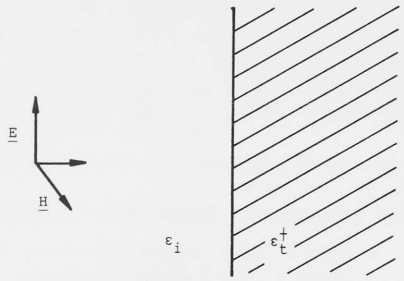

(b) Power penetration depth in 150mM saline for an incident plane wave. Complex permittivity of saline calculated using the Stogryn formula (Stogryn 1971).

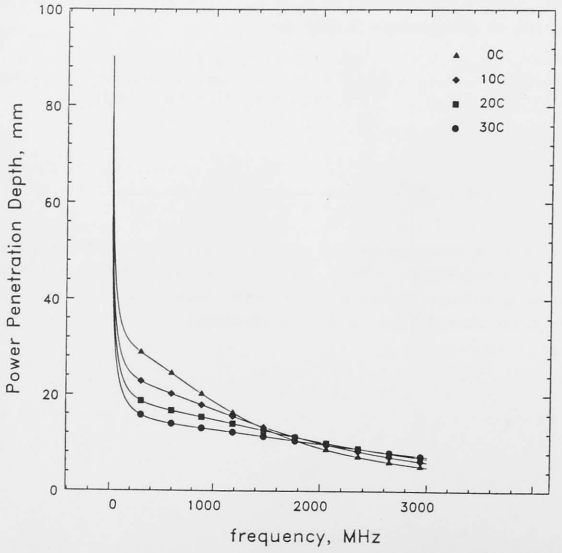

4.1.3. Practical Points

In a practical realization of this scheme, reported briefly by Ketterer et al. (1979), low frequency alternating current was passed through electrodes placed in contact with the surface of a kidney. However, Ketterer et al. identified an implicit stability problem with this form of applicator.

Suppose one part of the organ has thawed, and is consequently less resistive to the flow of current. If the two sections are in 'series', most of the power will be dissipated in the more resistive region (i.e. the frozen part) - which is exactly what is wanted. However, if the two regions are in 'parallel', most of the power will be dissipated in the thawed zone, a potentially unstable situation. Worse still, there is likely to be surface burning because of the electrode contact resistance, although this could be alleviated by using an intervening medium of similar conductivity.

A different approach has been suggested by Hessary and Chen (1984) for use in cancer hyperthermia therapy which might be usable here. In their scheme, the volume of tissue to be heated is surrounded by a large array of electrodes, and the power is 'steered' to where it is needed.

4.2. Plane Wave Applicator

If the frequency of the electromagnetic energy is such that the wavelength in the dielectric is comparable with or less than the dimensions of the applicator, then the applicator cannot be treated as a single circuit element.

As a simple case, consider a semi-infinite slab of dielectric material with an electromagnetic plane wave incident upon its surface, as shown in Figure 2.6a. The intervening medium is a lossless dielectric with dielectric constant ε_i e.g. air. Part of the incident wave will propagate into the material, and part will be reflected from the surface. In lossy materials, power is absorbed as the EM wave travels through the medium; the

attenuation increases exponentially with distance. The absorption can be usefully characterized by the 'penetration depth', D_p, which is the distance through which the wave travels before the power is reduced to 1/e (36.7%) of the value at the surface. For the geometry described above, D_p is solely a function of the material properties and is given by

$$D_p(T) = \frac{c}{\omega\sqrt{2}} \left[(\varepsilon_t'^2 + \varepsilon_t''^2)^{1/2} - \varepsilon_t'\right]^{-1/2}$$

$$= \frac{-c}{2\omega \mathrm{Im}\sqrt{\varepsilon_t^+}} \qquad (2.26)$$

where c is the velocity of light in free space. A related parameter is the total power that is absorbed in the semi-infinite slab, normalized to the incident power P_{inc}

$$\frac{P(T)}{P_{inc}} = \frac{4n_i \mathrm{Re}\sqrt{\varepsilon_t^+}}{|n_i + \sqrt{\varepsilon_t^+}|^2} \qquad (2.27)$$

where $n_i = \sqrt{\varepsilon_i}$. Figure 2.6b shows the computed power penetration depth in 150mM saline at four temperatures.

5. Thermal Runaway

Consider an organ warming system in which the electric and magnetic fields in the organ are spatially uniform; for example the capacitive applicator driven by an ideal voltage source. Now suppose that the organ has been warmed uniformly to temperature T, except for a small region that is at a higher temperature $T + \Delta T$. The discontinuity may be due to the spatial variation of the dielectric or thermal properties of the organ volume.

Now Poynting's theorem (2.10) shows that power absorption is dependent on the effective conductivity, σ. For the capacitive applicator, the power is proportional to σ. Qualitatively, we can see that if σ increases strongly with increasing temperature, the discontinuity will absorb more energy thus increasing the temperature further - which will quickly cause the discontinuity

to burn. This positive feedback is termed 'thermal runaway', and is one the most serious problems in both electromagnetic warming of organs, and in many industrial applications of microwave heating (Metaxas and Meredith 1983; pp54-58). Conversely, if the feedback can be made negative, i.e. power absorbed decreasing with increasing temperature, the discontinuity will tend to disappear.

Whatever the temperature dependence of σ, or more generally, the power absorption, thermal relaxation smooths out spatial discontinuities in the temperature distribution. Appendix 1 is an analytical investigation of thermal relaxation and thermal runaway which quantifies the effects of thermal relaxation. Also, an attempt is made to formulate a condition on the rate of change of power dissipation with temperature. Thermal relaxation can stabilize thermal runaway if the temperature coefficient of the absorbed power is small. However, the critical value of the temperature coefficient depends on the warming rate, the temperature increase of the bulk of the material, together with all the material properties, so it is difficult to make useful generalizations. Burdette et al. (1978b) were able to exploit thermal relaxation by pulsing their RF power source during rewarming.

There are other problems which are associated with the phase change from frozen to thawed, all of which enhance the possibility of thermal runaway:

a) The electrical conductivity, and the dielectric loss of tissue increase between frozen and thawed states.

b) The thermal diffusivity, which controls how quickly any non-uniform temperature distribution relaxes, reduces (by a factor of about 2.4 for beef).

c) The organ absorbs energy at constant temperature to make the phase transition - the latent heat of fusion (333.6kJ/kg for ice I -> water). This might allow cooler regions of the organ to 'catch up', though if the power deposition is predominantly at the surface, this may worsen the non-uniformity, as

described by Burdette and Karow (1978a).

5.1. Combating Thermal Runaway

Figure 2.4 shows that the effective conductivity of 150mM Saline does indeed decrease with increasing temperature at frequencies above about 1600MHz. This is exactly the sort of dielectric behaviour needed to avoid thermal runaway. Unfortunately, at these frequencies the distribution of energy in the saline becomes increasingly non-uniform and the power penetration depth becomes less than the smallest dimension of a kidney. Figure 2.6b shows the power penetration depth for 150mM saline over 0°C to 30°C; at 1600MHz, the penetration depth is about 12mm.

Clearly, a frozen organ perfused with cryoprotectant is a much more complex material than water, ice or saline. However, we can use these materials as a rough guide to the range of frequencies required for dielectric measurements on perfused tissue. Even if frequencies where the temperature coefficient is negative cannot be found, there are obviously frequencies to avoid. The low frequency limit is set by the positive temperature coefficient of the dc conductivity to about 10MHz. The high frequency limit is set by the power penetration depth to about 3GHz. The next chapter reviews the existing dielectric measurements that have been made on cryoprotectant solutions and perfused tissue.

6. Summary

The interaction between biological materials and electromagnetic fields is characterized by the complex permittivity ε_r^+. For a given electric field, $\mathrm{Im}\varepsilon_r^+$, which incorporates both conductive and dielectric loss mechanisms, controls the power absorbed by the material.

The situation is complicated by the fact that for external

sources of charge and current supplied by an applicator, the internal fields are also functions of ε_r^+. For the simplest case of an ideal voltage source driving a capacitive applicator, the dissipated power is directly proportional to the effective conductivity. Other geometries and driving arrangements produce more complex results. At high frequencies, electromagnetic field penetration into lossy media becomes spatially non-uniform, and the concept of 'penetration depth' becomes useful.

The dielectric properties of water are strongly temperature dependent; not least around the transition from ice to water. 150mM saline is more representative of the dielectric properties of tissue than water, and the dc conductivity of such saline shows a strong positive temperature coefficient.

Thermal runaway occurs when the temperature coefficient of the absorbed power is positive. Regions of a lossy material being heated by an EM field that are warmer absorb more power than the cooler regions; this positive feedback produces uncontrolled heating. Conversely, heating is stabilized if the temperature coefficient is negative. The dielectric loss in 150mM saline decreases with increasing temperature above about 1.6GHz. Dielectric measurements on perfused tissue are required so that frequencies suitable for rapid, controlled warming can be found.

Chapter 3

Review of Dielectric Measurements and Measurement Techniques for Cryoprotectants and Perfused Tissue

This chapter reviews dielectric measurements made on cryoprotectants and perfused tissue, and reviews methods for making such measurements over a range of frequencies and temperatures.

In organ cryopreservation, a cryoprotectant solution is perfused throughout the organ before cooling, so it is reasonable to expect that the dielectric properties of this solution will influence the electrical properties of the organ when it is rewarmed. Associated liquids, such as glycerol or propanediol are the basis of many cryoprotectants. Section 1 reviews existing dielectric measurements on pure associated liquids and on aqueous solutions of such liquids. Measurements of the electrical properties of tissue perfused with cryoprotectant are essential for the design of a rapid warming system using EM fields. A review of the dielectric measurements made by Burdette et al. in the late 1970's on perfused kidney tissue over a wide range of temperatures and frequencies is presented in section 2. Section 3 concludes that the existing measurement database is incomplete, and further measurements are required. Section 4 contains a brief review of suitable dielectric measurement techniques, and section 5 gives the reasons for the choice of the measurement systems used in this work.

1. Dielectric Properties of Cryoprotectants

Burdette (1981) has emphasized the importance of the cryoprotectant in modifying the effective dielectric properties of the perfused organ. Apart from water, the chief component of a cryopreservation solution is the cryoprotectant - often an 'associated liquid' such as glycerol or propanediol[‡]. Because of

the unusual structure of associated liquids, their RF and microwave spectra are of considerable interest to chemical physicists. Davidson and Cole (1951) investigated the dielectric dispersion of pure glycerol, propan-1-ol and propane-1,2-diol. They showed that although the dispersion of propan-1-ol could be adequately represented by a Debye formula, both glycerol and propane-1,2-diol require the empirically derived Cole-Davidson dispersion function. The form of this dispersion function, given in Chapter 2, can be interpreted in terms of an asymmetric distribution of relaxation times.

Litovitz and McDuffie (1962) measured the dielectric relaxation spectra of four associated liquids, including glycerol. McDuffie et al. (1962) investigated the dielectric relaxation spectra of glycerol-water mixtures over a range of frequencies at three sub-zero temperatures over a range of concentrations from pure glycerol to equimolar (cryoprotectants are rarely this concentrated). They showed that the relaxation time of the Cole-Davidson dispersion is reduced and the static permittivity increased by the presence of even small amounts of water. This suggests that the dielectric dispersion curves of cryoprotectants will consist of a single relaxation feature, as opposed to two distinct dispersions. However the dispersion parameter β_{cd} and the high frequency permittivity are relatively independent of the amount of water in the range of concentrations investigated.

Other investigators have performed dielectric measurements with rapid warming in mind. Macklis et al. (1975, 1979) have measured the dielectric properties of pure glycerol, solutions of ethanediol and pure dimethyl sulphoxide (DMSO). Their measurements covered a wide range of temperatures and concentrations, but only a very limited range of frequencies. Edwards (1982) made measurements on 3M glycerol at 100MHz over a range of low temperatures. The materials, temperatures, concentrations and frequencies investigated by all the workers

---

ǂ See Chapter 1. Appendix 2 includes the recipes for the cryoprotectants used in this work.

cited above are tabulated in Table 3.1.

Table 3.1

Dielectric Measurements of Cryoprotectants

Material	Temperature °C	Frequency	Conditions
Glycerol[a]	-75 to -40	20Hz-5MHz	Pure
Propanediol[a]	-90 to -45	20Hz-5MHz	Pure
Glycerol[b] in water	-7.5, -15.3 and -19.5	0.5-250MHz	Pure to equimolar
Glycerol[c]	-16 to +12	10kHz-1.2GHz	Pure
DMSO[d]	-60 to +20	1.48-1.54GHz	Pure
Glycerol[d]	-60 to +20	1.53-1.55GHz	Pure
Ethanediol[e]	-70 to +15	1.52-1.55GHz	0 to 10M in water
Glycerol[f]	-40 to 0	100MHz	3M in water

Sources: a) Davidson and Cole (1951)
b) McDuffie and Litovitz (1962)
c) McDuffie et al. (1962)
d) Macklis and Ketterer (1975)
e) Macklis et al. (1979)
f) Edwards (1982)

2. Dielectric Properties of Perfused Kidney Tissue

Burdette et al. (1978a, 1978b, 1980a, 1980b, 1981) have published measurements of the dielectric properties of several tissues, including canine kidney and rabbit kidney perfused with a DMSO based cryoprotectant over a -40°C to 0°C temperature range. Unfortunately, their published low temperature measurements are

Figure 3.1 The range of temperatures and frequencies covered in dielectric measurements of dog and rabbit kidney made by Burdette et al. (1978a, 1978b, 1980a, 1980b, 1981). Measurements made over the extended temperature range are on tissue that has been perfused with cryoprotectant. Also shown are the measurements of Brady et al. (1981) on bovine kidney, and those of Stuchly et al. (1982a) on cat kidney.

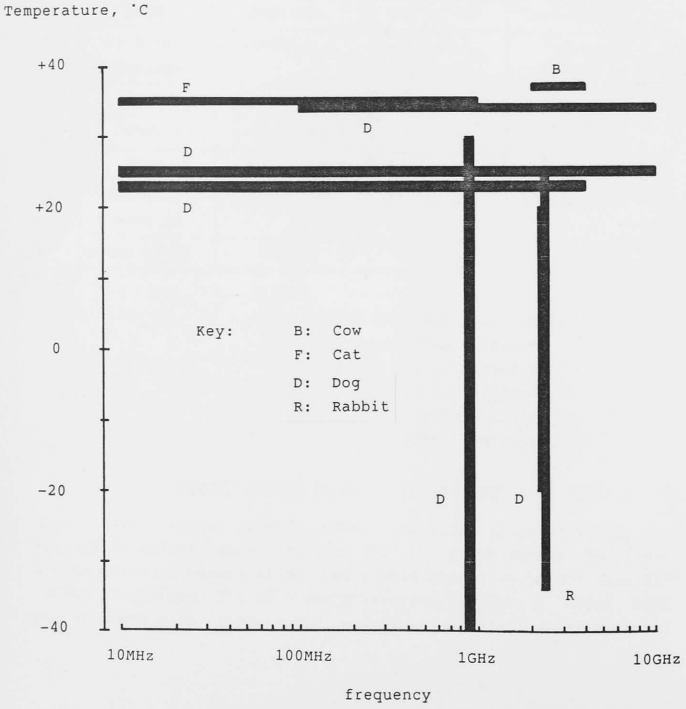

restricted to two frequencies - 918MHz and 2450MHz, which are the frequencies used in their cryopreservation experiments described in chapter 1. The temperature and frequency ranges of the measurements made by Burdette et al. are tabulated in Table 3.2, and shown graphically in Figure 3.1

Table 3.2

Dielectric Measurements of Perfused Kidney Tissue Published by Burdette et al.

Reference	Animal	Temperature °C	Frequency GHz	Conditions
1978a	Rabbit	-34 to +25	2.45	With DMSO ?
1978b	Rabbit	-20 & +25	2.45	0, 0.7M, 1.4M, and 2.1M DMSO
	Dog	+23	0.01-0.1 0.11-4	With DMSO ?
1980	Dog	+34	0.1-10	With 1.4M DMSO
	Dog	+34	0.1-10	no DMSO
	Dog	+34	0.1-4	in vivo
1981	Dog	+25	0.01-10	in vivo
	Dog	-40 to +30	0.918	With 0.7M DMSO
	Dog	-20 & +20	2.45	0, 0.7M, 1.4M, and 2.1M DMSO

Notes: The '?' indicates that it is not clear from the relevant paper if the tissue had been perfused with DMSO prior to the measurement.

As an example of their published measurements, Figure 3.2 shows the permittivity and effective dielectric loss of canine kidney tissue perfused with 0.7M DMSO prior to measurement, at 918MHz over a range of low temperatures (Burdette 1981). Other investigators have made dielectric measurements on excised bovine

Figure 3.2 Complex permittivity of canine kidney tissue perfused with 0.7M DMSO at 918MHz. After Burdette (1981).

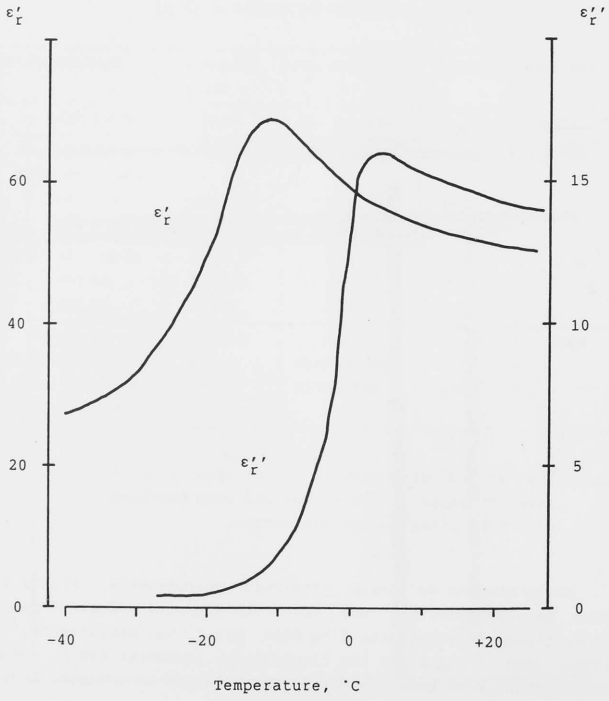

kidney (Brady et al. 1981) and both in vivo and in vitro cat kidney (Stuchly et al. 1982a), although both of these were performed at or near to physiological temperatures. For completeness, the frequencies and temperatures that they covered are given in Table 3.3, and shown together with Burdette's measurements in Figure 3.1.

Table 3.3

Dielectric Measurements of Kidney Tissue

Reference	Animal	Temperature °C	Frequency GHz	Conditions
Brady et al. 1981	Cow	+30	2, 3, & 4	in vitro
Stuchly et al. 1982	Cat	+35	0.01-1	in vivo

The problem of thermal runaway, and the need for dielectric property data is recognised by the food industry, which uses microwave heating systems for various thermal processing operations. Metaxas and Meredith (1983; pp48-58) review the data which is available for frozen foodstuffs. One relevant industrial process is 'tempering' in which the product is heated to just below the melting point. A pamphlet issued by the Electricity Council (1981) describes an industrial case history in which frozen meat was warmed (tempered) from -18°C to -4°C using microwave heating at 896MHz.

Mudgett et al. (1979) have measured the dielectric properties of several frozen meats at -40°C and -20°C at fixed frequencies of 300MHz, 915MHz and 2.45GHz. The dielectric properties were generally predicted by a physical-chemical model; all the meats measured becoming lossier with increasing temperature.

3. The Need for Further Dielectric Measurements

Although the dielectric properties of the various pure cryoprotectants have been studied; there seem to be no published dielectric measurements on 'complete' cryoprotectant solutions over the relevant frequency and temperature range. Similarly, many dielectric measurements have been made on biological materials which are relevant to organ cryopreservation, but there are still large areas of the temperature and frequency range left unexplored, as can be seen from Figure 3.1.

Because of the increased penetration depth, there is good reason to expect that warming would be more uniform at frequencies below 1GHz. However, it would be useful to overlap 2.45GHz; this is the microwave oven frequency which has been used in several previous attempts at rapid warming described in chapter 1. The low frequency limit is provided by the need to avoid the strong positive temperature coefficient of the effective conductivity which dominates below 10MHz. The temperature range investigated should be as large as is practical, but should obviously cover the phase transition which occurs around -10°C.

The next three chapters of this dissertation describe the measurement systems we have used to explore the remaining temperature and frequency range.

4. Review of Dielectric Measurement Techniques

There are a number of measurement techniques available for the determination of dielectric properties. This section reviews the techniques which are most suitable for biological materials including tissue, in order to survey the frequency range 10MHz to 3GHz.

4.1. Overview

Most measurement systems consist of a sample holder to contain the specimen, and instrumentation operating at radio or

microwave frequencies to measure some electrical parameter (or parameters) of the sample holder over the range of frequencies of interest. The dielectric properties of the specimen are then calculated from these measurements.

The key feature of any sample holder is that there should be a reasonably straightforward mathematical relationship between the electrical measurand and the permittivity to be measured. As a consequence of this, and because of the tight tolerances required for their manufacture, sample holder geometries are usually simple and highly symmetrical.

The instrumentation used is obviously dependent on the electrical parameter to be measured. Generally measurements are made in the frequency domain, although time domain instrumentation has been used in some systems. Increasingly, dielectric measurements are made using computer controlled semi-automated or fully automated instrumentation. Such methods allow sophisticated error correction techniques to be incorporated into the measurement procedure, and generally allow a much greater volume of data to be collected. Time domain methods also require some computational effort to transform the time domain responses to their equivalent frequency domain representation.

4.2. Transmission Line Methods

These are especially suitable for frequencies between 50MHz and 12GHz. Below 50MHz, conventional bridge systems are adequate (Field 1954). Above 12GHz, waveguide methods are more suitable when the problems created by higher modes in TEM transmission line become too severe. In these techniques, the dielectric material to be measured is made a part of a transmission line - often coaxial in cross-section. Measurements are made of the electrical properties of the composite transmission line. There are a variety of methods available, reviewed briefly below and in detail by Westphal (1954), Grant et al. (1980; pp75-120) and Stuchly and Stuchly (1980).

Figure 3.3 Four basic configurations for dielectric measurements.

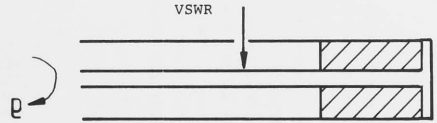

3.3a Roberts and Von Hippel

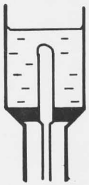

3.3c Bussey

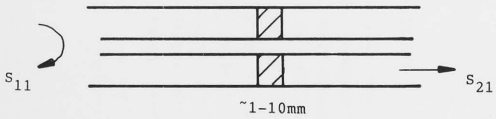

3.3b Nicolson and Ross

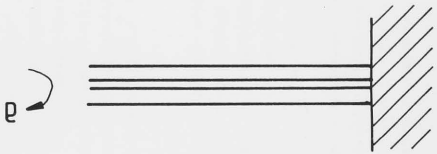

3.3d Burdette, Stuchly

In the technique due to Roberts and Von Hippel (Westphal 1954), the sample is placed at the end of a section of transmission line which is shorted at the distal end of the sample - see Figure 3.3a. The dielectric permittivity is determined by measuring the standing wave profile using a slotted line method (Lawinski et al. 1975, Grant et al. 1980 pp75-79). Alternatively, the reflection coefficient of the line can be measured using an RF bridge (Edwards 1982) or a time or frequency domain Network Analyzer.

A later development is the thin-sample technique; the sample replaces a thin section of the space between the conductors of the otherwise uniform transmission line, as in Figure 3.3b (Nicolson and Ross 1970). Measurement of the reflected or the transmitted wave amplitude and phase from the sample allow determination of the permittivity. Much of the published time domain work has been performed with this design of sample holder (Dawkins et al. 1979, Grant et al. 1980; pp101-120). A recent technique described by Bussey (1980) uses a shielded open-ended transmission line; the geometry is shown in Figure 3.3c.

The three methods described above correspond to three different known terminations on the distal end of the sample - short circuit, matched load, and open circuit.

4.3. Resonant Cavities

In these techniques, a small sample of the dielectric material is used to perturb the electromagnetic field in a resonant cavity, changing its resonant frequency. Measurements of a shift in frequency can be made extremely accurately; this is perhaps the most accurate dielectric measurement method. However, such systems are narrow band by their very nature, and consequently they are of limited use for surveying a range of frequencies. Macklis et al. (1975, 1979) used such a system for their measurements on cryoprotectants around 1.5GHz over a wide

range of temperatures.

4.4. Open ended probe

In this technique, an electrically short antenna is placed in contact with the dielectric material to be studied. The permittivity is determined from measurements of the input admittance made with a Network Analyzer. The antenna is made from semi-rigid coaxial cable; a short length of the inner protrudes to form a short monopole as shown in Figure 3.3d. Burdette et al. (1978a, 1978b, 1980a, 1980b, 1981) used such an antenna probe and an infinitesimal monopole - i.e. a plain open-ended probe - to make their measurements on tissue, and tissue perfused with cryoprotectant. Stuchly and Stuchly (1984) have made many measurements on biological materials using the open-ended probe (though not on perfused tissue).

Instead of measuring the input admittance of the probe, it is possible to make the probe part of a resonator (Tanabe and Joines 1976, Stuchly et al. 1978), although this method suffers from the same bandwidth limitation discussed above.

5. Choice of Measurement System

Clearly, resonant cavity methods are wholly unsuitable for a survey of a broad range of frequencies. This leaves the transmission line methods and the open-ended probe. The open-ended probe technique is superficially similar to the shielded open circuit technique described by Bussey (1980), however there are important differences between the two methods. The open-ended probe is essentially a transmission line abruptly terminated by a semi-infinite[‡] volume of the dielectric material to be measured. Consequently little or no sample preparation is required allowing in vivo and in vitro tissue measurements to be made if required. This is in contrast to the transmission line methods which require a sample of very specific geometry to be cut, which can be extremely difficult with semi-solid materials such as kidney tissue.

‡ Large, but finite in practice.

Although the open-ended (antenna) probe techniques allow simple sample preparation, the problem is that the exact field solution is extremely complex and an approximate equivalent circuit is required to determine the permittivity from the measured input impedance of the probe. In contrast, providing the transmission line sample holder is carefully designed, the exact field solution is fairly simple, and the permittivity can be accurately determined.

In this work, we have used two separate dielectric measurement systems:

a) Over the period 1982-1984 we concentrated on a transmission line system using the thin sample method, and time domain instrumentation. This system is the subject of chapter 4.

b) In late 1984, because of problems with the other system, and the availability of a frequency domain Network Analyzer, effort was directed towards a system based on the open-ended probe - with much greater success. The theoretical basis of the measurement system is described in chapter 5, and the practical details and performance in chapter 6.

The results obtained using the second system on perfused tissue and cryoprotectants are the subject of chapter 7.

Chapter 4

Dielectric Measurements Using a Strip-Line Sample Holder

This chapter describes the first of the two dielectric measurement systems that have been investigated in this work. The measurement system described here consists of a two-port transmission line sample holder, together with suitable time domain instrumentation. A 'strip-line' sample holder was used to allow simple preparation of tissue samples. Measurements of one or more of the scattering parameters of the resulting composite transmission line allow the dielectric properties of the unknown material to be determined.

Section 1 gives an overview of time domain dielectric measurements and describes the basic theory behind this measurement system. Section 2 describes the time domain instrumentation and the digital recorder used for practical dielectric measurements, together with the initial experimental arrangement used. Techniques designed to reduce the uncertainty in the measured permittivity and some of the results obtained are described in section 3. Finally, section 4 summarizes the problems with the system, and gives some suggestions for its improvement.

1. Time Domain Dielectric Measurements

1.1. History

Time domain measurement systems have been used historically for the measurement of low frequency dispersions. In 1969, Fellner-Feldegg introduced time domain spectroscopy for the measurement of the dielectric properties of liquids in the RF and microwave frequency range. Since this introduction, there have been many improvements in the data analysis and instrumentation (Grant et al. 1978; pp101-102, Dawkins et al. 1979, 1981a, 1981b).

Figure 4.1a Ideal transmission line sample holder. The dielectric sample forms a purely longitudinal discontinuity in the dielectric filling of otherwise uniform guide.

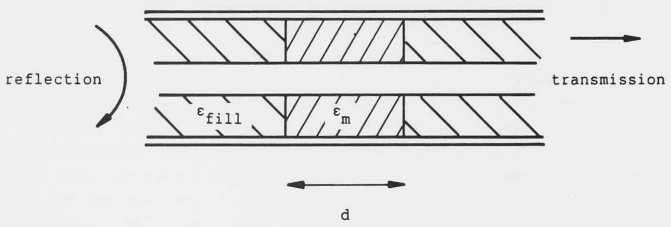

Figure 4.1b Signal flow graph of the geometry above.

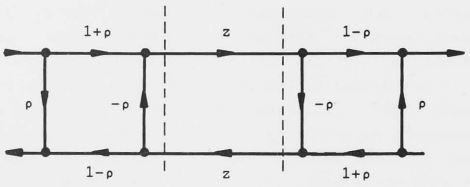

Figure 4.1c Reduced version of Figure 4.1b.

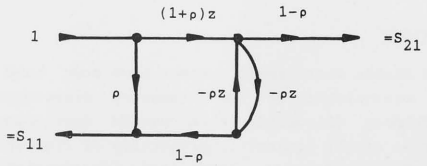

The general principle behind most time domain dielectric measurement systems is to replace a short section of the normal dielectric filling of an otherwise uniform coaxial transmission line by a sample of the dielectric to be measured, as shown in Figure 4.1. Many systems use precision air-filled coaxial line, this is fine for solid samples - semi-solid or liquid samples must be confined by teflon or similar spacers.

The electrical properties of the two-port formed from the composite transmission line are measured by firing a fast-rising (~30ps) step waveform down the line towards the sample holder and recording the incident pulse and the reflected and/or transmitted pulses.

During the evolution of time domain dielectric spectroscopy, various approximate methods of analysis were developed to permit calculation of the dispersion parameters directly from the time domain waveform (Fellner-Feldegg 1972, van Gemert 1974). Although this method of analysis is useful for qualitative measurements, in general more accurate results can be obtained by calculating the equivalent frequency domain scattering parameters of the sample holder, and using these to find the permittivity.

1.2. Time Domain Scattering Measurements

Techniques for measuring scattering parameters in the time domain are well established and time domain network analyzers have been described by many workers (Adam 1969; pp457-489, Nicolson and Ross 1970, Nicolson *et al*. 1972, Andrews 1978, Rigg and Carroll 1980).

Briefly, a step or impulse-like waveform, i(t), is impressed upon the network to be investigated - a two-port here. The reflected waveform $w_{11}(t)$, and the transmitted waveform $w_{21}(t)$ are essentially the time domain convolution of the input waveform i(t) with the reflection impulse response[+] $s_{11}(t)$ and the transmission impulse response $s_{21}(t)$ of the two-port. The frequency domain scattering parameters S_{11} and S_{21} of the two-port are calculated from the discrete Fourier transform (DFT) of the recorded

waveforms; the permittivity can be obtained from either S_{11} or S_{21}.

1.3. Calculation of Permittivity from Scattering Measurements

This section describes how the permittivity of the material in the sample holder, ε_m, is related to the scattering parameters of the sample holder. Define ρ and z as follows:

$$\rho = \frac{r - \sqrt{\varepsilon_m}}{r + \sqrt{\varepsilon_m}} \quad (4.01) \quad \text{and} \quad z = \exp -j\frac{\omega d}{c}\sqrt{\varepsilon_m} \quad (4.02)$$

where r is the characteristic impedance of the empty sample holder normalized to the impedance of the coaxial line, ω is the angular frequency, d is the length of the sample, and c is the free space velocity of light. The relative permeability is unity for biological materials, and for the idealized geometry shown in Figure 4.1a, $r = \sqrt{\varepsilon_{fill}}$. The signal flow graph for the two port is shown in Figure 4.1b. To perform a measurement, port 1 is excited by an incoming wave of unit amplitude, port 2 is matched. The scattering coefficients of the two-port can be obtained from the reduced flow graph of Figure 4.1c using standard signal flow graph reduction techniques (Adam 1969; pp86-106) yielding

$$S_{11} = \frac{\rho(1-z^2)}{1-\rho^2 z^2} \quad (4.03) \quad \text{and} \quad S_{21} = \frac{z(1-\rho^2)}{1-\rho^2 z^2} \quad (4.04)$$

Either of these expressions may be used to obtain the permittivity, however, the numerical solution of a transcendental equation in ε_m is required in both cases. Nicolson and Ross (1970) showed that if measurements of <u>both</u> S_{11} and S_{21} are available, then the permittivity can be directly calculated in closed form from

$$\varepsilon_m = r^2 . \frac{(1 - S_{11})^2 - S_{21}^2}{(1 + S_{11})^2 - S_{21}^2} \quad (4.05)$$

---

† The 'reflection impulse response' is the reflected signal that would be observed if a true impulse was impressed upon the network.

Figure 4.2 Strip-line sample holder geometry.
(a) Top view showing cutaway section through RG402 coaxial cable. (b) Sample holder cross-section

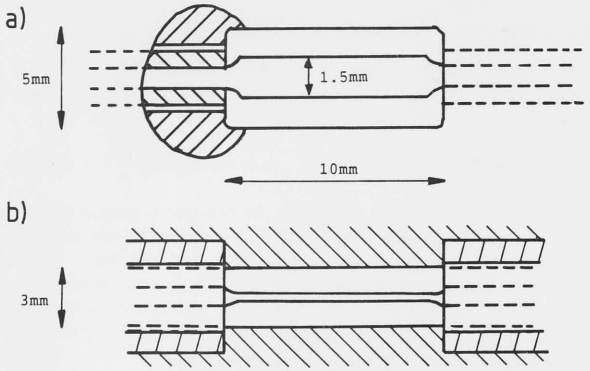

(c) Exploded view. The top and bottom walls of the sample holder are formed from small 'anvils' attached to two cooling blocks which are bolted around the middle section. Only the lower block is shown here.

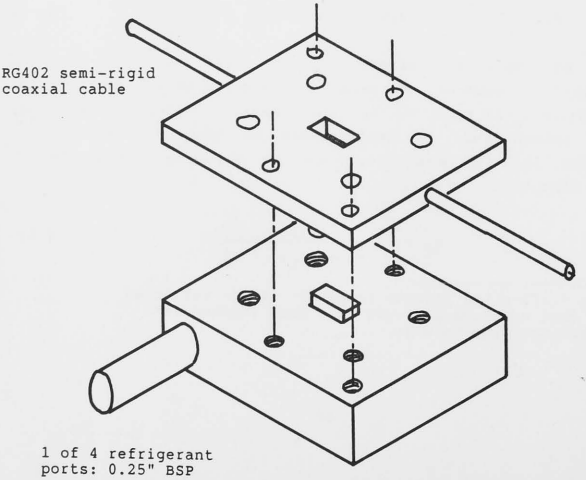

or alternatively

$$\cos\frac{\omega d}{c}\sqrt{\varepsilon_m} = \frac{1 + s_{21}^2 - s_{11}^2}{2s_{21}} \qquad (4.06)$$

though (4.05) is preferred because of the ambiguity inherent in (4.06) and also because it is unnecessary to know the frequency accurately, or the length of the sample holder. The normalized impedance of the empty sample holder, r, can be determined from a single measurement of a known dielectric, since it occurs merely as a scaling factor here.

1.4. Design of the Strip Line Sample Holder

Up to now, the discussion has implied a wholly coaxial geometry is required. Provided the sample forms a longitudinal discontinuity in the guiding structure, the analysis applies to any two-conductor system in which the TEM mode‡ is dominant.

From the start, our aim has been to measure the dielectric properties of tissue perfused with cryoprotectant over a range of temperatures. A particular problem presented by a coaxial line sample holder is that of sample preparation - we did not believe we could reliably cut samples of tissue to fill a narrow annular volume. After some experimentation, we decided that it was fairly easy to cut rectangular 'slabs' of tissue - this was the major factor which influenced the choice of sample holder, the final version of which is shown in Figure 4.2. Temperature control is provided by a refrigerant which flows through cooling channels cut into the lower and upper blocks, though only the lower block is shown here.

The sample holder is essentially a 10mm length of 3mm by 5mm 'rectangular coax' (Cruzan and Garver 1964) tapered to cylindrical coaxial line at either end. The length was chosen as a compromise

‡ With small modifications, the analysis may also be used for a single TE or TM mode in suitable waveguide (Ligthart 1983).

between the low frequency sensitivity of the sample holder and the available tissue volume. Our original design used a wider inner conductor - we had hoped to attain sufficient accuracy by treating the sample holder merely as a lumped-element parallel capacitance, but this circuit model proved inadequate above about 200MHz.

It is very difficult to fabricate long lengths of such rectangular guides, and in any case most of the instrumentation uses coaxial connectors, so the transition from a rectangular to a coaxial guiding structure is inevitable at some point in the system. This transition necessitates the existence of higher modes which appear as small discontinuity capacitances (TM modes) and inductances (TE modes) in the equivalent circuit of the sample holder (Whinnery and Jamieson 1944). These additional reactive elements have not been incorporated into the equivalent circuit model of the sample holder - this is an area that requires further investigation.

The rectangular inner conductor of the sample holder was made by removing 10mm of the outer and dielectric from the mid-portion of a 260mm length of RG402 (0.141") semi-rigid cable; the exposed inner was crushed flat to final dimensions of 1.5mm by 0.5mm. The cable was heat treated (to reduce shrinkage of the PTFE dielectric), the inner gold plated (to prevent corrosion), and standard female SMA connectors attached to the ends. The remainder of the sample holder is built from brass, this is also gold plated on the surfaces that form the walls of the rectangular cell.

2. Instrumentation for Time Domain Measurements

Sampling oscilloscopes capable of measuring picosecond pulse phenomena were first introduced by Hewlett-Packard in the mid-1960's. Since that time, sampling oscilloscopes have been used in a broad range of in network and antenna measurement

applications (Bennett and Ross 1978).

2.1. Time Domain Network Analyzers

The techniques discussed in the previous section need scattering parameter measurements of a two-port sample holder, thus a Network Analyzer is required. Commercially available frequency domain Network Analyzers are expensive, and the native instrument generally requires error correction techniques to reduce the systematic errors created by the hardware. Chapter 5 describes simple methods for performing this error correction for one-port measurements, however the situation is more complex for two-ports. In the frequency domain Network Analyzer, separation of incident and reflected signals is performed by a directional coupler, which inevitably has finite directivity. In the time domain version, this signal separation is performed by suitable lengths of delay line. Provided the output of the pulse generator used to investigate the system is time-limited, this corresponds to effectively infinite directivity.

Most previous workers have used sampling oscilloscopes manufactured by Hewlett-Packard; however we believe that Tektronix is now the only manufacturer of sampling oscilloscopes in the western world. For this work we have used the Tektronix 7000-series sampling oscilloscope system - specifically two S-6 'loop-thru' sampling heads (rise-time $\leq$ 30ps), two 7S11 sampling units, a 7T11 sampling sweep unit and a 7603 mainframe.

2.2. Sampling Oscilloscope Operation

The principles of sampling and sampling oscilloscope systems are described by Cochrane (1985). The detailed operation of the 7000-series sampling system is well described in the relevant manufacturers manuals, a brief summary is given here. The following description refers to the 'sequential' operating mode of the 7T11 which is the one used throughout, as the alternative 'random' mode has worse jitter performance and is not as suitable for digital recording techniques.

The sampling oscilloscope system reconstructs a necessarily periodic waveform by taking short-duration (~20ps) samples from the waveform at successively later and later instants with respect to the trigger signal. Each sample is acquired by a tunnel diode sampling bridge in the S-6 sampling head; the sampling instant is controlled by a strobe pulse from the 7T11 sweep unit.

One clear requirement for a time domain Network Analyzer is a means of recording and processing the trace produced on the sampling oscilloscope to produce the scattering parameters of the network under test. In sequential mode, the 7T11 can be modelled as a pulse generator with a voltage controlled delay time. That is, the delay between the arrival of a trigger pulse from some external circuit, and the instant at which the sampling bridge is opened is voltage controlled. In normal operation, this voltage control is provided by an internal slow (2-40Hz) ramp generator that sweeps through the range of delay times set by the 7T11 front panel controls. At the same time, the ramp sweeps the horizontal deflection of the 7603 to provide the display.

Recording the waveform is facilitated by an external scan ('EXT SCAN') input to the 7T11 sweep unit, and a vertical signal output ('VERT SIG OUT') from the 7S11 which amplifies and stores the sampling head output. Appendix 3 describes the details of the digital recorder used in this work to capture time domain waveforms, a summary is given below.

The recorder contains a 12-bit digital to analogue converter (DAC) which drives the EXT SCAN input of the 7T11 across the time window. A 10-bit analogue to digital converter (ADC) acquires data from the 'VERT SIG OUT' jack of the 7S11 at each time point that the DAC sets. The 7T11 gives an output, used by the 7603 mainframe for intensity modulation of the trace, which indicates that the current sample is being held by the 7S11 and so is suitable for display. This output is available from a rear panel jack ('GATE OUT') on the 7603 and it is used to synchronize data acquisition by the ADC. After a waveform has been captured, it is transferred to a BBC microcomputer and recorded on floppy disk; at the end of the experiment, the data is transferred to the

University IBM 3081 mainframe for subsequent processing.

The noise inherent in the sampling system can be reduced by signal averaging. There are two simple ways in which this averaging may be performed. In 'cyclic' averaging, the timebase is swept repetitively through the time window N_a times. At the end of each sweep, the array of ADC values obtained at each time point is summed into an accumulator array. After all the sweeps have been performed, each accumulated value is divided by N_a to obtain the required average.

In 'sequential' averaging, the timebase is swept across the time window once only. At each time point, the output signal is sampled N_a times, then divided by N_a before moving to the next point. Our digital recorder uses the latter algorithm which is faster because the time needed for the timebase to settle at each new time point (~0.3ms) is much longer than the time required to digitize a sample (64μs). Typically 1024 points were sampled from a 100ns time window with 256 summations per point - this takes about 17 seconds, two such recordings are required for each material.

2.3. Source Waveform

Many workers who have developed time domain dielectric measurement systems have used commercial step waveform generators, based on tunnel diodes, which generally have rise-times of the order of 30ps. The problem with these very wide-band sources is that the maximum step amplitude is the order of 250mV, this amplitude is reduced by passing through the delay lines needed to provide signal separation. The S-6 sampling head will accurately display up to 1V, consequently some dynamic range is lost. It is possible to make pulse sources using slower semiconductor devices (50-100ps rise-time) which produce higher voltages. The reduced bandwidth is more than adequate for this application and the higher output voltage means that the full dynamic range of the sampling head can be used even after the pulse has passed through long delay lines.

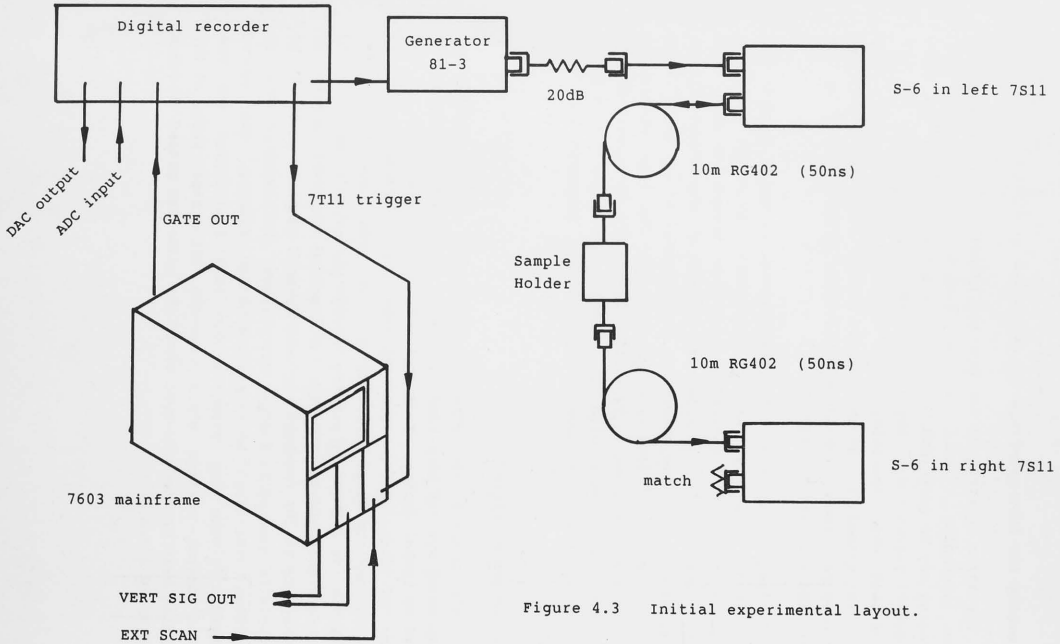

Figure 4.3 Initial experimental layout.

Several pulse generators were used for this work, the majority of which were constructed by H C Reader in this department (Reader 1985). The generators produce quasi-impulsive waveforms, which approximate to a decaying exponential, using a cascaded pulse sharpening technique: a TTL pulse generated by the digital recorder is sharpened by two avalanche transistor stages. The final stage uses a step recovery diode to perform final pulse sharpening, together with a schottky diode shaping network. The results presented later in this chapter were obtained with pulse generators 81-3 and 84-6M, both of which had peak output voltages of about 12V, rise-times of better than 100ps, and FWHMs of about 400ps.

2.4. Triggering

The sampling system requires a repetitive trigger to function correctly. In our system, this is derived from the crystal controlled clock of the digital recorder. The clock pulse (after TTL division) has a 64μs repetition period; this drives an avalanche pulse generator which provides both the oscilloscope trigger, and the drive to the final stage of the pulse sharpener. The 7T11 requires the trigger to be at least 70ns in advance of the waveform to be displayed, so the pulse sharpener drive is taken via a suitable length of delay cable.

2.5. Initial Experimental Layout

In order to obtain scattering parameters down to 10MHz using the DFT, uncluttered waveforms which extend over 100ns are required. Various system imperfections, such as reflections from the pulse generator, connectors and sampling heads, set the time 'window' during which the reflected or transmitted waveforms can be recorded cleanly. Two 10m lengths of RG402 semi-rigid cable (50ns propagation delay) are used in the transmission and reflection halves of the system which produce the required 100ns time windows.

Figure 4.3 shows the initial experimental layout used. The waveform incident on the sample holder was determined (as a

calibration measurement) by replacing the sample holder by a matched tee which has known return and insertion losses. The effect of the attenuation and dispersion (but not reflection) in the delay lines is removed using such a reference scheme. The insertion loss produced by a 10m length of such line is about 7dB at 2GHz.

Note that the two connectors which join the sample holder to the delay lines remain. Although the return loss of these connectors can be made very small using carefully assembled standard SMA connectors (better than -40dB below 3GHz), the resulting reflection is comparable with that produced by the empty sample holder alone.

2.6. Initial Results

The results from this system, which were obtained using a prototype digital recorder with an 8-bit ADC, were very disappointing. Although it seemed that reasonably accurate measurements of the scattering parameters had been made, the corresponding measured permittivity was hopelessly wrong, forcing the conclusion that greater accuracy was required. This was one of the reasons for constructing the improved digital recorder described in the previous section. Three further problems were identified with the instrumentation: the time drift inherent in the 7T11 timebase, the absolute calibration of the 7T11, and the errors introduced by the connectors on the sample holder. Another way to improve the accuracy of the measured permittivity is to make more use of the information implicit in the two scattering parameter measurements. The system improvements are described in the following section.

Figure 4.4 Recorded waveform from HP8406 100MHz crystal comb generator. Pulse rise-times are about 60ps.

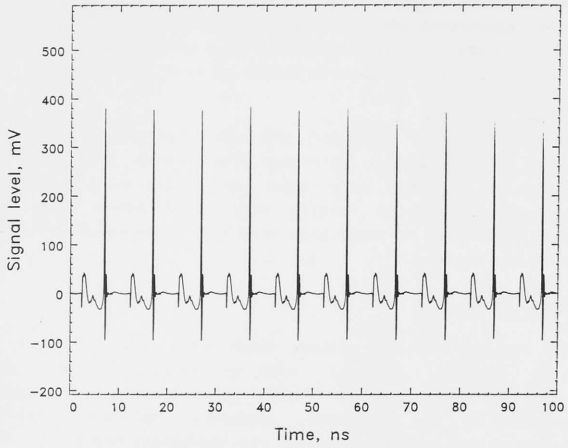

Figure 4.5 Measured time drift for 7000-series sampling system over a two minute period.

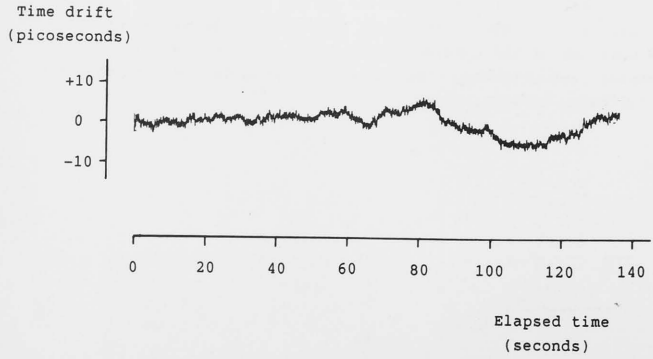

3. System Improvements

3.1. Time Calibration

Calibration of the 7T11 timebase was performed by recording the waveform produced by an HP8406 100MHz crystal comb generator, and using the apparent spacing between the fastest edges of the recorded waveform (which are 10ns apart) to correct the frequency scale. Figure 4.4 shows such a calibration waveform from the 8406. Calibration of the absolute vertical deflection voltage recorded by the ADC was only approximate. Accurate absolute calibration is unnecessary because when calculating either scattering parameter, the ratio of the DFT of two waveforms measured with the same sampling head is taken. Different vertical range settings were occasionally required for the two waveforms, the settings were measured to be within 0.7% on adjacent ranges e.g. 100mV/div to 50mV/div.

3.2. Time Drift Correction

Unfortunately, all sampling oscilloscopes have some drift in the timing zero. Figure 4.5 shows a measurement of drift versus elapsed time for the 7000-series sampling system: the short term drift several hours after power up is less than 10ps over a 2 minute period. Provided the time taken to record the waveform is short, this drift appears as a random offset in the true time position of the waveform with respect to some previous recording e.g. the incident pulse. In the frequency domain, this time offset corresponds to a linear phase error - at 1GHz, 50ps of time drift corresponds to 18° of phase error, which is quite unacceptable. This sort of drift can easily occur during a series of measurements that might take some tens of minutes, or even hours.

This drift problem was recognised early in the development of time domain measurements. Nicolson and Ross (1970) used a three point scanning technique for active correction of the time drift. Before recording data at each new time point, the position of two fixed points on the waveform were checked, the timebase was

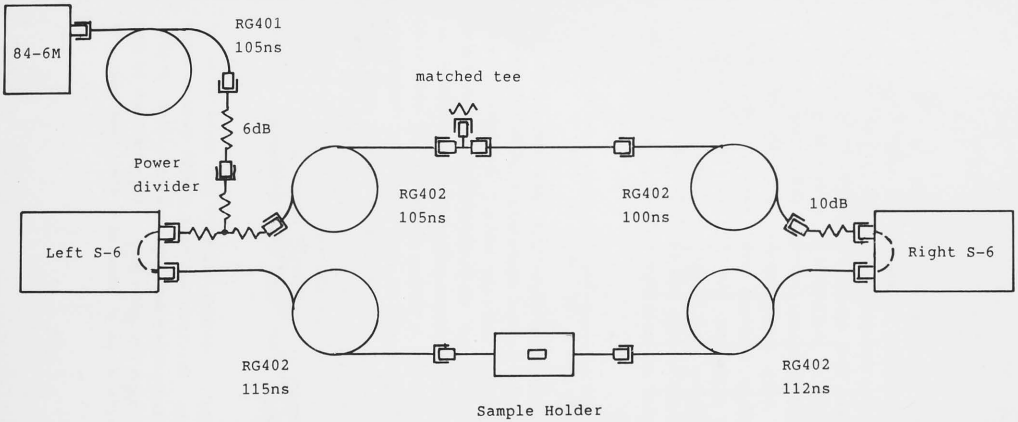

Figure 4.6 Experimental layout for time domain dielectric measurements with time drift correction. The details of the recorder and oscilloscope interconnections are the same as those of Figure 4.3.

corrected if they had drifted. This is obviously very time consuming: 256 points with 4 summations took 7 minutes, however, they were able to stabilize the drift to within 1ps with this scheme. Similar (faster) schemes have been used by other workers (Dawkins et al. 1979)

Because the frequency range we intended to cover was lower than that used by Nicolson and Ross, we used a passive method which relies on the drift being small during the 17 seconds required to acquire a single waveform. In order to correct for time drift, an additional set of delay lines were used in the modified experimental arrangement as shown in Figure 4.6. This reference set are in close thermal contact with the original set of delay lines, however a matched tee replaces the sample holder. The tee piece produces a timing reference pulse on both transmitted and reflected waveforms, thus each waveform contains a pulse which is in the same electrical position on every waveform, regardless of the drift. The reference lines are about 10ns shorter than the measurement lines so that the reference pulses arrive first. The reference pulse is removed from the recording before evaluating the DFT by simply setting the first 10ns of the time window to zero.

The drift is not corrected at the time the measurement is taken, the amount of drift is calculated subsequently by an autocorrelation technique. Correction is deferred until the DFT of the waveform has been evaluated; the DFT is multiplied by a suitable linear phase term. The resulting time window stability is better than 5ps for time drifts of less than 100ps.

Figure 4.7 shows the waveforms recorded from the system shown in Figure 4.6, including the timing reference pulses. The diagram shows the reflection and transmission reference waveforms, and the two 'measurement' waveforms recorded from the sample holder filled with ethanediol.

Figure 4.7
Measured waveforms from the time domain system.

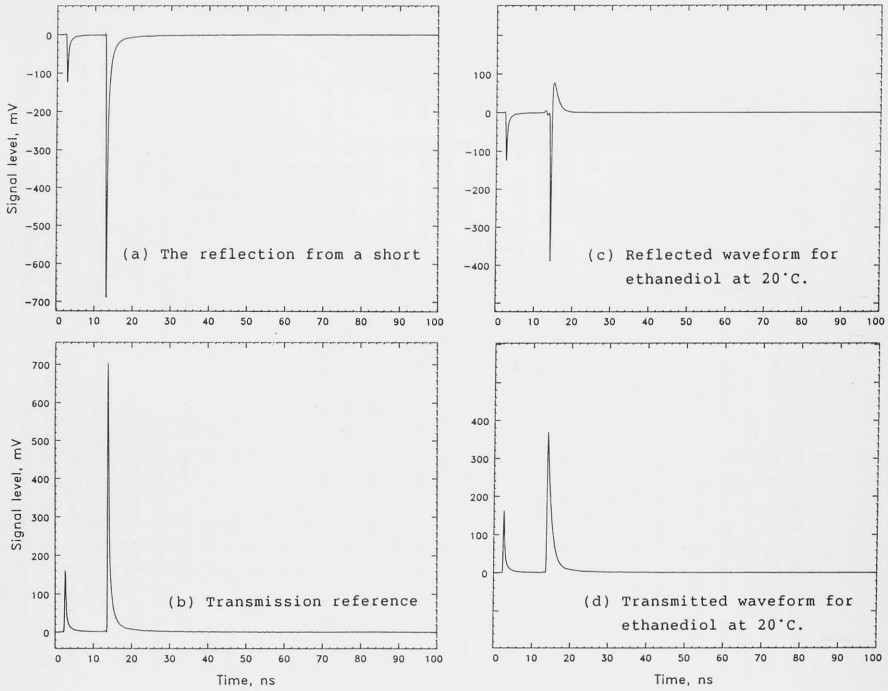

3.3. Uncertainty Reduction by Mapping Techniques

As noted previously, there are two independent ways to calculate the permittivity if both S_{11} and S_{21} are known. Consequently there is some redundant information which can be used to reduce the error. Ligthart (1983) describes a mapping algorithm which uses uncertainty estimates in scattering parameter measurements to reduce the uncertainty in the calculated permittivity. First, eliminate ε_m between (4.05) and (4.06) to obtain

$$h(S_{11}, S_{21}, \frac{\omega dr}{c}) = \frac{1 + S_{21}^2 - S_{11}^2}{2S_{21}} - \cos\frac{\omega dr}{c}\left[\frac{(1 - S_{11})^2 - S_{21}^2}{(1 + S_{11})^2 - S_{21}^2}\right]^{\frac{1}{2}}$$

$$= 0 \qquad (4.07)$$

Thus given a measurement of S_{21} and the value of $\omega dr/c$, it is possible to determine the value of the corresponding S_{11}. The algorithm proceeds as follows. Given uncertainties $\Delta S'_{21}$ and $\Delta S''_{21}$ in the real and imaginary parts of S_{21}, an uncertainty rectangle can be constructed around the measured value S_{21m}, inside which the true value S_{21t} must lie. A similar region can be constructed in the S_{11} plane, these two regions are shown side-by-side in Figure 4.8a. In fact square uncertainty regions were used* i.e. $\Delta S'_{11} = \Delta S''_{11} = \Delta S_{11}$ and $\Delta S'_{21} = \Delta S''_{21} = \Delta S_{21}$.

Now, using equation (4.07), map each vertex of the uncertainty region from the S_{21} plane into the S_{11} plane, as in Figure 4.8b. Provided the uncertainties are small, so that the relevant derivative of h is relatively constant around S_{21m}, the intersection between these two regions contains S_{11t}, and the area

* It is likely that phase errors due to time drift would be much greater than magnitude errors. Perhaps a better choice would be to calculate the vertices of the uncertainty region accordingly.

Figure 4.8 Mapping algorithm for uncertainty reduction.

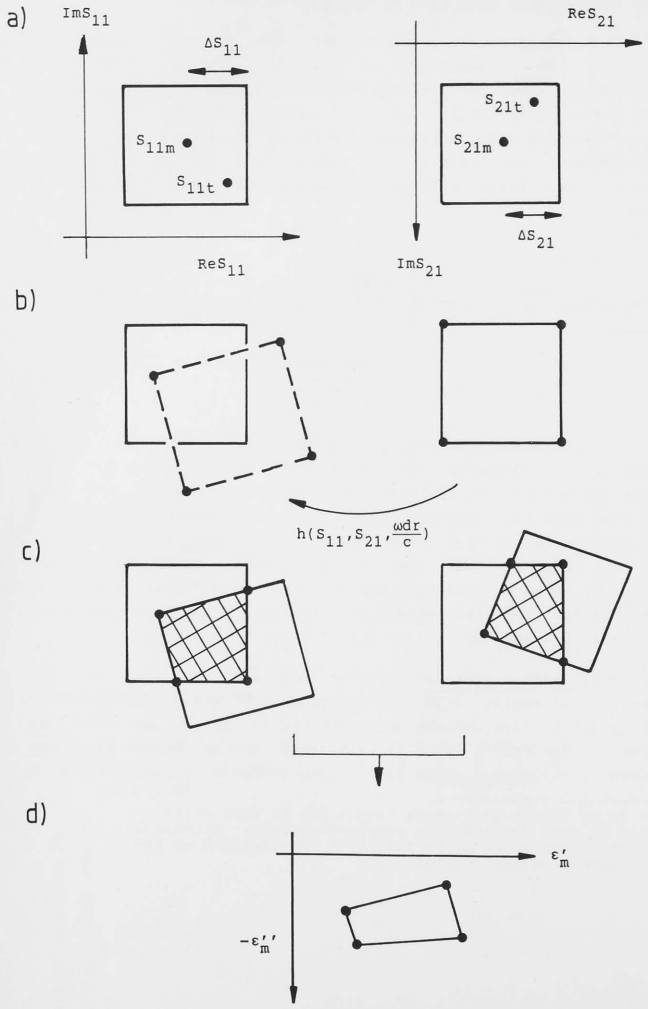

of the combined uncertainty region is reduced, as shown in Figure 4.8c. The same procedure is repeated, mapping the S_{11} uncertainty region into the S_{21} plane. The new vertices of the reduced uncertainty region in the S_{11} plane are mapped into the S_{21} plane, finally the permittivity is calculated using corresponding pairs of vertices in (4.05), producing an uncertainty image in the ε_m plane (rarely rectangular) which is shown in Figure 4.8d.

Ligthart uses the first term of a Taylor expansion for h to express S_{11} in terms of S_{21} and $\omega dr/c$. Our implementation of his scheme used a more accurate numerical technique (Newton's method) to perform the mapping, because initial simulation studies suggested that the approximate version was not always reliable. Also many checks were built in to ensure that the images of the uncertainty regions in the S_{11} and S_{21} domains were properly connected, and both permittivity images were evaluated and checked for consistency. Between three and eight vertices are generated by the mapping procedure; the results given later in the chapter are plots of the average value of the vertices.

The measurement uncertainties are larger at higher frequencies because the effects of the connector discontinuities, wall losses and residual time drift all increase with frequency. All but the latter are systematic uncertainties, nevertheless, there appeared to be no sensible way to predict upper bounds on how big the region should be without being excessively pessimistic. So, we decided to allow the size of each uncertainty region to be reduced alternately until they ceased to produce an intersection region. The previous intersection region is then used to calculate the uncertainty region in the permittivity plane. The mapping process is computationally expensive, so only a 5-2-1 sequence of uncertainties are used, in the range 0.05 to 0.0005. Approximately 30 seconds of CPU time was required to evaluate 200 frequency points.

Now it is certainly possible that this process might underestimate the uncertainty associated with a particular measurement, and thus exclude the true value S_{11t} or S_{21t} from the

Figure 4.9 Measured permittivity of ethanediol at 20°C using the strip-line sample holder with SMA connectors. The dotted line is calculated from the dispersion parameters for ethanediol given by Jordan et al. (1978).

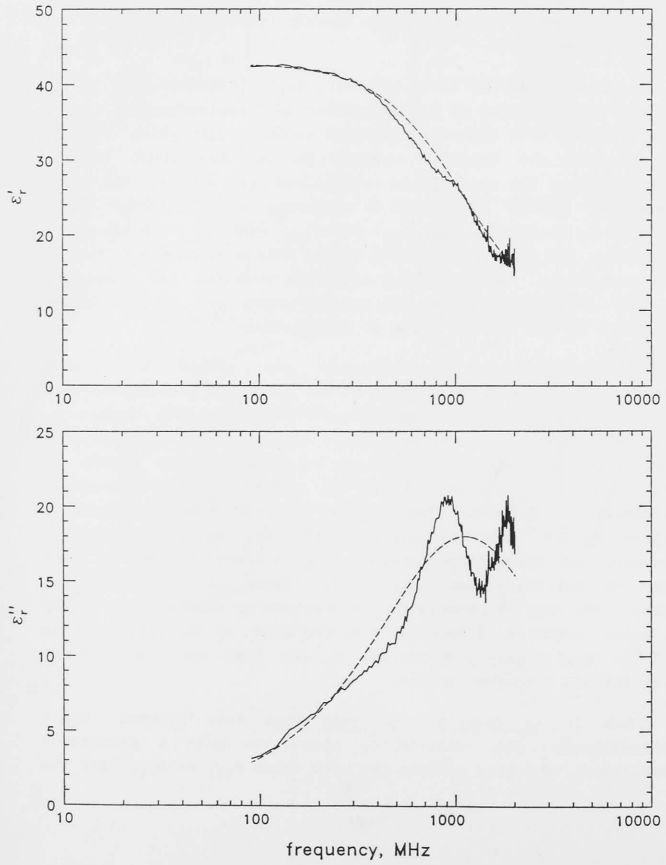

intersection region. However, the extended algorithm can be considered as a way of making the measurements of S_{11} and S_{21} consistent - within the constraints of the simple model for the sample holder.

3.4. Determination of Sample Holder Parameters

Section 1.3 showed that the permittivity can be determined from two simultaneous scattering measurements given only the characteristic impedance of the empty sample holder. However, the mapping procedure described above uses both parameters of the sample holder - the normalized impedance, r, and the length d. In principle, these two parameters can be found from accurate measurements of the sample holder dimensions. However, it is difficult to account for the effect of the tapered inner, and the transition from rectangular to coaxial guide. Instead, the effective values of r and d were found from a measurement of the sample holder filled with ethanediol. The sum of the squared relative errors in the scattering coefficients is minimized with respect to these two parameters over the frequency range 10MHz to 2GHz. The error is evaluated for each trial value of r and d by computing the theoretical scattering coefficients using (4.01-4.04) and the permittivity of ethanediol from the dispersion parameters given by Jordan et al. (1978).

3.5. Connector Problems

Despite all the enhancements to the measuring system, the performance of the system was still poor. Figure 4.9 shows the measured permittivity of ethanediol calculated from the time domain measurements shown in Figure 4.7. We attributed the bizarre oscillation in the permittivity to the SMA connectors on the sample holder.

At this point in the development of the system, several attempts were made to find an equivalent circuit model for the connectors so that their effect could be removed numerically. Several different models were tried; for example, the mated connector pair was modelled as a short length d_c of mismatched

Figure 4.10 Measured permittivity of ethanediol at 20°C using the strip-line sample holder with no connectors. The dotted line is calculated from the dispersion parameters for ethanediol given by Jordan et al. (1978).

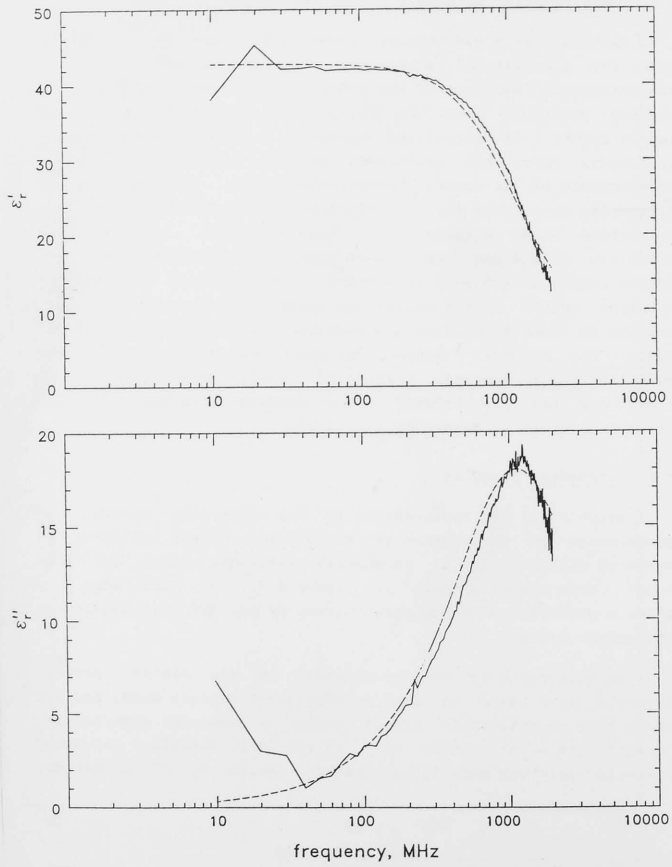

line of normalized impedance r_c. The model parameters r_c and d_c were calculated from separate time domain measurements of the connectors, and the resulting parameters used to calculate the coefficients of scattering matrices to represent each connector pair. These 'connector matrices' were then used to correct the scattering measurements, yielding the scattering coefficients of the sample holder. This method did improve the accuracy of the system, in that the amplitude of the wild oscillation shown in Figure 4.9 was reduced by at least 50% across the frequency range.

There is little doubt that the errors are caused by the SMA connectors. Figure 4.10 shows a similar measurement made on ethanediol using an earlier version of the sample holder which had no connectors at all. This sample holder was constructed by making a butt-joint between the flattened inners of the two 10m delay lines. The butt-joint was bridged by a thin layer of solder, forming a continuous line, free from connectors over the 100ns time window required. The resulting permittivities show good agreement with the measurements of Jordan et al. (1978) from 40MHz to 2GHz.

4. Conclusions and Suggestions for Further Work

Despite the improvements to the measurement system described on the previous pages, it became apparent that it was impractical to perform accurate dielectric measurements using the strip-line sample holder. This section explores the reasons for this, and offers suggestions which should allow a more accurate system to be constructed.

4.1. Time Domain Measurement System

Some improvements can be made to the instrumentation - these include modifying the digital recorder so that both reflected and transmitted waveforms can be recorded simultaneously, and exploring active correction of the time drift during experiments. It is also clear that the addition of a fast microcomputer, so that DFTs could be performed in a reasonable time, would improve

the turn-round time between recording a measurement and obtaining the permittivity (currently several hours).

4.2. Strip-Line Sample Holder

As Figure 4.10 shows, the existing instrumentation and the strip-line sample holder can be used for making reasonably accurate dielectric measurements. However, there are some problems with this design.

a) First, although sample preparation sounds reasonably simple, it is in fact quite difficult to cut a rectangular slab of tissue to fit into the sample holder with no air pockets, because of the elastic nature of kidney tissue.

b) Measurements on liquids are made particularly difficult because the sample holder leaks, albeit slowly.

c) The rectangular to coaxial discontinuities are not particularly attractive; their effect on the sample holder model certainly needs further investigation.

It is clear that a wholly coaxial design would be an improvement for both b) and c), however, the sample preparation problem remains. It would be possible to mash up the tissue, so as to fill the annular volume, however, little is known about the effects of such treatment on the dielectric properties. Dawkins et al. (1981c) have made tissue measurements over 0.1-6GHz with a coaxial sample holder based on a 2mm section of 7mm precision air line. However, the magnitude of S_{11} from the sample holder scales as the sample length at low frequencies - longer sample holders are required to get down to 10MHz. Also it would be very difficult to construct the long lengths of delay line required for low frequencies without using adapters, and thus introducing further reflections into the system.

It is possible to avoid the sample preparation problem altogether using one of the probe techniques mentioned in the last chapter, and reviewed in greater depth by Stuchly and Stuchly (1980, 1984). The exact theory of these probes is much more

complicated than that of the ideal transmission line sample holder, nevertheless, good accuracy may be obtained with approximate equivalent circuit models. The permittivity can be measured either in the frequency domain or in the time domain - both of these possibilities are explored in the following chapters.

4.3. Connectors

The previous section showed the dramatic improvement in accuracy possible if the connectors are removed from the sample holder. However, the fragility of the butt-jointed inner conductors of the two delay lines was a significant problem, particularly if the temperature of the sample holder was changed. One alternative to omitting the SMA connectors altogether is to replace them with better ones. It is possible to obtain such connectors, though they are extremely expensive: Amphenol produce a range known as 'APC-3.5' that are suitable for attachment to RG402 cable[#]. Another alternative is to pursue connector modelling, however, measurement of the connector scattering parameters is not particularly accurate because the reflection from an SMA connector is of the same order as the reflections from the inhomogeneities in the delay line.

Perhaps the best option is to develop a measurement system which incorporates all the system errors into two scattering matrices (one for each arm). This approach, as applied to one-ports (an open-ended coaxial probe), is the subject of the next chapter.

60-70 pounds each (March 1984 prices)

Chapter 5

Dielectric Measurements with an Open-Ended Coaxial Probe:

Part I - Theory

This chapter concerns the theory and implementation of a dielectric measurement system for biological materials based on a probe made from a length of open-ended semi-rigid coaxial cable. In use, the probe is placed in contact with the material under investigation and measurement of the probe admittance allows the determination of the dielectric permittivity. One of the major advantages of the technique is that no sample preparation is necessary, allowing measurements to be performed *in vivo* if required.

Electrically short antennas were first used for the measurement of permittivity and permeability towards the end of the 1950's (Smith and Nordgard 1985). The open-ended coaxial probe was introduced as a measurement technique by Tanabe and Joines (1976). Burdette *et al*. (1980a) developed the technique further and made many measurements of the dielectric properties of various tissues and cryoprotectants - see the review in chapter 3. Stuchly and Stuchly (1984) have investigated the open-ended probe in detail, both theoretically and experimentally.

This chapter reviews previous work on the open-ended probe, briefly describes the measurement system we have used, and presents the theory for our own dielectric measurements. First the geometry and manufacture of the open-ended probe used in this work is described. Section 2 investigates the electromagnetic fields and equivalent circuit of the probe, and shows how measurements of the probe input admittance are related to the dielectric permittivity. High frequency admittance measurements are the subject of section 3 and an error correction method is described which can be used to improve the accuracy of such measurements. Section 4 contains the derivation of a new

Figure 5.1a Dimensions of the RG401 coaxial probe.

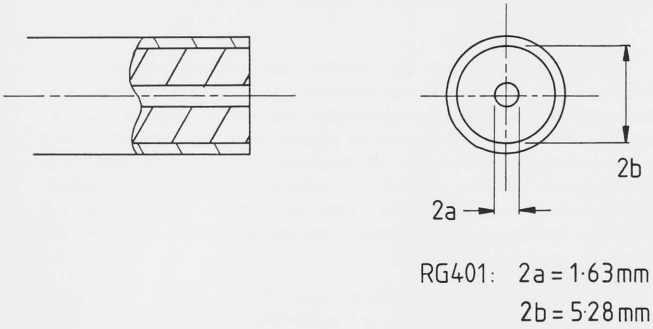

Figure 5.1b External view of completed RG401 probe with a male Type-N connector.

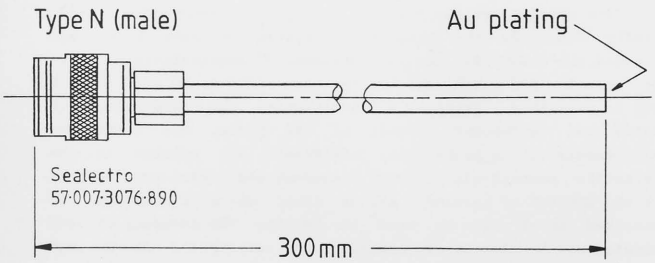

simplified procedure for performing error correction and identifies two important linearity properties inherent in this error correction technique. The application of the technique to dielectric measurements is explained in section 5, and a numerical example using measured data is given in section 6. Section 7 is an uncertainty analysis for the dielectric measurement system, the evaluation of the experimental uncertainties is deferred to the next chapter, together with a more detailed account of the experimental apparatus.

1. Open-Ended Probe Geometry and Manufacture

1.1. Geometry

All the probes used were constructed from standard PTFE filled semi-rigid coaxial cable, with a (nominal) characteristic impedance of 50 ohms. In much of our work we have used the cable designated as RG401 (Sealectro Ltd.), whose dimensions are shown in Figure 5.1a.

There is an inverse relation between the probe diameter, and the lowest frequency at which useful measurements can be made. However, the larger the probe, the larger the volume of material interrogated, so the choice of probe dimensions is necessarily a compromise. RG401 allows us to go down to about 50MHz, with sample volumes of approximately 20ml (lossy materials).

1.2. Manufacture

Initially, the cable is cut into 300mm lengths. To relieve the stresses built into the semi-rigid cable during its manufacture, it is cycled in temperature from -79°C to +25°C many times, as recommended by the supplier (Sealectro 1984). Heat treatment reduces the expansion of the dielectric during connector assembly, and is particularly important when the probe is to be used over a wide range of temperatures. After heat treatment, one end of the cable is faced off flat and gold plated to prevent corrosion, the other end is attached to a standard male Type N

connector. Figure 5.1b shows a completed probe.

2. The Electromagnetic Fields of the Open-Ended Probe

This section reviews some of the attempts to determine the electromagnetic fields and the input admittance of the probe.

2.1. Modal Decomposition

A convenient and well known representation for the electromagnetic fields in a guiding structure splits the fields into three sets of transverse modes - Transverse Electric (TE), Transverse Magnetic (TM) and Transverse Electromagnetic (TEM) modes (Ramo et al. 1965; pp371-419). In metal guides, TE and TM modes are characterized by cut-off frequencies, which are determined by the guide geometry. Below the cut-off frequency for a particular mode, propagation along the guide ceases, and the mode becomes attenuated.

The TEM mode is the dominant mode in coaxial line, and the operating frequency and guide dimensions are usually chosen so that both TM and TE modes are far below cut-off. The electromagnetic field at the probe aperture is that of an ideal open-circuit TEM guide with other field components, which form the 'fringing' field, superimposed to satisfy the boundary conditions at the open end. Although the TE_{01} mode has the lowest cut-off frequency in coaxial line, because of the axial symmetry, only TM_{0N} modes are excited by the discontinuity. Thus the aperture field can be represented as the summation of the TEM mode, and a series of TM_{0N} modes. Mosig et al. (1981) used this modal representation to calculate the reflection coefficient of the TEM mode for a range of dielectric permittivities, the results were presented as a nomogram for each frequency.

Unfortunately this exact analysis is rather involved, and calculating the dielectric permittivity from measured data requires considerable computational effort since a closed form expression for the field is not available. Consequently, there

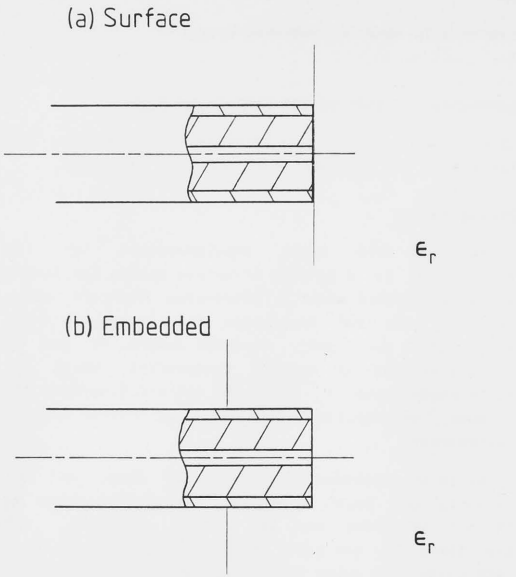

Figure 5.2 Diagrams (a) and (b) show two contact conditions between the RG401 probe and a dielectric material of relative permittivity ϵ_r.
The equivalent circuit of the probe is shown in (c).

has been much effort to develop an approximate equivalent circuit model for this sensor so as to provide a simpler, if less accurate, way to determine the permittivity from the probe input admittance.

2.2. Equivalent Circuit of the Open-Ended Probe

In RG401 semi-rigid coaxial cable (5.3mm diameter) the lowest TM mode, TM_{01}, has a cut-off frequency of about 54GHz. At the frequencies where the probe is used for dielectric measurement, e.g. below 10GHz, TM_{01} is attenuated by about 15dB/mm, indicating that the effect of the discontinuity only extends a few millimetres into the guide. Thus the probe can be modelled by lumped circuit elements located at the end of an ideal open-circuited line. Whinnery and Jamieson (1944) show that TM modes far below cut-off store energy in the electric field, so that a capacitor is the most appropriate element, one for each mode.

Tanabe and Joines (1976), measured the Q factor of a TEM resonator terminated by a probe. Their approximate analysis neglected radiation effects, and assumed the field at the probe tip and in the medium was purely TEM. Burdette et al. (1980) considered a more general probe geometry, in which the inner conductor of the coaxial cable was allowed to protrude from the end, forming a short monopole antenna. An antenna modelling theorem due to Deschamps (1962) was used to relate the impedance of the probe to the dielectric permittivity. Burdette's approach thus includes the open-ended probe as a special case, however a derivation specifically for the open-ended probe has been given by Brady et al. (1981) which is outlined below. Figure 5.2a shows the geometry.

In a non-magnetic medium where $\mu_r = 1$, the Deschamps antenna modelling theorem can be expressed as

$$Y(\omega, \varepsilon_r \varepsilon_o) = Y(\omega\sqrt{\varepsilon_r}, \varepsilon_o)\sqrt{\varepsilon_r} \qquad (5.01)$$

where Y is the antenna admittance, ε_r is the relative permittivity

(possibly complex) of the material in which the antenna is embedded, and ε_o and ω have their usual significance. The theorem applies to any probe geometry, provided the medium that surrounds the antenna is infinite in extent, in other words the radiation field must be wholly contained in the medium. Marcuvitz (1951) gives an analytic expression for the equivalent circuit admittance of a coaxial aperture radiating into free space which is of the form

$$Y(\omega) = a_4\omega^4 + ja_1\omega \qquad (5.02)$$

where a_1 and a_4 are functions of the geometry only. Applying (5.01) to (5.02) gives the following expression for the probe admittance

$$Y(\omega, \varepsilon_r) = G_o\varepsilon_r^{5/2} + j\omega C_o\varepsilon_r \qquad (5.03)$$

where G_o is the radiation conductance, and C_o is a capacitance that represents the fringing field. Note that G_o varies implicitly as ω^4. However, equation (5.03) is not strictly applicable to the open-ended probe geometry, for the following reasons:

(a) The field at the feed point of the probe, which is also the aperture in this case, is not purely TEM. Hence there is no unique antenna admittance and (5.01) does not apply (Deschamps 1962, Smith and Nordgard 1985).

(b) Marcuvitz's original derivation is only approximate since the aperture field is assumed to be TEM.

(c) Equation (5.02) is the low frequency approximation of a more complex expression. For the approximation to be valid, the probe dimensions should be much less than the wavelength in the dielectric.

(d) Equation (5.02) is derived for a coaxial aperture in an infinite ground plane whereas the open-ended probe possesses a very small ground plane (the thickness of the outer).

For the probes used in this work, and the dielectric materials we have measured, (c) is a reasonable assumption over most of the frequency range. Calculations performed by Bahl and Stuchly (1979) suggest that absence of the infinite ground plane has little effect, so that (d) is a reasonable approximation. Note that there are two probe contact geometries; the surface case, used for measurements of tissue, and the embedded case, used for measurements of liquids. The two geometries are shown in Figures 5.2a and 5.2b respectively. Brady et al. attempt to resolve the remaining difficulties by assuming the equivalent circuit capacitance can be decomposed into two separate terms. A capacitance, C_f, represents the fringing field in the PTFE dielectric of the cable, the other capacitance $\varepsilon_r C_o$, represents the fringing field in the external dielectric material, usually $C_o >> C_f$. Their final equivalent circuit model is shown in Figure 5.2c. The admittance of the probe, normalized to the TEM characteristic impedance Z_o ($=1/Y_o$), is

$$Y(\omega, \varepsilon_r)/Y_o = G_o Z_o \varepsilon_r^{5/2} + j\omega Z_o(\varepsilon_r C_o + C_f) \qquad (5.04)$$

which we refer to as probe admittance model I, or the 'non-linear' model. From the expressions for a_4 and a_1 derived by Marcuvitz, it can be shown that, for coaxial lines that are small compared with the wavelength and open into free space, $G_o << \omega C_o$. This suggests a further simplification, used by several workers (Athey et al. 1982, Stuchly et al. 1982a, Tran et al. 1984), which is to neglect G_o altogether. With this simplification, (5.04) becomes

$$Y(\omega, \varepsilon_r)/Y_o = j\omega Z_o(\varepsilon_r C_o + C_f) \qquad (5.05)$$

which we refer to as probe admittance model II or the 'linear' model. In a later paper, Stuchly et al. (1982b) examine this simplification more carefully, and suggest that it can lead to considerable errors at high frequencies for large permittivities.

Gajda and Stuchly (1983) have investigated the accuracy of the simpler circuit model of equation (5.05) using numerical methods. The analysis was restricted to the static case, thus

only lossless dielectrics were modelled, and radiation effects were ignored. They used both the Finite Element Method and the Method of Moments to calculate the equivalent circuit capacitance, and compared their numerical results with measured capacitances. They concluded that although C_f and C_o are functions of ε_r, the model is a good approximation for large permittivities, since C_f and C_o are relatively constant in this range. For small permittivities (they suggest $\varepsilon_r' < 10$) the model is less accurate.

Newnham (1985), as part of a third year undergraduate project in this department, investigated some of these problems experimentally, and attempted to measure and calculate the errors involved in using the simple model of the probe.

2.3. Field Penetration

All the analyses above start by assuming that the dielectric material is semi-infinite in extent. In practice, the probe must be presented with a sample of finite thickness, so it is important to establish how far the field penetrates. Although this can be done experimentally for measurements on dielectric liquids, it is much more difficult for biological materials which are often inhomogeneous.

Anderson (1984) computed the field distribution, and hence the capacitance of the open-ended line immersed in water. Water layers of varying thickness backed by air or a metal wall were assumed, and a quasi-static solution was obtained using the Method of Moments. Theoretical predictions were confirmed by experimental measurements of the probe capacitance over 200MHz to 2GHz. For a 6.4mm diameter (RG401) probe immersed in water, the error in the sensor capacitance as compared with the homogeneous case was found to be < 1% for layers thicker than 6mm. Thus, the effective volume of material interrogated by the probe can be quite small.

According to Stuchly (1984), the electric field is most intense around the inner conductor of the probe. However the exact field distribution (and hence the equivalent circuit

parameters) depends on the surface conditions of the probe. Burdette (1984) was particularly careful to ensure that the probe surface was cleaned between each measurement. Also, when measuring biological tissue, he was careful to ensure constant contact pressure between the probe tip and the surface of the material.

The open-ended probe geometry is closely related to that of the annular slot antenna, which was first studied by Levine and Papas (1951). In order to investigate its efficacy as an applicator for localized hyperthermia treatment of tumours, Nevels et al. (1985) have calculated the fields of this applicator and its apparent input admittance in biological media. They used essentially the same method as Mosig et al. (1981), and their calculations confirm the simple picture of the probe input admittance as a capacitance at low frequency, and show that the field is very intense around the probe tip.

3. Microwave Measurement of One-Port Networks

In order to measure the permittivity of an unknown dielectric material, the input admittance of the probe must be measured, whatever the circuit model. At the frequencies of interest, direct admittance measurements are very difficult; instead measurements of the probe input reflection coefficient are made. The reflection coefficient Γ of an admittance Y is defined with respect to a wave admittance Y_o as

$$\Gamma = \frac{Y_o - Y}{Y_o + Y} \qquad (5.06)$$

The reflection coefficient can be measured in either the time domain or the frequency domain; we concentrate here on the frequency domain technique that has been used for the majority of our measurements. Chapter 6 contains a brief description of the time domain version.

Reflection coefficients can be measured in both magnitude and phase over a range of frequencies using a Network Analyzer (Adam

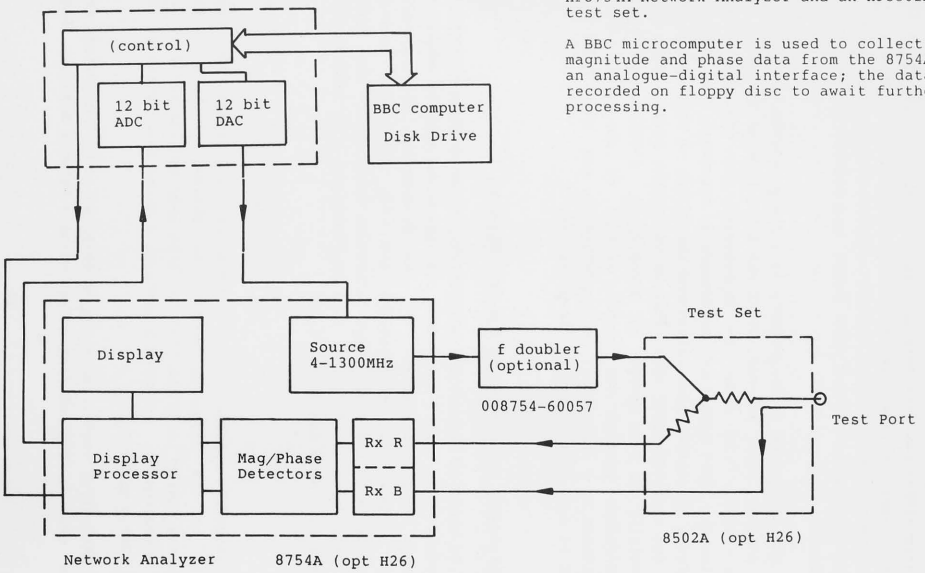

Figure 5.3 Block diagram of the Semi-Automated Network Analyzer system. The system is based on an HP8754A Network Analyzer and an HP8502A test set.

A BBC microcomputer is used to collect magnitude and phase data from the 8754A via an analogue-digital interface; the data are recorded on floppy disc to await further processing.

1978). Such systems have been used by many workers for dielectric measurement applications (Burdette *et al.* 1980, Stuchly and Stuchly 1984). Most practical Network Analyzer systems can measure the scattering parameters of microwave two-port networks. However the discussion here is restricted to the measurement of one-port networks such as the open-ended probe.

3.1. A Practical Network Analyzer System

The Network Analyzer system we have used for our investigation consists of a Hewlett-Packard 8754A Option H26 Network Analyzer, an 8502A Transmission/Reflection test set and an 08754-60057 frequency doubler. A microcomputer controlled interface of our own design records measurements for subsequent processing. Figure 5.3 shows a block diagram of the system. A description of the function and implementation of the interface and the relevant details of the 8754A operation are contained in chapter 6 and appendix 3. The next chapter contains further practical details of the system. This configuration is capable of measuring the reflection coefficient of the probe in magnitude and phase over a 4-2600MHz frequency range.

3.2. Error Models for One-Port Measurements

In any real Network Analyzer system, there are a number of imperfections, both in the connections between the one-port and the Network Analyzer, and in the Network Analyzer itself. It is convenient to model this imperfect Network Analyzer measuring a one-port, as a perfect Network Analyzer connected to the one-port via a general two-port network that embodies the system errors. This error network can be represented by a frequency dependent scattering matrix $\underline{N}$. Note that this is implicitly a linear model of the system errors.

Some physical interpretation can be placed on the elements of $\underline{N}$. N_{11} is the directivity error and it includes the effect of the finite directivity of the coupler used to separate the incident and reflected signals in the test set. N_{22} is the source match error, and is caused by multiple reflections of the reflected

signal back to the unknown. $N_{12}N_{21}$, the frequency tracking error, is caused by the (usually) small variations in gain and phase flatness between the test and reference channels. Note that it is impossible in general (and unnecessary in this application) to obtain N_{12} or N_{21} separately from reflection measurements alone (Bauer and Penfield 1974). Only their product may be obtained uniquely, though if the error network is known to be reciprocal, N_{12} and N_{21} are equal, although there is a sign ambiguity.

If the admittance is to be measured accurately, the effects of of the intervening two-port error network must be removed. The true reflection coefficient Γ_m can be calculated from the measured value ρ_m at each frequency using

$$\Gamma_m = \frac{\rho_m - N_{11}}{\rho_m N_{22} - (N_{11}N_{22} - N_{12}N_{21})} \tag{5.07}$$

which can be quickly derived from a signal flow graph using standard methods (Adam 1969; pp86-106). The elements of $\underline{N}$ are determined by performing separate measurements on known terminations at each frequency of interest, most commonly a short circuit, an open circuit and a matched load. With this set of known terminations, the elements of $\underline{N}$ are given by

$$N_{11} = \rho_{ma} \tag{5.08a}$$

$$N_{22} = 1 - 2\,\frac{\rho_{ma} - \rho_{sc}}{\rho_{oc} - \rho_{sc}} \tag{5.08b}$$

$$N_{12}N_{21} = (1 - N_{22})\,(\rho_{oc} - \rho_{ma}) \tag{5.08c}$$

where ρ_{sc}, ρ_{oc} and ρ_{ma} are the complex reflection coefficient measurements of a short circuit, open circuit and matched load respectively. The expressions above are usually the minimum needed because of the inadequacies of practical microwave terminations (particularly matched loads). This type of error correction procedure has been used by many workers, including Burdette et al. (1980a), Brady et al. (1981), Athey et al. (1982) and Stuchly et al. (1982a). Bauer and Penfield (1974) show that

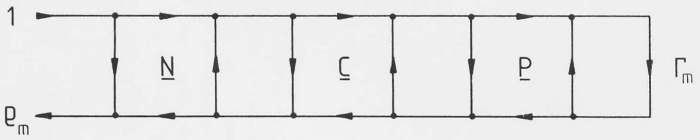

Figure 5.4 Signal flow graphs for the open-ended probe dielectric measurement system.

The top graph shows three cascaded two-ports which represent the Network Analyzer and associated test set (N), the probe connector (C), and the probe cable (P). The reflection coefficient of the open end is Γ_m, the corresponding measurement of it is ρ_m.

In fact all three two-ports may be cascaded into one error network (E) as shown in the lower graph.

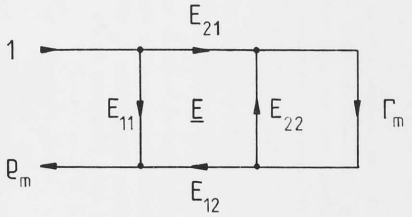

the effect of noise in the measurement system can be reduced by using the redundant information available from measurements of more than three known terminations, although this is not always practical, and is more complex computationally.

Bauer and Penfield (1974) divide the error correction method into two distinct stages, known as unterminating and de-embedding.

Unterminating

Characterize the system errors by a scattering matrix $\underline{N}$, say, and make measurements of known one-ports to determine the elements of $\underline{N}$ e.g. equation (5.08a-c).

De-embedding

Correct measurements of unknown one-ports, using $\underline{N}$ to evaluate the error corrected reflection coefficient, e.g. equation (5.07).

3.3. Application to the Open-Ended Probe

In this measurement application the probe is connected to the Network Analyzer via a pair of imperfect connectors and imperfect cabling, so additional scattering matrices $\underline{C}$ for connectors, and $\underline{P}$ for the probe cable are needed. Figure 5.4 shows the full signal flow graph for the composite system, measuring an unknown admittance Y_m which has a true reflection coefficient Γ_m.

Since we are not particularly interested in the scattering parameters of, say, the connectors, we combine all the error networks into one with scattering matrix $\underline{E}$. The de-embedding for this composite system is performed using (5.07) with N_{ij} replaced by E_{ij}

$$\Gamma_m = \frac{\rho_m - E_{11}}{\rho_m E_{22} - (E_{11}E_{22} - E_{12}E_{21})} \qquad (5.09)$$

Again, the elements of the composite error matrix $\underline{E}$ are determined from measurements of known terminations, at each of the

frequencies of interest, but this time the terminations must be applied at the probe tip. The short circuit condition can be readily provided by pressing metal foil, backed with plastic foam, against the probe tip. The open-circuit condition can be realized, approximately, by leaving the probe open into air, however, the provision of a matched load is much more difficult. Such a component would be expensive to manufacture, and extremely difficult to design so that it was both repeatable and had an accurately known reflection coefficient.

Kraszewski et al. (1983b), recognizing these difficulties, introduced the idea of using dielectric materials, usually polar liquids, of known dielectric properties as terminations for the probe. They developed a set of expressions for the elements of $\underline{E}$ in terms of a set of general terminations, which is given below.

Consider three reflection coefficient measurements ρ_1, ρ_2, and ρ_3 of three different but otherwise arbitrary terminations, which have known reflection coefficients Γ_1, Γ_2 and Γ_3 respectively. Then the elements of $\underline{E}$ are given uniquely by

$$E_{11} = \frac{\Gamma_1\Gamma_2\rho_3(\rho_1 - \rho_2) + \Gamma_1\Gamma_3\rho_2(\rho_3 - \rho_1) + \Gamma_2\Gamma_3\rho_1(\rho_2 - \rho_3)}{\Gamma_1\Gamma_2(\rho_1 - \rho_2) + \Gamma_1\Gamma_3(\rho_3 - \rho_1) + \Gamma_2\Gamma_3(\rho_2 - \rho_1)} \tag{5.10a}$$

$$E_{22} = \frac{\Gamma_1(\rho_2 - E_{11}) + \Gamma_2(E_{11} - \rho_1)}{\Gamma_1\Gamma_2(\rho_2 - \rho_1)} \tag{5.10b}$$

$$E_{12}E_{21} = \frac{(\rho_1 - E_{11})(1 - E_{22}\Gamma_1)}{\Gamma_1} \tag{5.10c}$$

These expressions are essentially an extended form of (5.08a-c), and can be derived from (5.09). Although specifically developed for the error correction of reflection coefficients measurements made with the probe, they apply to any one-port measurement problem. Kraszewski et al. suggest that three suitable known terminations are a short circuit, the open circuit probe (modified by the fringing capacitance $C_f + C_o$), and the probe in contact with some known dielectric liquid.

The problem that remains is that the predicted reflection coefficients Γ_1, Γ_2 or Γ_3 cannot be evaluated unless the equivalent circuit parameters G_o, C_o and C_f are already known. The circuit parameters can be estimated from the geometry (i.e. the fields), but as noted in section 2.3, the fields at the probe tip are even dependent on the surface finish, so an experimental technique is preferable here. Kraszewski *et al.* suggest that the probe equivalent circuit should be determined using measurements on other known liquids i.e. those not used in the error correction. Their proposed iterative procedure uses estimates of the circuit parameters to perform error correction on the reflection measurements from the other known liquids and from the resulting admittances, obtain better estimates of the circuit parameters.

The next section describe the direct de-embedding procedure we have developed that circumvents these problems.

4. Direct Error Correction For One-Port Measurements

The error correction method described in the previous section splits the problem into two stages; (i) unterminate E, and (ii) use E to de-embed subsequent measurements. In this application, the unterminating step is auxiliary in that E is only needed for de-embedding measurements. This section describes a simple technique that allows the unterminating step to be avoided altogether, and allows direct de-embedding to be performed.

4.1. Derivation of the Direct De-embedding Procedure

This section derives the procedure in its most general form; the next section examines its application to the special case of the open-ended probe.

As before, we start with a set of reflection coefficient measurements ρ_1, ρ_2, ρ_3 on known admittances y_1, y_2, y_3 and measurement ρ_m on an unknown admittance y_m. The y_i's are normalized so that the known reflection coefficients are

$$\Gamma_i = \frac{1 - y_i}{1 + y_i} \tag{5.11}$$

for i = 1,2,3,m. Substituting (5.11) into (5.10a-c), and the resulting expressions into (5.09) yields

$$y_m = - \frac{r_{m1}r_{32}\, y_3\, y_2 + r_{m2}r_{13}\, y_1\, y_3 + r_{m3}r_{21}\, y_2\, y_1}{r_{m1}r_{32}\, y_1 + r_{m2}r_{13}\, y_2 + r_{m3}r_{21}\, y_3} \tag{5.12}$$

where

$$r_{ij} = \rho_i - \rho_j \tag{5.13}$$

This remarkably simple and symmetrical expression is formally equivalent to the previous error correction procedure, except that the elements of $\underline{E}$ are not calculated. Although the derivation is easy to describe, it is difficult to perform; the algebra involved in the substitutions, expansions and the subsequent cancellation is quite lengthy. The actual manipulation was performed on a mainframe computer using a symbolic algebra package called REDUCE (Hearn 1974).

There are two important linearity properties of the error correction procedure that can be derived from the reduced form of equation (5.12).

Property 1

If a new set of reflection coefficients ρ_i' are computed such that

$$\rho_i' = e_1\rho_i + e_2 \tag{5.14}$$

for i = 1,2,3,m where e_1 and e_2 are arbitrary complex constants, then y_m is unchanged.

Property 2

If a new set of admittances y_i' are computed such that

$$y_i = e_3 y_i' + e_4 \tag{5.15}$$

for i = 1,2,3,m where e_3 and e_4 are arbitrary complex constants, then (5.12) also holds for the y_i'.

Property 1 means that, practically speaking, absolute values of the phase or magnitudes of the reflection coefficient are not required - we need only be concerned about drift and repeatability in the measurement system. Property 2 is particularly important in the application of this error correction procedure to dielectric measurements, which is the subject of the next section. Property 1 can be derived from inspection of (5.12) and (5.13a-c), however REDUCE was used to derive property 2.

There is a further simplification that arises if a short circuit termination is used for one of the known admittances. From a practical point of view, short circuit terminations are quite easy to manufacture for many microwave measurement situations, so this is an important case to consider. Identify known termination 1 with a short circuit, then as $y_1 \rightarrow \infty$, (5.12) becomes

$$y_m = - \frac{r_{m3} r_{21} y_2 + r_{m2} r_{13} y_3}{r_{m1} r_{32}} \tag{5.16}$$

Note that property 1 and property 2 can both be obtained with little effort from this equation.

5. Application to Dielectric Measurements

This section concentrates on the application of the general direct de-embedding technique developed in the previous section to dielectric measurements with the open-ended probe. The first problem that must be addressed is which equivalent circuit model

for the probe admittance should be used.

5.1. Probe Admittance Model I

Section 2 showed that both of the equivalent circuit models for the probe admittance are somewhat approximate, but equation (5.04), reproduced below, is thought to be more accurate (Stuchly et al. 1982b).

$$Y(\varepsilon_r)/Y_o = G_o Z_o \varepsilon_r^{5/2} + j\omega Z_o(\varepsilon_r C_o + C_f)$$

Substituting this admittance model into (5.12), with three known permittivities ε_1, ε_2 and ε_3, and an unknown permittivity ε_m, generates a fifth order polynomial in $\varepsilon_m^{1/2}$:

$$G_o\varepsilon_m^{5/2} + j\omega(\varepsilon_m C_o + C_f)$$

$$+ \frac{r_{m1}r_{32}Y(\varepsilon_3)Y(\varepsilon_2) + r_{m2}r_{13}Y(\varepsilon_1)Y(\varepsilon_3) + r_{m3}r_{21}Y(\varepsilon_2)Y(\varepsilon_1)}{r_{m1}r_{32}Y(\varepsilon_1) + r_{m2}r_{13}Y(\varepsilon_2) + r_{m3}r_{21}Y(\varepsilon_3)}$$

$$= 0 \qquad (5.17)$$

with r_{ij} defined as in (5.13). The coefficients of this polynomial are functions of the known permittivities, the reflection coefficient measurements and the circuit parameters G_o, C_o and C_f. Now apply a linear transformation to $Y(\varepsilon_r)$ to give $y(\varepsilon_r)$ such that

$$Y(\varepsilon_r) = j\omega C_o y(\varepsilon_r) + j\omega C_f \qquad (5.18)$$

Property 2 states that, under a such a linear transformation, $y(\varepsilon_r)$ also satisfies (5.12). Further, this linear transformation yields

$$y(\varepsilon_r) = \varepsilon_r + \frac{G_o}{j\omega C_o}\varepsilon_r^{5/2} \qquad (5.19)$$

so that (5.17) becomes

$$G_n \varepsilon_m^{5/2} + \varepsilon_m + \frac{r_{m1} r_{32} y(\varepsilon_3) y(\varepsilon_2) + r_{m2} r_{13} y(\varepsilon_1) y(\varepsilon_3) + r_{m3} r_{21} y(\varepsilon_2) y(\varepsilon_1)}{r_{m1} r_{32} y(\varepsilon_1) + r_{m2} r_{13} y(\varepsilon_2) + r_{m3} r_{21} y(\varepsilon_3)} = 0 \qquad (5.20)$$

where $G_n = G_o / j\omega C_o$, the normalized radiation conductance. The reduction of (5.17) to (5.20) shows that the absolute values of G_o, C_o and C_f need not, indeed cannot, be determined using this error correction procedure. However, G_n must be determined in order to calculate ε_m from the measured reflection coefficient ρ_m. This may be accomplished by measuring the probe reflection coefficient, ρ_4, for another known dielectric with permittivity ε_4, then setting $m = 4$ into (5.20), and solving the resulting quadratic in G_n. Once G_n is known, the permittivity of subsequent measured dielectrics can be obtained from (5.20), which can be solved numerically for ε_m.

5.1.1. Short Circuit Simplification

There are a number of advantages in using a short circuit as one of the known terminations. From a practical point of view, a short is easy to make for this geometry, and from a theoretical point of view, equation (5.20) becomes much simpler. Because of these factors, we have used the short circuit termination as a reference for our experimental measurements, using the following reduced form of (5.20). With known termination 1 identified as a short circuit, then as $y_1 \to \infty$ (5.20) becomes

$$G_n \varepsilon_m^{5/2} + \varepsilon_m + h = 0 \qquad (5.21)$$

where

$$h = \frac{r_{m2} r_{13}\, y(\varepsilon_3) + r_{m3} r_{21}\, y(\varepsilon_2)}{r_{m1} r_{32}} \qquad (5.22)$$

A further advantage of the short circuit termination is that the expression for G_n is much simpler in form. Given a fourth measurement ρ_4 of a known material with permittivity ε_4, G_n can be calculated directly by setting m = 4 in (5.21) yielding

$$G_n = - \frac{r_{41}r_{32}\varepsilon_4 + r_{42}r_{13}\varepsilon_3 + r_{43}r_{21}\varepsilon_2}{r_{41}r_{32}\varepsilon_4^{5/2} + r_{42}r_{13}\varepsilon_3^{5/2} + r_{43}r_{21}\varepsilon_2^{5/2}} \qquad (5.23)$$

5.2. Probe Admittance Model II

The previous development has shown that the permittivity can be calculated from the measured reflection coefficients knowing only the dimensionless parameter $G_n = G_o/j\omega C_o$. In section 2 it was shown that $G_o << \omega C_o$ for the probe at low frequencies, so that as a further approximation, set $G_o = 0$, as in equation (5.05) so that the admittance is linearly related to ε_r. With this approximation, which has been used by Athey et al. (1982), Stuchly et al. (1982a) and Tran et al. (1984), equation (5.20) becomes

$$\varepsilon_m = - \frac{r_{m1}r_{32}\varepsilon_3\varepsilon_2 + r_{m2}r_{13}\varepsilon_1\varepsilon_3 + r_{m3}r_{21}\varepsilon_2\varepsilon_1}{r_{m1}r_{32}\varepsilon_1 + r_{m2}r_{13}\varepsilon_2 + r_{m3}r_{21}\varepsilon_3} \qquad (5.24)$$

with the r_{ij} as defined in (5.13).

Using (5.24) the permittivity ε_m can be calculated directly from reflection coefficient measurements, without any knowledge of the equivalent circuit components C_o and C_f. Although the equation is simple in form, it still embodies the error correction procedure for an arbitrary two-port error network. If greater accuracy is required, then this simple form can be used as a starting point for the solution of (5.20). Since $G_o/\omega C_o$ is small, the resulting ε_m from (5.24) is usually quite close to the required root of (5.20).

5.2.1. Short Circuit Simplification

The short circuit form of (5.24) is

$$\varepsilon_m = - \frac{r_{m2}r_{13}\ \varepsilon_3 + r_{m3}r_{21}\ \varepsilon_2}{r_{m1}r_{32}} \qquad (5.25)$$

Figure 5.5 Reflection coefficient measurements made over 8-2600MHz using the HP8754A Network Analyzer, HP8502A test set and open-ended probe.

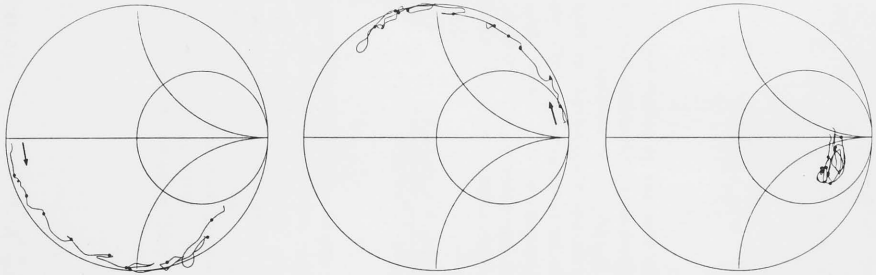

(a) Short Circuit (b) Air (c) 100mM Saline

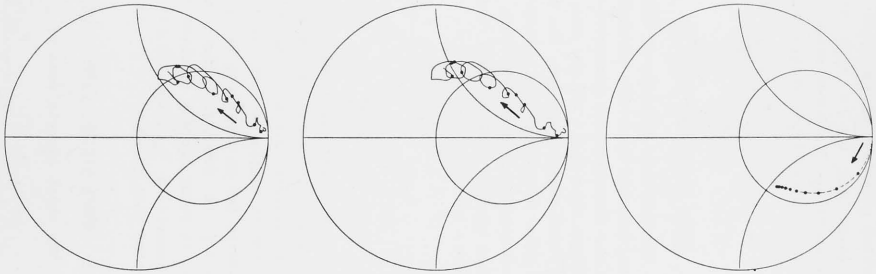

(d) Methanol (e) Ethanediol (measured) (f) Ethanediol (theory)

Note that using this equation, it is unnecessary to know any of the equivalent circuit parameters for the probe. It is (5.25) that best illustrates the remarkable simplicity that the direct de-embedding procedure offers to dielectric measurements using the open-ended probe. For efficient computation, this expression can be rearranged as a bilinear transform of ρ_m - see chapter 6.

6. A Direct De-Embedding Example

This section contains an example of the direct de-embedding procedure described in this chapter. Measurements of reflection coefficient from an open-ended probe dipped in ethanediol which were made using the HP8754A Network Analyzer system are processed to give the corresponding permittivity. Further details of the measuring system are given in the next chapter.

6.1. Reflection coefficient measurements

Figure 5.5a-d show, on separate polar plots, reflection coefficient measurements over 8-2600MHz for a short circuit and three reference materials with known dielectric properties - air, 100mM saline (Stogryn 1971) and methanol (Jordan et al. 1978). Figure 5.5e shows the reflection coefficient for ethanediol, whose permittivity is to be measured.

In fact, the dielectric permittivity of ethanediol is also known (Jordan et al. 1978), so the measurement is compared with the known result. The predicted reflection coefficient for the probe in contact with ethanediol is shown in Figure 5.5f. This was calculated using C_o = 0.041pF (Athey et al. 1982), C_f = 0.002pF and G = 4.7nS (estimated). It should be emphasised that this is the only place where the values of the equivalent circuit components have been used.

The measured S parameters are very different to the predicted ones. Part of this difference is due to the (deliberate) shift in the phase zero reference plane which has been introduced by the cabling. The numerous folds and wiggles in the measured data are

Figure 5.6 Dielectric measurements of the permittivity of ethanediol. The solid curves are from the measured data of Figure 5.5 de-embedded using the non-linear admittance model of equation (5.04). The dashed line is taken from the measurements of Jordan et al. (1978).

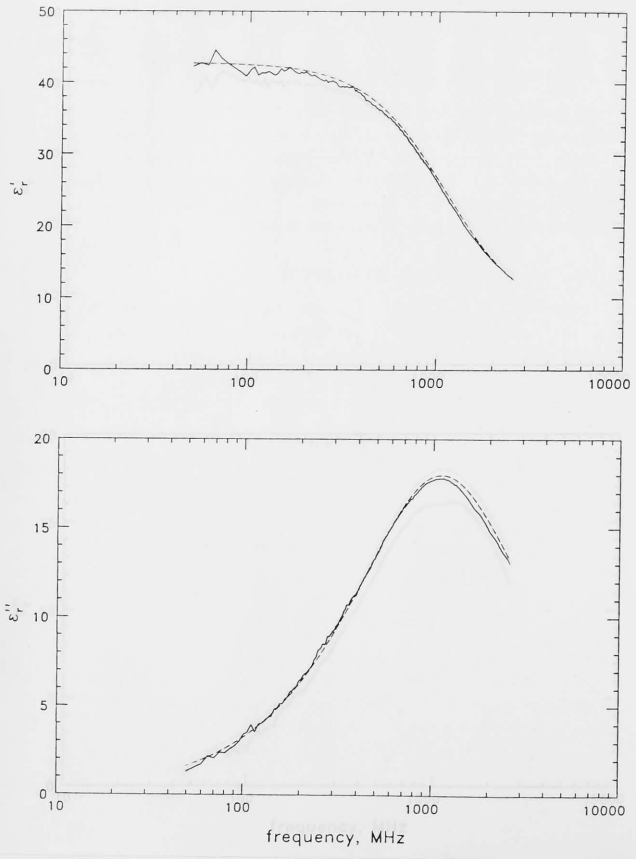

fully repeatable; they arise from the imperfections in the Network Analyzer itself, the test set, its cabling and its connectors. It is these imperfections (as well as the phase offset) that the de-embedding procedure corrects. Note that the corrected S parameters themselves cannot be calculated without knowing values for the equivalent circuit parameters of the probe.

6.2. De-embedded Results

Admittance Model I

Figure 5.6 shows the permittivity results obtained using the non-linear admittance model. There is excellent agreement between the de-embedded measurements of Figure 5.5e (solid line) and the dielectric measurements of Jordan et al. (1978) (dashed line).

Admittance Model II

Figure 5.7 shows the permittivity results obtained using the linear admittance model. In this case, the agreement is not so good.

6.3. Choice of Admittance Model

Clearly, the non-linear admittance model gives greater accuracy for this material. In general, for the measurements of other known liquids, the real part of the measured complex permittivity seems to be more accurate than the imaginary part, and the measured value of the imaginary part is lower than the true value. The cause of this discrepancy is not clear, and further experimental work is required. The error generally seems to increase at low frequencies, whereas the errors introduced by setting G_n to zero would be expected to increase as ω^3 (Newnham 1985). For lossy (conductive) materials, the difference seems much less pronounced. In chapter 7 the measurements on one of the cryoprotectants studied are shown after processing with both admittance models; the difference in the permittivity and effective conductivity is barely detectable.

Figure 5.7 Dielectric measurements of the permittivity of ethanediol. The solid curves are from the measured data of Figure 5.5 de-embedded using the linear admittance model of equation (5.05). The dashed line is taken from the measurements of Jordan et al. (1978).

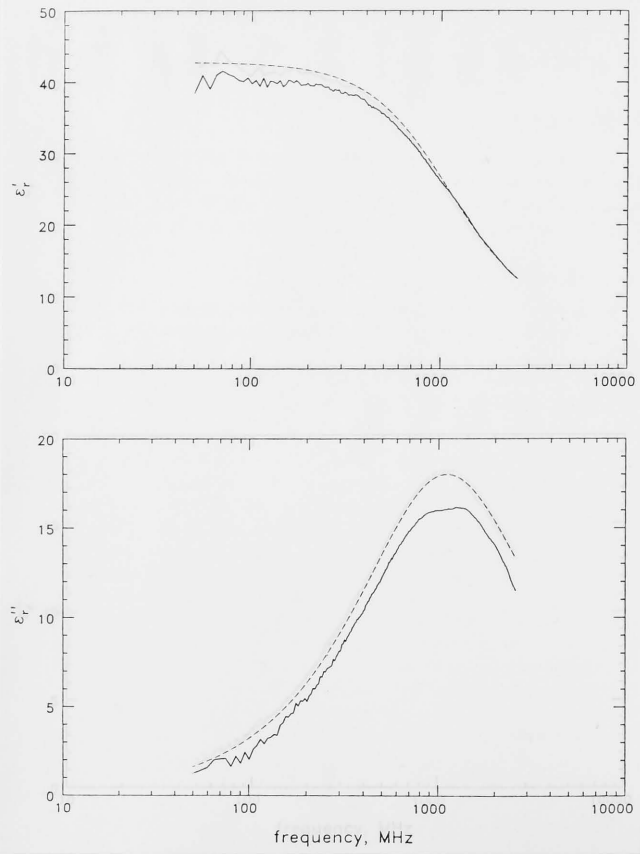

7. Uncertainty Analysis for the Open-Ended Probe

This section investigates how the instrumentation uncertainties propagate into the permittivity measurements. The direct de-embedding procedure allows the uncertainties in the Network Analyzer measurements to be related directly to the resulting uncertainty in the measured permittivity.

It has been shown that the greatest accuracy in determining the permittivity for a given accuracy of reflection coefficient measurement is obtained when

$$\omega C_o Z_o |\varepsilon_m| = 1 \qquad (5.26)$$

the 'optimum capacitance' condition (Athey et al. 1982). Taking C_o = 0.041pF as before, and the permittivity as that of 150mM saline (Stogryn 1971), this condition is realized at about 900MHz which lies nicely in the middle of the range which we wish to measure.

Kraszewski et al. (1983a) examined the error sensitivity of the simple probe admittance model (5.05), and calculated the uncertainty in the measured permittivity resulting from using the linear admittance model. Their calculations were performed for a 3.6mm diameter probe, measured at 3GHz, assuming measurement system uncertainties of 0.05dB in magnitude and 0.3° in phase. They concluded that, for tissue permittivity measurements the relative uncertainties are less than 1% in ε_r' and less than 3% in ε_r''.

The remainder of this section describes the method we have used to estimate the uncertainties in our own measurements. This technique allows the uncertainty to be estimated for any set of measurements, over the full range of frequencies. Use of the direct de-embedding procedure means that fixed magnitude and phase offsets are removed (linearity property 1). Instrumentation uncertainties which are significant are those due to drift and noise in the measurement system. Four assumptions about the system are made at the outset:

a) The non-linear admittance model of equation (5.04) for the probe is correct.

b) The errors in the Network Analyzer can be adequately represented by a scattering matrix.

c) The uncertainties in the magnitude and phase of the reflection coefficients are much smaller than the magnitude of the reflection coefficients.

d) The uncertainties in the permittivity of the known dielectric materials are small compared with the other system errors.

Under these assumptions, when the measured permittivity is calculated using (5.21-23), the permittivity is a function of the reflection coefficient measurements alone. Measurements ρ_1, ρ_2, ρ_3 are used for de-embedding, ρ_4 is used for G_n, and ρ_m is the reflection coefficient corresponding to ε_m, thus the uncertainty $\delta\varepsilon_m$ in ε_m is given by -

$$\delta\varepsilon_m = \sum_i \frac{\partial\varepsilon_m}{\partial\rho_i}\,\delta\rho_i \qquad (5.27)$$

where the $\delta\rho_i$ are the uncertainties in the reflection coefficient measurements, and the summation is taken over i = 1,2,3,4,m. The individual partial derivatives are obtained by straightforward differentiation, however their algebraic form is not particularly illuminating. Instead, the worst case error in the measured permittivity resulting from given uncertainty estimates in the magnitude and phase of ρ_i are calculated by substituting the measured values of the reflection coefficients into these partial derivatives. The technique is described in more detail below.

7.1. Calculation of the Worst Case Error

The ith term of (5.27) is the error sensitivity for ρ_i, which effectively relates the uncertainty in the measurement of ρ_i to the resulting permittivity. Assume that the ith set of measurements are wrong in magnitude and phase by the absolute quantities δm_i and δp_i respectively. Further, all these errors are

Figure 5.8 The uncertainty $\delta\rho_i$ produced in the ρ-plane by measurement uncertainties δm_i in magnitude and δp_i in phase.

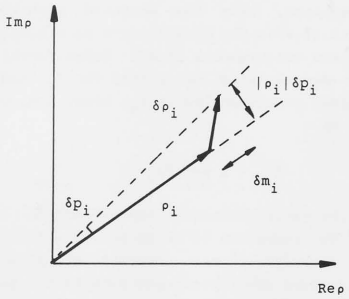

$$\delta\rho_i \simeq (\delta m_i + j|\rho_i|\delta p_i) \exp(j \arg\rho_i)$$

bound such that

$$|\delta m_i| \leq \delta M \quad \text{and} \quad |\delta p_i| \leq \delta P \tag{5.28}$$

where δM and δP are small compared with $|\rho_i|$. From Figure 5.8,

$$\delta\rho_i = (\delta m_i + j|\rho_i|\delta p_i) \exp(j \arg\rho_i) \tag{5.29}$$

For brevity, write

$$K_i = \frac{\partial \varepsilon_m}{\partial \rho_i} \exp(j \arg\rho_i) \tag{5.30}$$

with $K_i' = \mathrm{Re}(K_i)$ and $K_i'' = \mathrm{Im}(K_i)$. Now maximize the error in the real and imaginary parts of $\delta\varepsilon_m$ separately (hence 'worst case', above)

$$\delta\varepsilon_m' = \delta M \sum_i |K_i'| + \delta P \sum_i |K_i''\rho_i| \tag{5.31a}$$

$$\delta\varepsilon_m'' = \delta M \sum_i |K_i''| + \delta P \sum_i |K_i'\rho_i| \tag{5.31b}$$

where $\delta\varepsilon_m'$ and $\delta\varepsilon_m''$ are the uncertainties in the real and imaginary parts respectively. These equations allow the calculation of the error bounds for measured data, given only estimates of δM and δP.

7.2. Uncertainty Analysis Example

This technique is used on the data of Figure 5.5 to provide uncertainty estimates for the measured permittivity of ethanediol in the following chapter.

Chapter 6

Dielectric Measurements with an Open-Ended Coaxial Probe:

Part II - Practical Details

The previous chapter showed how measurements of the input impedance of an open-ended semi-rigid coaxial probe can be related to the permittivity of the material it is in contact with. This chapter concerns the implementation of a dielectric measurement system using such probes, and describes the procedures used to make measurements over a range of temperatures on cryoprotectants and perfused tissue.

For the majority of the work using the open-ended probe, we have used frequency domain instrumentation to measure the probe impedance, that is a Hewlett-Packard 8754A Network Analyzer and much of the chapter concerns this system. Similar instrumentation using the HP8410B Network analyzer has been used by Burdette et al. (1980) and the Stuchly's (Athey et al. 1982).

Section 1 describes the important features of the Network Analyzer, and of the digital recorder that has been used to record the measurements for subsequent processing. The remaining experimental apparatus used for measurements on liquids and perfused tissue is described in section 2. Section 3 describes the experimental procedures and associated software used to perform calibration, error correction, and calculation of the measured permittivity.

The resolution and accuracy of the composite system is described in section 4, and the uncertainties for the measurement of a 'standard liquid' are evaluated.

The probe impedance can also be measured successfully in the time domain, section 5 describes the experimental layout used to make such measurements using the instrumentation described in chapter 4. This is believed to be one of the first demonstrations

Figure 6.1 Network Analyzer Block Diagram.
The 8754A is shown configured as a reflectometer.

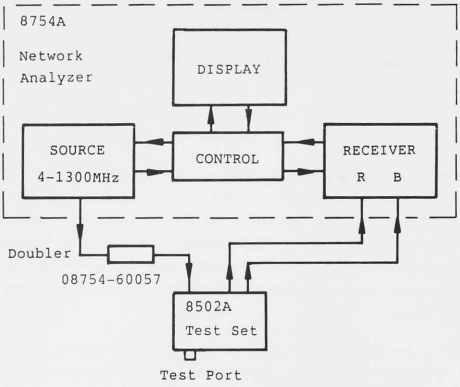

Figure 6.2 Transmission/Reflection Test Set Schematic.

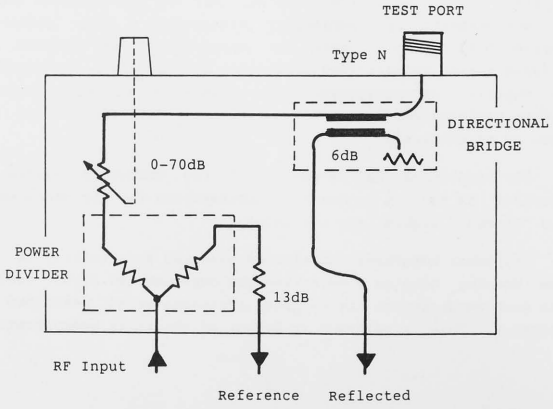

of such measurements using time domain instrumentation.

1. Frequency Domain Instrumentation

1.1. The Hewlett-Packard 8754A Network Analyzer

At microwave frequencies, direct impedance measurements cannot be made, and concepts such as voltage and current become less useful; instead a wave approach becomes more appropriate. The open-ended probe is a one-port network, and the impedance can be deduced from measurement of the reflection coefficient. The HP8754A is a frequency domain Network Analyzer, which together with a suitable test set and frequency doubler, performs such measurements directly over a frequency range of 4-2600MHz‡. Much of the information concerning the operation of the 8754A in the description below has been gleaned from the manufacturers handbook, and Application Note 294 (Hewlett-Packard 1979).

The 8754A consists of a swept RF source and dual receiver system, together with some sophisticated display electronics. The dual receiver system can measure the magnitude ratio of, and relative phase between two signals derived from the RF source. When used with an HP8502A transmission/reflection test set, the resulting configuration can measure the reflection coefficient, i.e. S_{11}, in both magnitude and phase. In fact, the 8754A can be used to measure all the four S parameters of a two port network, however, the functional description below is restricted to that required for one-port measurements, which is the configuration shown in the block diagram in Figure 6.1.

1.1.1. The 8502A Transmission/Reflection Test Set

The 8502A test set contains the microwave components necessary to configure the source and receiver of the 8754A as a reflectometer. The most important components of the test set are

‡ 'Opt H26' is required for extended frequency operation.

the power divider and the directional bridge, which are shown in Figure 6.2. The power divider returns, via a compensating attenuator, a fraction (-19dB) of the source power to the 'R' or 'reference' channel of the 8754A receiver; the other half is sent via a 0-70dB step attenuator to the directional bridge. The one-port to be measured is connected to the test port of the 8502A; the reflected power is coupled (-6dB) by the directional bridge into the 'B' or 'test' channel of the 8754A receiver. The bridge directivity is quoted as better than 40dB.

1.1.2. RF Source

The source in the 8754A sweeps from 4 to 1300MHz, or part of that range, and consists of a pair of varactor tuned oscillators operating in a 'see-saw' configuration. One oscillator is swept down from 3.6 to 3.0GHz whilst the other is swept up from 3.6 to 4.3GHz; the two outputs are mixed, and the difference frequency amplified and levelled to give a continuously variable output up to +10dBm. When used with an 08754-60057 frequency doubler, the output frequency range is extended to 2600MHz. Builtin crystal markers are available at 1, 10 and 50MHz intervals, accurate to ±0.01%.

In normal (LOCAL) operation, an internal slow ramp generator sweeps both the source and receiver tuning. By switching to REMOTE operation, the source frequency can be programmed externally by a dc voltage fed into the rear panel EXT SWEEP INPUT jack. This enables the source frequency to be externally programmed anywhere between the minimum and maximum values set up on the front panel sweep controls.

1.1.3. Receiver

In this application, the 8754A receiver is used to measure the magnitude and phase of the complex ratio B/R, i.e. the reflected signal divided by the reference signal. The receiver down-converts the two RF signals from the test set to a 1MHz intermediate frequency (IF) using a sampling technique. The sampling gates are driven by 300ps wide strobe pulses derived from

Figure 6.3 Block Diagram of 8754A Receiver Front End

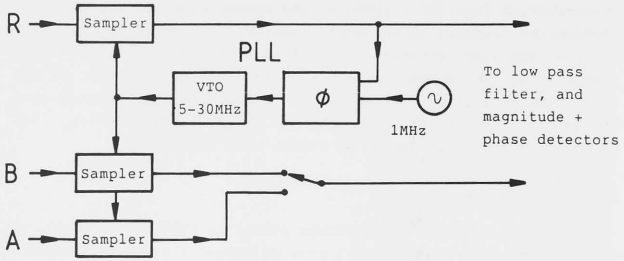

Figure 6.4 Down-conversion process for 29MHz RF input to 1MHz IF Output. The PLL sets the VTO frequency to 10MHz

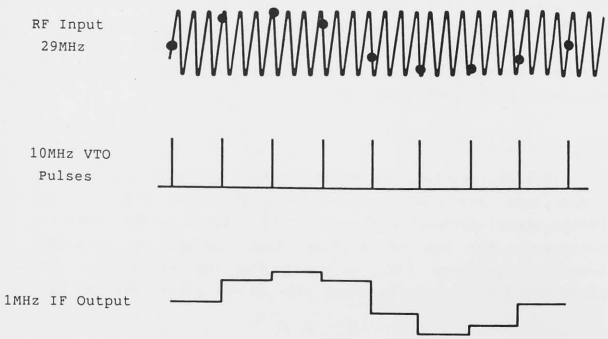

a voltage tuned oscillator (VTO) which has a 5-30MHz tuning range; a phase locked loop (PLL) ensures that one of the VTO harmonics is 1MHz greater than the RF on the 'R' receiver input. Thus the samplers act as harmonic mixers, preserving magnitude and phase relationships whilst time stretching the input waveforms to a lower, fixed frequency. A block diagram of this portion of the receiver is shown in Figure 6.3. Figure 6.4 illustrates the down-conversion process for a VTO frequency of 10MHz with an input RF frequency of 29MHz.

When sweeping over the whole frequency range available from the source, the VTO has to be retuned, and the PLL relocked every time it reaches the end of the VTO tuning range. During normal operation, this retune/relock process is performed automatically and is effectively invisible to the operator, because the control circuitry blanks the display and performs a short retrace during this period.

Detection in the dual receiver is performed on the frequency shifted IF signals; the detector outputs include signals proportional to phase and logarithmic magnitude over a possible 80dB dynamic range. These signals are fed into the display circuitry of the 8754A where they are processed to provide a trace on the CRT display. Displays of S_{11} magnitude or phase versus frequency or a polar plot of S_{11} with frequency (Smith Chart) may be selected. The display driver circuitry also provides rear panel VERT and HORIZ output jacks which effectively give an image of the displayed trace scaled as 100mV/div.

1.1.4. Control Inputs

A rear panel programming connector on the 8754A provides control functions which include switching from LOCAL to REMOTE mode, and the initiation of a relock cycle for the receiver PLL.

1.2. Digital Recorder

This section is a description of the function of the digital recorder, and an outline of its implementation. The interface

records both magnitude and phase of the reflection coefficient of the open-ended probe versus frequency. Further details of both the hardware and software used in the recorder, which are summarized below, are given in appendix 3.

1.2.1. Source and Receiver Tuning

The external tuning voltage for the 8754A is provided by a 12-bit digital to analogue converter (DAC) under software control. As discussed earlier, when the receiver VTO runs out of tuning range the VTO PLL must be relocked. Unfortunately, the 8754A gives no external signal to indicate that such a relock is necessary. As a simple solution to this problem, the recorder software relocks the PLL every time the source tuning voltage is changed, which ensures that repeatable measurements are obtained.

1.2.2. Receiver Outputs

The magnitude and phase outputs from the display circuitry are sampled by a 12-bit analogue to digital converter (ADC). By using the displayed outputs, it is possible to use the internal amplifiers and offset circuitry of the 8754A so as to make best use of the dynamic range available from the ADC. Switching between LOCAL and REMOTE mode is performed automatically via the programming connector, however manual selection of magnitude, then phase, is required.

1.2.3. Recorder Hardware and Software

The low-level interface hardware, i.e. the DAC and ADC, is driven by a BBC microcomputer system, which also provides control signals to the 8754A. The software is split into two logically distinct sections: the user interface, written in BBC BASIC, and the low-level interface driver, written in 6502 Assembler. The hardware driver is called from the BASIC program in order to execute various interface functions including sweeping the source frequency and sampling the reflection coefficient data from the receiver output. After a set of data has been sampled, it is recorded on floppy disk, together with a header that contains a

representation of the instrument settings. If required, the recorded data can be displayed on the BBC micro to provide a visual check that the system is operating correctly.

1.2.4. Sampling Algorithm

The voltage produced by the DAC is used to tune the 8754A source to one of a number of discrete (e.g. 512) frequencies, and after a suitable settling time, the ADC samples the detected output signal from the 8754A receiver. Thus an array of digital values is obtained; each element represents the value of the receiver output (either magnitude or phase), the index of the element is proportional to frequency.

The 12-bit ADC is configured so that a change in the least significant bit corresponds to 0.002dB when switched to 'Magnitude B/R' (1dB/div) and 0.1° when switched to 'Phase B/R' (45°/div). This resolution corresponds to about 0.2mV per bit at the input of the ADC, however, the measured noise at the receiver output was about 7mV in amplitude. Just as in the time domain measurement system, the signal to noise ratio of the signal from the 8754A can be improved by averaging. Either 'cyclic' averaging or 'sequential' averaging of the output signals can be performed.

In cyclic averaging, the source is swept through the frequency range N_a times. At the end of each sweep, the array of ADC values obtained is summed into a separate accumulator array. After all the sweeps have been performed, each value in the accumulator array is divided by N_a to obtain the required average.

In sequential averaging, the source is swept through the frequency range once only. At each of the discrete frequencies visited, the output signal is sampled N_a times and the sum of these samples formed. Before moving to the next frequency point, the accumulated value is divided by N_a.

Clearly there is a trade-off between the noise level and the time required to perform the recording. The sequential averaging technique has been used for the output from the 8754A - primarily

Figure 6.5 View of experimental arrangement showing the 8502A test set, an open-ended probe, the magnetic stirrer and the cooling pipes. Lagging material, and the support clamp for the 8502A have been omitted.

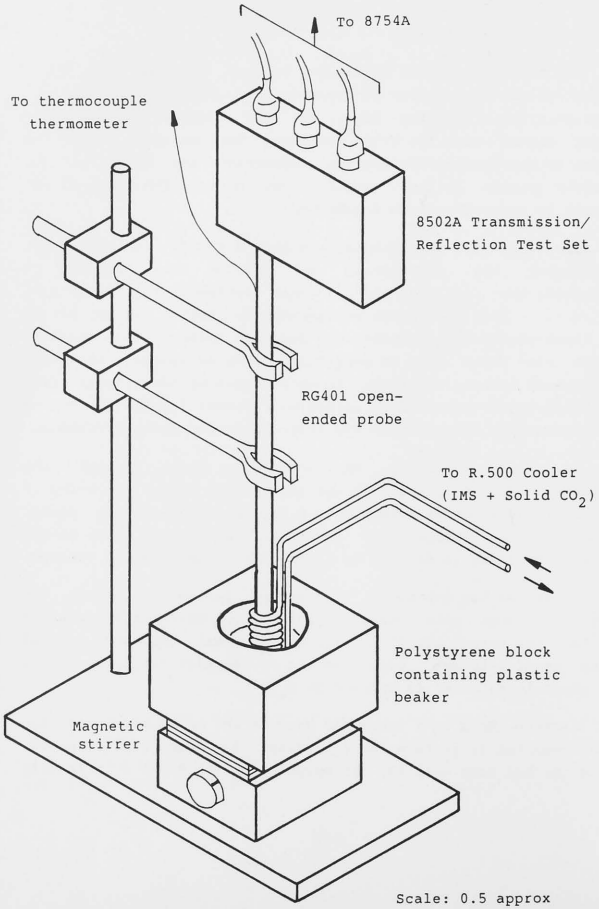

for speed. Rapid recording is needed to minimize the effects of any drifts that may occur - not in the instrumentation, but in the temperature of the dielectric material in contact with the probe. It takes approximately 4.5ms to change the source frequency and relock the receiver PLL, whereas it takes about 130μs to acquire, fetch, sum and store a sample. We have commonly used 512 frequencies and 128 summations; the cyclic technique would require over 10 minutes to record both magnitude and phase. In practice, the sequential technique takes about 25 seconds; an entire recording at one temperature can be completed in about 30 seconds.

2. Experimental Apparatus and Layout

This section concerns the remaining experimental apparatus used to perform dielectric measurements using the open-ended probe and 8754A Network Analyzer. Figure 6.5 is a sketch of the experimental arrangement which shows the 8502A test set, open-ended probe, magnetic stirrer and cooling pipes.

2.1. Room Temperature Measurements on Liquids

For measurements at room temperatures on liquids, it is convenient to use the open-ended probe vertically, so it can be dipped into the liquid under investigation. Temperature control is not required, since the liquid temperature (20°C) is stable to within $\pm$0.1°C when used with a magnetic stirrer. Figure 6.6a shows the open-ended probe dipped into a liquid held in a 50ml plastic beaker.

2.2. Low Temperature Measurements

2.2.1. Cryoprotectants

The apparatus used for low temperature measurements is very similar to that used at room temperature, but with the addition of a cooling system which allows the temperature to be controlled from +25°C to -35°C, as shown in Figure 6.6b.

Figure 6.6a
Open-ended probe dipped into the liquid to be measured.

Figure 6.6b
Detailed view of the probe, cooling pipes, and stirrer magnet. This is the experimental arrangement used for low temperature measurements on liquids (cryoprotectants).

Figure 6.6c
As 6.6b but showing position of tissue mass during measurements on perfused kidney.

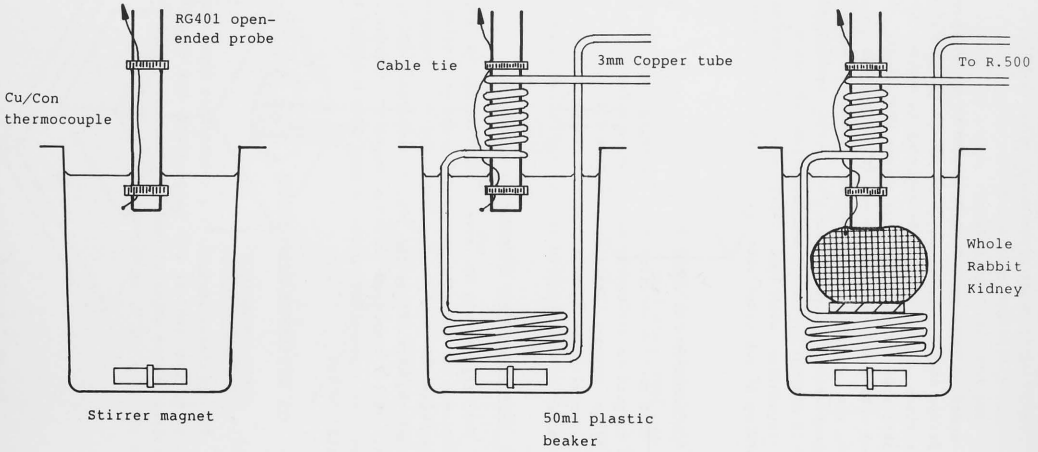

A coil of 3mm copper tubing is immersed in the liquid, and refrigerant - cold industrial methylated spirits (IMS) - is pumped through it. The cryoprotectant solution is cooled by conductive and convective heat transfer, the latter aided by the magnetic stirrer. The open-ended probe is also cooled by the tubing, this is necessary to prevent it heating the material under test. The minimum spacing between the probe tip and the piping was 15mm in all of the experiments. The temperature of the liquid is measured by a Comark 6200 thermometer with a copper-constantan thermocouple near the open-ended probe tip.

2.2.2. Perfused Tissue

The most important tissue measurements for organ cryopreservation are those of perfused tissue because the cryoprotectant forms a substantial fraction (~20%) of the volume. Figure 6.6c shows the experimental configuration used for measurements on perfused kidney tissue. The apparatus is the same as that used on liquids, only the perfused (whole) kidney is supported by a narrow perspex spacer that sits on the copper tubing (see Figure 6.6c). The tissue is immersed in the cryoprotectant, and the probe is pushed firmly against the surface. The pressure applied distorts the surface, but is not sufficient to puncture it.

Rabbit kidneys (and cryoprotectants) were supplied by the MRC Cryobiology Group at the Department of Surgery. Several hours before the dielectric measurement, kidneys were harvested from New Zealand albino rabbits and perfused with the cryoprotectant under investigation using the procedures described by Jacobsen *et al.* (1978). Perfusion of the cryoprotectant was performed at 10°C, the concentration of cryoprotectant in the perfusate is increased linearly at about 1% of the final concentration per minute; the whole process taking about 150 minutes. The kidneys were then bathed in a solution of the cryoprotectant, and kept on crushed ice during transportation to the Department of Engineering. Dielectric measurements were taken on the tissue as the temperature was cycled from room temperature

down to at least -30°C, then back to room temperature. Average cooling and warming rates were less than 1°C/min, each experimental run taking about four hours including calibration.

2.2.3. Refrigeration

The refrigerator used was a model R.500 Mk.4 cooler manufactured by G V Planer Ltd., which controls the temperature by alternately heating and cooling the IMS refrigerant (Pegg 1966). Heating is provided by a 500W electric heater, cooling by percolating the IMS over a block of dry ice (solid carbon dioxide). In practice, cooling is much more effective than heating, so that the 'bang-bang' temperature controller supplied with the R.500 is not very effective - the temperature oscillates wildly around the set point. Better control was obtained by operating the cooler manually, allowing the refrigerant to recirculate through the sump of the refrigerator (i.e. neither cooled nor heated). This kept the temperature approximately constant (within 0.5°C) during each measurement.

3. Experimental Procedures and Processing Software

This section describes the experimental procedures and associated software for performing calibration and error correction, and the software used for the calculation of the measured permittivity.

3.1. Choice of Data Processing Engine

The digital recorder sweeps the RF source of the Network Analyzer and samples the magnitude and phase outputs of the receiver, storing the data on floppy disk. In principle, the processing of the measured data to obtain dielectric data could be performed on the BBC microcomputer which forms part of the recorder. In practice the raw data is transferred via the University data network (UDN) for processing on an IBM 3081 mainframe computer.

There are several reasons for this approach. First, a typical experimental run of 40 temperature points produces about 300Kbytes of raw data which occupies three floppy disks. On the mainframe, storage and manipulation of this quantity of data is a trivial matter. Also, the data can be recorded on magnetic tape allowing accessible archival storage of both raw data and processed results. Second, the processing power of the mainframe is larger than the BBC micro by several orders of magnitude. This is enhanced by the availability of high level languages which can call on substantial program libraries of both numerical and graphical routines. The only disadvantage is that the processing is off-line, so errors in experimental procedures can only be detected some time (possibly hours) after the completion of the experiment. This was not found to be a serious limitation in this work.

3.2. Calibration

The actual data recorded for each frequency point consists of two 12-bit numbers which represent the averaged values of the code at the ADC output for magnitude and for phase. The recorder software translates each number into hexadecimal ASCII codes to allow simple data transfer via the UDN. Further details of the data format are given in appendix 3.

The DAC presents a tuning voltage between 0 and 10V (nom.) to the RF source, and the ADC samples the uncalibrated voltage at the VERT output jack of the 8754A. Thus the source frequency and the magnitude and phase outputs need to be calibrated. This requirement can be simply expressed as the need to determine the calibration constants (A_f,B_f), (A_m,B_m), (A_p,B_p) in the following three equations for frequency, return loss (dB) and phase (degrees):

$$f_i = A_f.i + B_f \qquad (6.1)$$

$$20\log_{10}|\rho_m(f_i)| = A_m.ADC_m[i] + B_m \qquad (6.2)$$

$$\frac{180}{\pi}.\arg\rho_m(f_i) = A_p.ADC_p[i] + B_p \qquad (6.3)$$

In this set of equations, i is the index which was sent to the interface DAC to set the RF source frequency to f_i, and $ADC_m[i]$ and $ADC_p[i]$ are the recorded ADC values for the magnitude and phase of the measured reflection coefficient $\rho_m(f_i)$. The calibration coefficients are determined from six recordings of different Network Analyzer configurations, given below.

3.2.1. Frequency Calibration

Frequency calibration is performed by recording 100MHz markers across the sweep range used; A_f and B_f are determined from linear regression of the spacing between the recorded markers.

3.2.2. Magnitude and Phase Offsets

The error correction procedure (discussed in the next section) allows us to calculate the permittivity without knowing the values of the magnitude and phase offsets, B_m and B_p, although they must remain constant throughout the sequence of measurements. However, approximate values were obtained - B_m was determined by recording '0dB' at some fixed frequency in the centre of the sweep range, and B_p by recording the '0°' reference level.

3.2.3. Magnitude and Phase Calibration

The range of return loss values generated by the probe in contact with tissue and cryoprotectants over a given frequency range varies by several dB, the largest range - about 8dB - was observed close to the liquid -> solid phase change. Over the temperature range -35°C to +25°C, the return loss varies from 0dB to about 12dB, and the phase of the reflection coefficient by about 200°. This range of return loss and phase values restricts the choice of magnitude and phase sensitivities on the 8754A, and for all the measurements these were set to 1dB/div and 45°/div respectively.

Magnitude calibration relies on the calibration of the

Figure 6.7a Return loss calibration record. The steps are produced by manually increasing the OFFSET control on the 8754A by 1dB steps from 0 to +7dB.

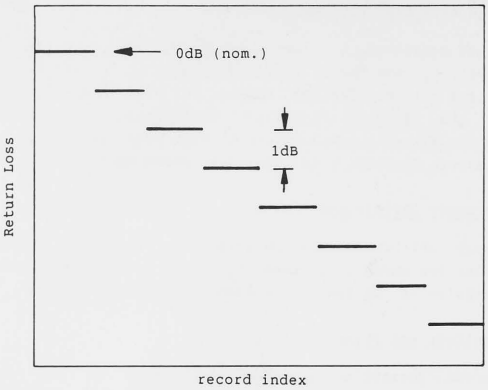

Figure 6.7b Phase calibration record. The record shows the phase output versus linear frequency for a remote open-circuit termination.

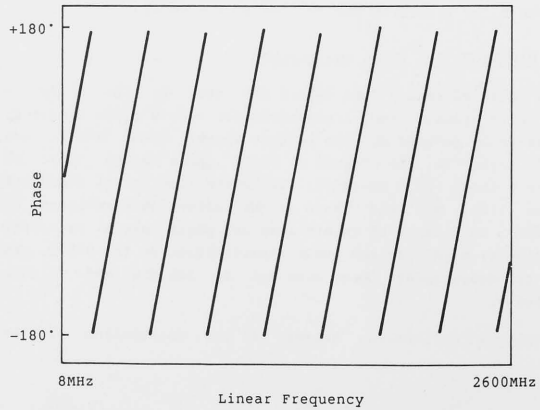

stepped attenuator on the 8754A front panel. As the frequency is swept by the recorder, the attenuator is manually stepped from 0 to +7dB in 1dB steps. The resulting (synthetic) magnitude record is shown in Figure 6.7a; A_m is calculated by linear regression of the step heights.

The cable lengths between the test set and the 8754A were matched to the length of the open-ended probe so that no phase discontinuities appear in the measured data (to avoid the +180° -> -180° jump). Phase calibration is performed by recording the phase with the probe removed. This produces an open circuit at the test set input connector with an apparent phase of 2500° at 2600MHz, generating eight discontinuities where the displayed phase jumps from +180° to -180°. Figure 6.7b shows the resulting phase record; the maximum and minimum ADC values corresponding to these extremes of phase are used to calculate A_p. Clearly, it is possible to obtain B_m and B_p from these recordings too, so they were used as a check of the calibration procedure.

3.3. Error Correction and Permittivity Calculation

In chapter 5, expressions for calculating the measured permittivity were derived. These expressions, which perform simultaneous error correction and probe calibration have been used for processing all the measured data.

3.3.1. Equivalent Circuit Models

Both of the equivalent circuit models for the probe admittance discussed in chapter 5 have been used. In the simple model, the probe is modelled by a fringing capacitance in which the capacitance is linearly related to the permittivity. The more complex non-linear model includes a radiation conductance term.

From the experimental point of view, there is little difference between the two models, except for the number of reference materials that need to be recorded. In order to perform the error correction using the linear model, three references are required. In the majority of the measurements, these were (i) the

open-ended probe short-circuited by a piece of aluminium foil, (ii) the probe in air, and (iii) in 100mM saline. This choice of references produces an extremely simple expression for the permittivity of the material under test which can be written as a simple bilinear transformation

$$\varepsilon_m[i] = C_0[i] \frac{\rho_m[i]-C_1[i]}{\rho_m[i]-C_2[i]} \qquad (6.4)$$

where $C_0[i]$, $C_1[i]$ and $C_2[i]$ are pre-computed from the reference materials using the following set of expressions. For each value of the frequency index i,

$$C_0 = \frac{\varepsilon_3(\rho_1-\rho_3) + \varepsilon_2(\rho_2-\rho_1)}{\rho_3-\rho_2} \qquad (6.5a)$$

$$C_1 = \frac{\rho_2\varepsilon_3(\rho_1-\rho_3) + \rho_3\varepsilon_2(\rho_2-\rho_1)}{\varepsilon_3(\rho_1-\rho_3) + \varepsilon_2(\rho_2-\rho_1)} \qquad (6.5b)$$

$$C_2 = \rho_1 \qquad (6.5c)$$

In the above equations, ρ_1 is the measured reflection coefficient of a short circuit at frequency f_i. The reflection coefficients ρ_2 and ρ_3 are those recorded when the probe is dipped into the reference materials with permittivity ε_2 and ε_3.

The non-linear model requires four reference materials; these were generally the same as the previous set of recordings with the addition of (iv) ethanediol or methanol. Determining the permittivity is more difficult than the transformation in (6.4) - it requires the solution of a fifth order polynomial with complex coefficients, although the result is generally more accurate.

3.3.2. Choice of Reference Materials

There are two basic criteria: the references should be as accurate as possible, and also produce reflection coefficients as different as possible from one another. The short circuit reference can be provided accurately and conveniently and its use

allows considerable simplification in the form of the error correction expression. Similar remarks apply to the open-ended probe in air, the choice of the other references is a little more difficult.

Kraszewski et al. (1983a) have examined the uncertainties associated with dielectric measurements of water (Schwan et al. 1976) and methanol (Jordan et al. 1978), and concluded that the dielectric permittivity of water is more accurately known. However in the range of frequencies used here, i.e. below 2.6GHz, water is not as lossy as methanol and the real part of the permittivity much greater so that the volume of liquid interrogated by the probe is necessarily larger. This idea has been confirmed experimentally - when dipped in water, the probe appeared to be sensitive to metallic objects placed even 50mm from the tip. The errors induced were manifest as a series of distinct resonances in the measured permittivity whose frequencies clearly depended on distance between the object and the probe. For these reasons, we decided to use a lossy liquid whose properties were close to those we were trying to measure - 100mM saline, using the Stogryn formula for the calculation of reference permittivities (Stogryn 1971). Other liquids used either as references, or to evaluate the performance of the system include ethanediol and methanol from Jordan et al. (1978), and propan-1-ol from Garg and Smyth (1965) and Von Hippel (1954; p362).

4. Errors and Uncertainty

4.1. Systematic Errors

There are several possible sources of error in the dielectric measurement system that has been described. The error correction technique discussed in the previous section removes systematic errors due to imperfections in the RF hardware e.g. the connectors and the directional bridge in the test set. The correction is performed separately at each frequency, which effectively eliminates frequency dependent variations in the system magnitude

Figure 6.8 Dielectric measurements of the permittivity of ethanediol. The solid curves are from the measured data of Figure 5.5 de-embedded using the non-linear admittance model of equation (5.04). The dashed line is taken from the measurements of Jordan et al. (1978). The dotted lines are the uncertainties corresponding to reflection coefficient uncertainties of 0.03dB and 0.2°.

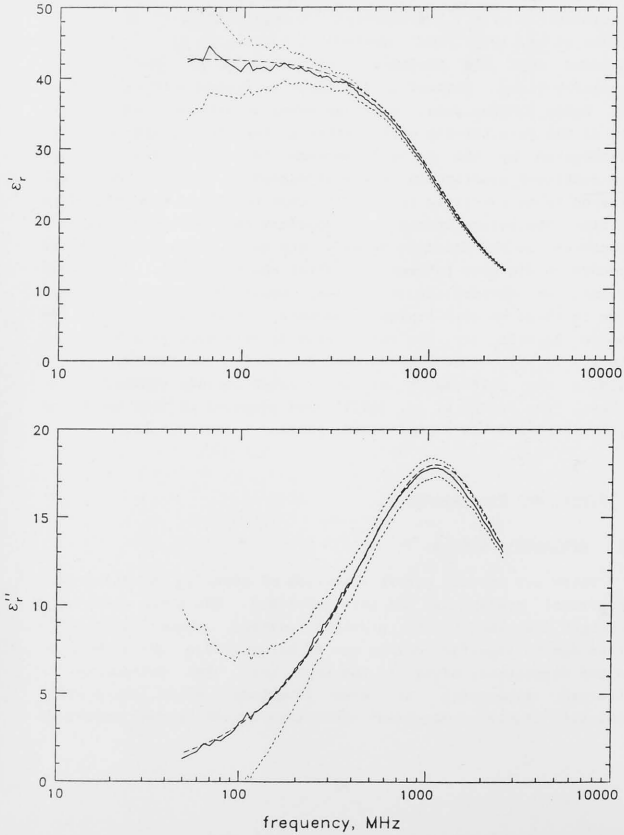

and phase response.

Other sources of error remain. These include the inadequacy of the equivalent circuit model to represent the fields at the probe tip, the probe surface conditions, and the effect of the proximity of metallic objects i.e. the cooling pipes. When lossy materials, such as cryoprotectants, are being measured, the effects of metallic objects are not detectable, provided they are more than 5mm from the probe. The probe surface changes with temperature because the PTFE dielectric has a different thermal expansion coefficient to the copper conductors. This effect was reduced by heat treating the probe during fabrication, as described in the previous chapter.

The length change of the probe due to thermal contraction when cooled by 50°C is about 0.1mm, corresponding to a phase change of about 0.03° at 100MHz and 0.9° at 2600MHz. This error in the measured reflection coefficient depends on the probe temperature distribution which is very difficult to estimate. Fortunately, the probe is more sensitive to errors at low frequencies, where the effect of the length change is much less severe. Nevertheless, an experimental check of the magnitude of this effect is required e.g. measuring the dielectric properties of hot saline.

Chapter 5 showed how uncertainty estimates for the measurement of the probe reflection coefficient could be used to provide estimates of the resulting uncertainties in the real and imaginary parts of the measured permittivity. From the manufacturers data, the 8754A receiver magnitude uncertainty is specified as better than 0.3dB, and the phase uncertainty as better than 2°. Around 0dB, this magnitude uncertainty corresponds to approximately 0.033 in ρ, the phase error is 0.035rad. These measurement uncertainties are extremely pessimistic, and imply uncertainties in the calculated permittivity that are much too large. Instead, the predicted uncertainties in the permittivity can be found for measurements on known dielectric materials for a range of values of reflection coefficient uncertainties. Figure 6.8 shows the result of a

Figure 6.9 Dielectric measurements of ethanediol. The data show the effect of changing the number of summations used on the measured permittivity.

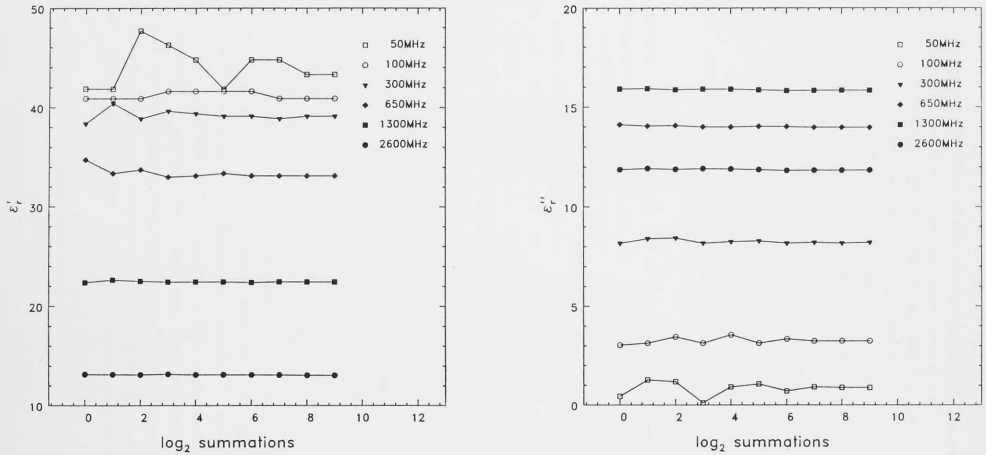

measurement on ethanediol (solid line), the known permittivity from Jordan et al. (1978) (dashed) and the predicted uncertainty limits (dotted) for magnitude and phase uncertainties of 0.003 and 0.003rad, corresponding to 0.03dB and 0.2° for the error-corrected Network Analyzer. These uncertainties are close to the resolution limit of the 12-bit ADC (see section 2.2.4). The error correction was performed using the non-linear admittance model, with short circuit, air, 100mM saline and methanol as reference materials (data from chapter 5). Clearly, for this set of materials the non-linear equivalent circuit model appears to be sufficiently accurate, however we note in passing that the error correction procedure allows the circuit parameters to change arbitrarily with frequency.

4.2. Non-Systematic Errors

There are several non-systematic errors inherent in the measurements which are not anticipated by the error correction procedure. These include noise and drift in the source and receiver circuits of the 8754A, temperature gradients in both cryoprotectants and in tissue, and biological variation in the properties of each kidney.

4.2.1. System Noise

The effect of noise on the measurements is reduced by averaging. Figure 6.9 shows the effect of changing the number of summations on the resultant measured permittivity of ethanediol. It is clear that the lower frequencies are more susceptible to the noise introduced by using too few summations, and that 128 summations are adequate here.

4.2.2. System Drift

According to the specification, the 8754A source is stable to within 0.4MHz/°C and 0.1MHz/hr. A typical experimental run covering a range of temperatures takes about four hours, during which ambient temperature remains constant to within 1°C, so that the maximum drift is less than 2MHz. However, no figure is given

Figure 6.10 Dielectric measurements of ethanediol. The probe reflection coefficient was recorded at 10 minute intervals for 5 hours after power up.

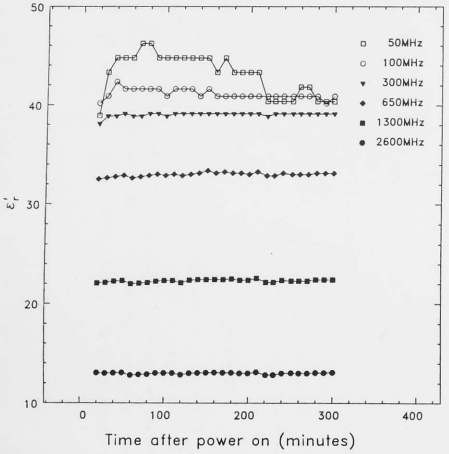

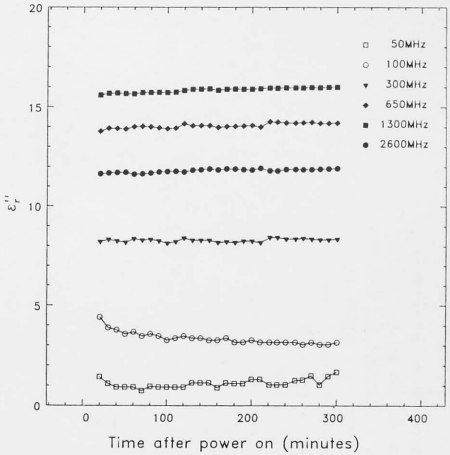

by the manufacturer for the drift of the phase and magnitude response.

Figure 6.10 shows the results of an experiment which was intended to evaluate the effects of this drift. The probe was dipped into ethanediol at room temperature and the reflection coefficient recorded at 10 minute intervals for 5 hours, beginning when the network analyzer was first powered up from 'cold'. At the end of this period, the calibration and error correction records were taken. The resultant permittivities show that the effects of all sources of drift are small, even from power up. In practice, the effect of drift was minimized by allowing at least four hours for the 8754A to warm up before starting a measurement sequence. Another feature that can be seen in Figure 6.10 is that the measured permittivity appears to change in discrete jumps - this is particularly obvious at 50MHz. These jumps correspond to 1-bit changes in the original recordings, which tends to confirm our previous remarks concerning measurement uncertainties.

4.2.3. Temperature Control and Biological Variation

One of the most difficult errors to assess is the effect of inhomogeneities in the mass of half-frozen cryoprotectant or tissue caused by non-uniform heat transfer. It is hoped that these errors were minimized as far as possible by changing the temperature slowly; separate sets of measurements were made both as the material was cooled and warmed so the effects could be assessed (see chapter 7).

One problem which applies to measurements on tissue is the effect of 'biological variation' i.e. variation between individual animals. In practice, measurements were taken on organs taken from different animals (of the same genetic strain) so variations might be expected. Unfortunately, the resources available did not permit us to perform sufficient number of experiments to assess this variation statistically.

Figure 6.11a Experimental configuration used for time domain measurements of the open-ended probe admittance.

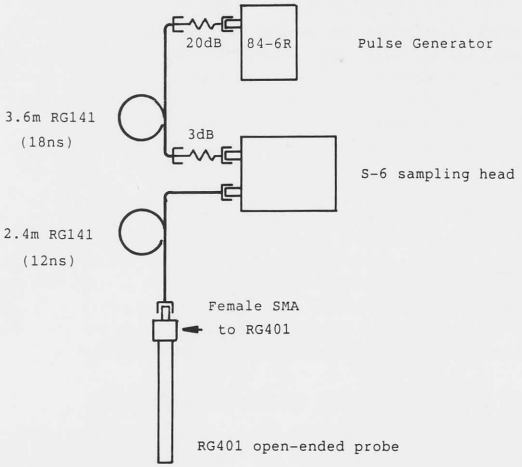

Figure 6.11b Waveform from 84-6R pulse generator.

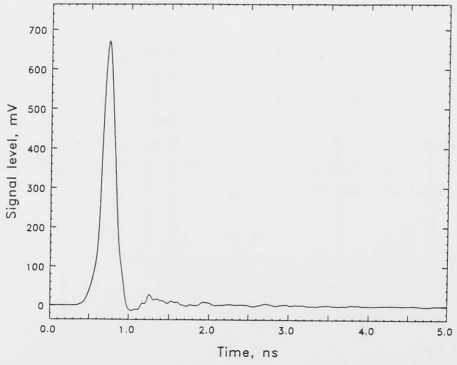

5. Time Domain Dielectric Measurements Revisited

This section describes how dielectric measurements using the open-ended probe can be made using time domain instrumentation. It is included in this dissertation to further illustrate the utility of the simultaneous error correction and calibration procedure, and as a contrast to the error correction techniques described in chapter 4. The time domain system has not yet been used for measurements on cryoprotectants over a range of temperatures, although its operation has been demonstrated experimentally, as described below.

5.1. Experimental Configuration

Figure 6.11a is a schematic diagram of a pulse generator, S-6 sampling head, RG141 delay lines and RG401 (0.25") open-ended probe. The S-6 'loop-thru' sampling head is carried in a 7S11 sampling unit, and a 7T11 sampling sweep unit provides the timing signals.

Such a system configuration is commonly used for time domain reflectometry - the only difference here is that the pulse generator used produces a narrow impulsive spike rather than a fast rising step waveform. The pulse generator‡, which is based on a step recovery diode pulse sharpener, was built by H C Reader in this Department; the rise time is about 60ps and the peak output voltage is about 12V (Reader 1985). Figure 6.11b shows the waveform produced by the pulse generator as it passes through the sampling head. The amplitude is much reduced before reaching the S-6 after passing through two attenuators (20 + 3dB) and a 3.6m length of RG141 delay line (18ns delay) - these are used to isolate the sampling head from the generator. Recordings of the various time domain waveforms were made using the digital recorder hardware and software described in chapter 4 and appendix 3.

Figure 6.12a shows the waveform observed from the practical

‡ Pulse generator 84-6R

Figure 6.12a Observed waveform from the practical time domain measurement system.

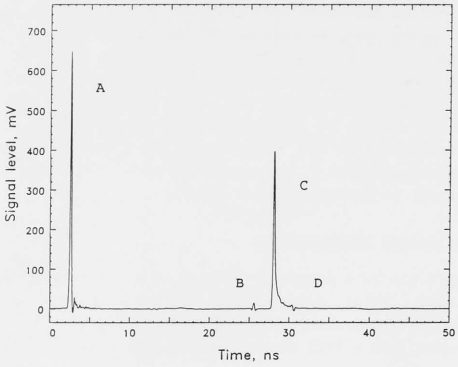

Figure 6.12b Schematic diagram showing the link between features of the measurement system and the observed waveform.

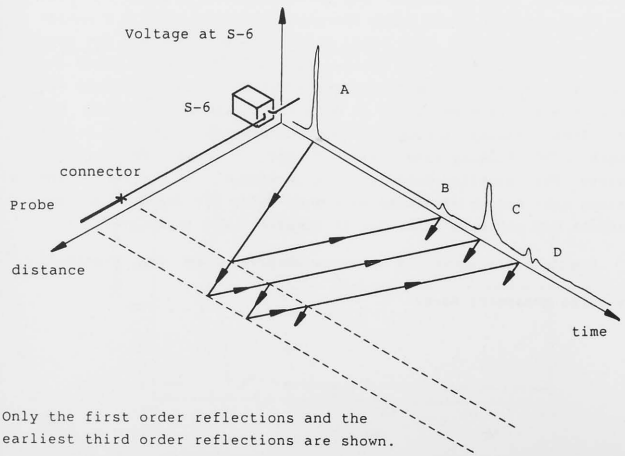

Only the first order reflections and the earliest third order reflections are shown.

measurement system on a long time scale. Figure 6.12b is a schematic diagram of the S-6 and open-ended probe together with a sketch of the observed waveform showing four distinct features of the time domain trace. The 'A' portion of the waveform is essentially the pulse which passes through the S-6 i.e. as Figure 6.11b, and the 'B' portion is the reflection of this pulse from the SMA connector at the proximal end of the RG401 probe. The 'C' portion of the waveform is the reflection of the pulse from the discontinuity at the distal end of the probe which is dipped in the material to be measured, as before. Finally, 'D' is the first multiply reflected signal from the probe and RG401 to SMA connector (see diagram).

5.2. Reflection Coefficient Calculation

If the measuring system were ideal - reflectionless connectors and lossless lines, then the 'C' waveform would simply be the time domain convolution of the 'A' waveform with the impulse reflection coefficient of the probe r(t) i.e.

$$c(t) = a(t) * r(t) \tag{6.6}$$

where '*' represents convolution. The frequency domain reflection coefficient of the probe can be recovered at a discrete number of frequencies using the discrete Fourier transform (DFT)

$$\rho_m(f_i) = \mathrm{DFT}[c(t)]_i \; / \; \mathrm{DFT}[a(t)]_i \tag{6.7}$$

However, the measured reflection coefficient using real connectors and real cabling is far from this ideal. The observed waveforms shown in Figure 6.12 consist of both this 'wanted' set of reflections and a set of 'parasitic' reflections from connectors and delay lines.

5.3. Application of the Direct De-embedding Procedure

The simplest way around the parasitic reflection problem would be to make the probe longer which would increase the separation between the troublesome discontinuities, thus excluding them from the time window. However, this is an inherently

approximate method that relies on ideal delay lines, and on S_{21} of the probe connector being very close to 1.

In the work described in chapter 4, the approach taken towards untangling the nest of multiple reflections was to set up lossless, reciprocal scattering matrices to represent each of the discontinuities produced by the connectors. Each scattering matrix was determined from additional measurements on the connectors alone. Finally, the scattering parameters of the strip-line sample holder were computed using this connector characterization. Whilst this technique did achieve some accuracy improvement, chapter 5 suggests a different approach.

The scattering parameters of the connectors per se are not very interesting - we only wish to use them to de-embed a measured admittance. In fact the time domain measurement system outlined above can be assigned exactly the same error model as the frequency domain network analyzer instrumentation. The experimental procedure is summarized below for the linear admittance model; it is simple to extend to the non-linear model:

a) Record three sets of reflected waveforms from the probe in contact with reference materials - short circuit, air and 100mM saline are suitable as before, call these $r_1(t)$, $r_2(t)$ and $r_3(t)$.

b) Record the reflected waveform for the material under test: $r_m(t)$. Each waveform is the convolution between the signal from the pulse generator, a(t) and the impulse reflection coefficient of the error network terminated by the probe. Figure 6.13a shows such a recording for the probe dipped in propan-1-ol at 20°C.

c) Now use the DFT to produce frequency domain versions of these four records as follows:

$$\rho'_j(f_i) = A(f_i).\rho_j(f_i) = A(f_i).DFT[r_j(t)]_i \qquad (6.8)$$

for j = 1,2,3,m, where $A(f_i)$ is the ith component of the DFT of a(t). The $\rho'_j(f_i)$ can now be substituted directly into the

Figure 6.13a Time domain recording of the reflection from the open-ended probe dipped in propan-1-ol.

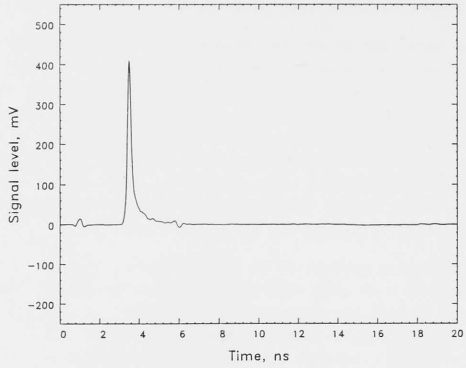

Figure 6.13b Measured permittivity of propan-1-ol from the time domain recording above. Reference materials used: short circuit, air, 100mM saline and ethanediol with the non-linear admittance model.

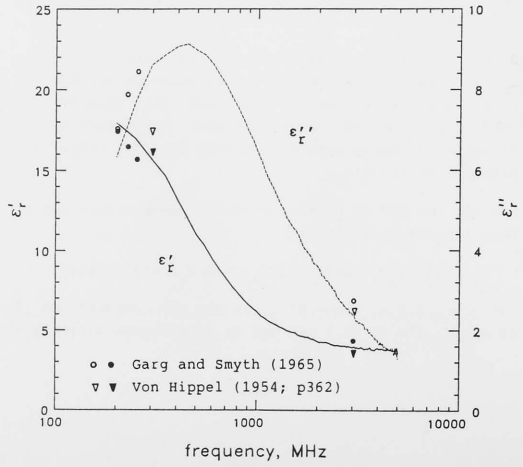

bilinear transform expression of (6.4) and (6.5a-c) to obtain the permittivity directly, as before.

Note that it is **unnecessary** to record the incident pulse a(t) at all - the essential point is that the value of $A(f_i)$ is the same for each measurement, though it may well be frequency dependent. Using the linearity property of the error correction procedure given in chapter 5 means the $A(f_i)$ term will cancel at each frequency.

The 'B' portion of the waveform must be recorded, although it could be excluded from the time window, this is necessary for two reasons. Firstly, it forms an important part of the error network, and secondly it is used to correct drift in the sampling oscilloscope time base. Drift of the time zero is a serious problem in time domain instrumentation (see chapter 4). The first reflection from the connector ('B') should be in the same time position (with respect to the 7T11 trigger) on every record, so this can be used as the time reference.

5.4. Performance

Only a limited amount of experimental work has been performed with this configuration. As an example, Figure 6.13b shows the measured permittivity of propan-1-ol from 200MHz to 5GHz using four references: short circuit, air, 100mM saline and ethanediol, with the non-linear admittance model. The results obtained are as good as those obtained with the frequency domain system, though extending to higher frequencies. Calibration is much simpler, and the system is potentially faster because only one recording per measured material is required.

Chapter 7

Dielectric Measurements for Organ Cryopreservation

This chapter presents the dielectric data resulting from measurements made on cryoprotectant solutions and on perfused rabbit kidney tissue. All these measurements were made using the open-ended coaxial probe and frequency domain Network Analyzer described in chapters 5 and 6.

A large volume of data has been collected, so a compact presentation is required. Section 1 discusses the format used for presentation of the dielectric measurements in this chapter. In section 2, dielectric measurements over a wide temperature range on existing cryoprotectants and perfused tissue are given. The formulation of a new cryoprotectant is introduced in section 3, and dielectric measurements on both the new cryoprotectant, and on perfused rabbit kidney tissue are described.

Section 4 discusses practical details of the measurements, and some of the problems encountered, whilst section 5 makes some recommendations concerning design of an electromagnetic rapid rewarming system for organs. Section 6 concludes the dissertation, and offers suggestions for further work.

1. Presentation of Dielectric Data

Much of the dielectric data presented in this dissertation has been as plots of the real and imaginary parts of the complex permittivity against frequency. Cryoprotectant solutions are quite lossy over the range of frequencies measured here, and it is more convenient to plot the imaginary part of the complex permittivity as the corresponding effective conductivity (see chapter 2).

Instead of plotting a separate graph for each temperature, the data has been condensed onto one plot. The temperature scales

Figure 7.1 Electrical properties of rabbit kidney perfused with HP6 plus 3M glycerol cryoprotectant solution.

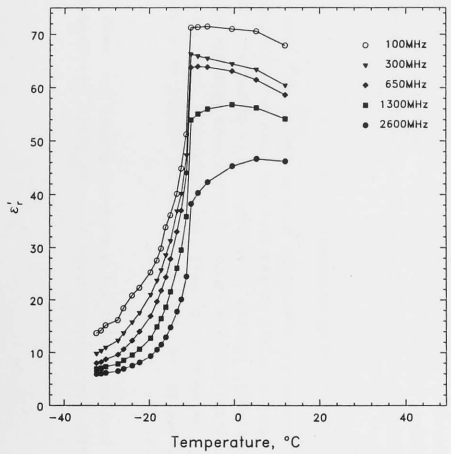

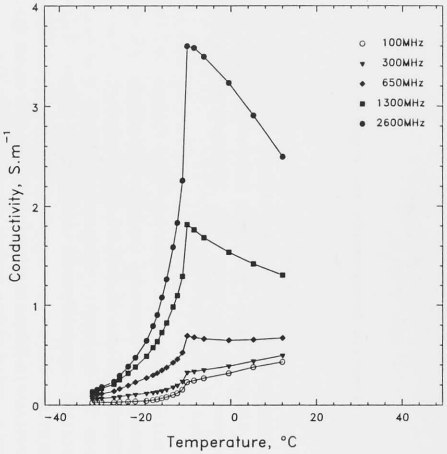

Figure 7.2 Electrical properties of HP6 plus 3M glycerol cryoprotectant solution.

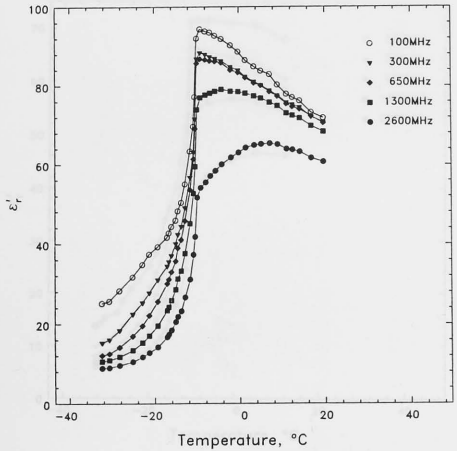

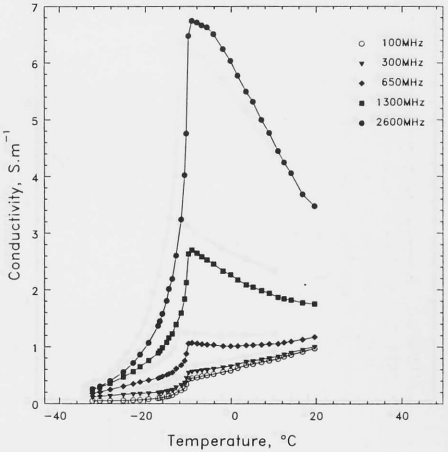

Figure 7.3 Power penetration depth in (a) perfused tissue and (b) HP6 plus 3M glycerol cryoprotectant

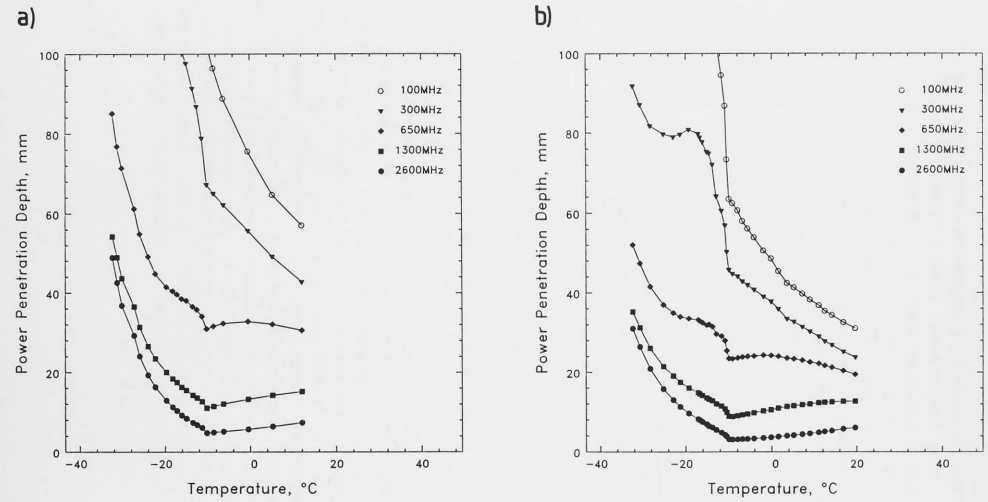

are fixed throughout, although the temperature range covered in each case does differ. Lines of constant frequency are drawn so that the variation of dielectric properties with temperature can be clearly seen. This is particularly relevant to applicator design, since it is likely that warming would be carried out at one frequency. The frequencies plotted (in all cases) cover the range of measured values in a logarithmic fashion - 100MHz, 300MHz, 650MHz, 1300MHz and 2600MHz.

2. Dielectric Measurements

Three cryoprotectant solutions have been investigated. Two of these solutions have been used in organ cryopreservation experiments by other workers, the third is an attempt to design a new cryoprotectant which has electrical properties that make it more suitable for rapid warming.

2.1. HP6 + 3M Glycerol

This cryoprotectant solution has been used experimentally by Pegg and co-workers at the Department of Surgery. The 'recipe' for this and the other cryoprotectants is given in appendix 2. The abbreviation 'HP6+3Mg' is used to denote this solution.

Figure 7.1 shows the permittivity and effective conductivity of rabbit kidney tissue perfused with HP6+3Mg cryoprotectant over -32°C to +12°C. Figure 7.2 shows the dielectric properties of HP6+3Mg alone, over -32°C to +20°C. These curves illustrate one general feature that was observed for all the perfused tissue measurements; that is, the temperature dependence of the dielectric properties of perfused tissue is very similar in form to those of the cryoprotectant solution alone, over the frequency range shown here. Consequently, much information can be obtained from the study of raw cryoprotectant solutions. However, the absolute values of the conductivity and permittivity do differ; generally, both parameters are smaller in perfused tissue.

Another feature visible in these two curves is the reversal of the temperature dependence of the effective conductivity in the thawed state, which appears to occur around 600MHz in both perfused tissue and cryoprotectant solution. Below this frequency, the temperature coefficient is positive, increasing as the frequency reduces. Above this frequency, the coefficient is negative, becoming more so at higher frequencies. Note, however, the drastic change in effective conductivity either side of the phase transition, which is more severe at high frequencies.

Chapter 2 showed that a particularly relevant parameter in electromagnetic heating is the power penetration depth, which is solely a function of the dielectric properties. Figure 7.3 shows the calculated power penetration depth for both (a) perfused tissue and (b) HP6+3Mg cryoprotectant. These diagrams demonstrate that the power penetration depth in tissue at or above 1300MHz is simply too shallow compared with the minimum dimensions (~20mm) of rabbit kidney (see Figure 1.3). At 2600MHz, the minimum power penetration depth which occurs at the phase transition - probably the worst place - is merely 5mm.

2.2. Modified Sachs Solution + 1.4M DMSO

This is the cryoprotectant solution used by Guttman et al. (1977) and Pegg et al. (1978) in their electromagnetic rewarming experiments on dog kidney, in which warming was carried out using a domestic microwave oven operating at 2.45GHz. The composition is detailed in appendix 2, and the abbreviation 'MS+DMSO' is used to denote this solution.

Only the dielectric properties of the cryoprotectant solution have been measured - the results, taken over -31°C to +25°C, are shown in Figure 7.4, the power penetration depth is shown in Figure 7.5. The temperature dependence, and the actual values obtained for the dielectric properties and power penetration depth of this cryoprotectant are quite similar to those of HP6+3Mg.

Once again, the power penetration depth at 2600MHz is about 5mm. This fact, together with the difficulty of producing

Figure 7.4 Electrical properties of modified Sachs solution with 1.4M DMSO cryoprotectant.

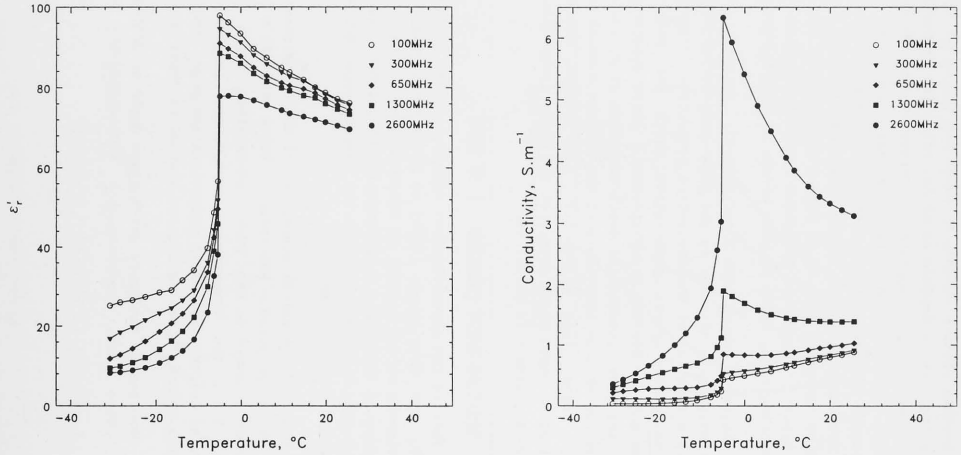

Figure 7.5 Power penetration depth in modified Sachs solution with 1.4M DMSO cryoprotectant.

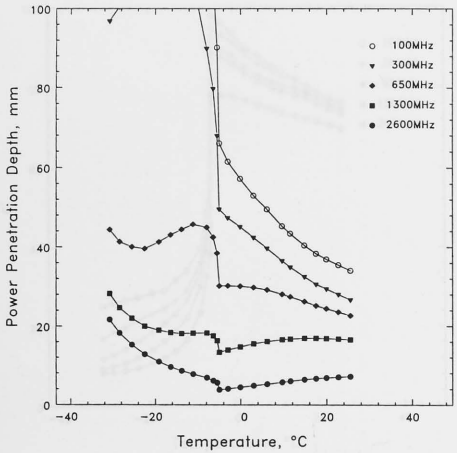

controlled exposure conditions in a microwave oven, offers a tentative explanation for the problems experienced by both Guttman et al. (1980) and Pegg et al. (1980) in their attempts to reproduce the originally successful experiments. At low temperatures, the penetration depth is about 20mm at 2600MHz - this would be sufficient to cause a significant variation in power deposition with depth. As the temperature increases, the problem worsens, until at the phase transition, only the outside 'shell' of the organ would be heated at all.

3. Modified Cryoprotectant Solutions

Both of the cryoprotectant solutions in the previous section show markedly similar electrical behaviour. It is possible to alter the composition of a cryoprotectant solution - as remarked in chapter 1, the existing compositions are somewhat arbitrary. Clearly it is constructive to examine the composition of a cryoprotectant solution if modifications are to be made.

3.1. The Composition of Cryoprotectant Solutions

Cryopreservation solutions generally contain a fairly concentrated associated liquid e.g. 3M glycerol - the cryoprotectant. The other components of the cryopreservation solution, electrolytes and other additives, are included to prevent osmotic damage to the cells; these electrolytes also affect the dc conductivity of the cryoprotectant solution.

It is apparent in both HP6+3Mg and MS+DMSO that the dc conductivity of the solutions dominates the effective conductivity below 300MHz, and that below this frequency, the conductivity increases with increasing temperature. Chapter 2 showed that the dc conductivity of 150mM saline has a positive temperature coefficient. Physically, this can be thought of as the effect of the increased mobility of hydrated ions with temperature. Below the centre frequency of a dielectric relaxation the temperature coefficient of the dielectric loss is negative (which is what we want). The interplay between the conductive loss and the

Figure 7.6 Electrical properties of 3M glycerol solution containing varying concentrations of mannitol and saline at 20°C (see text).

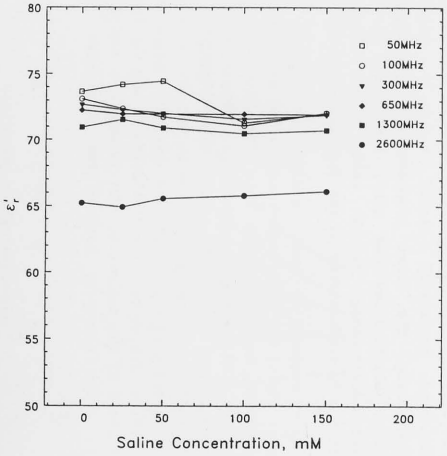

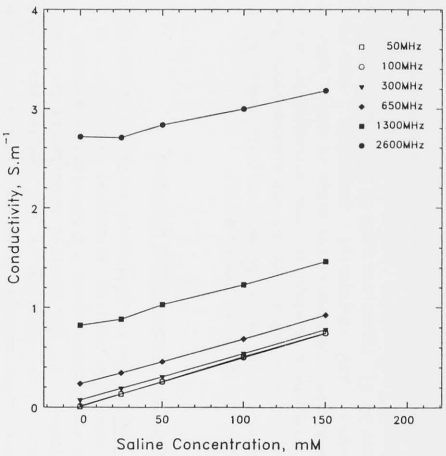

Figure 7.7 Electrical properties of 3M glycerol solution containing 269mM glucose.

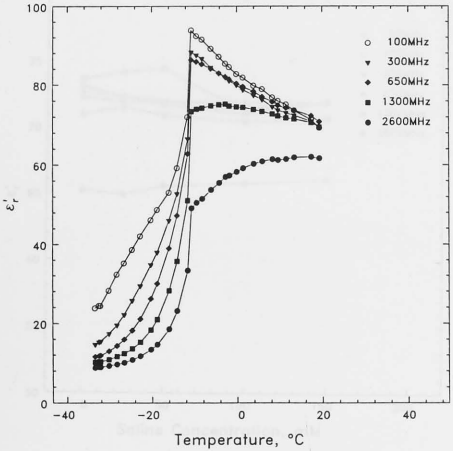

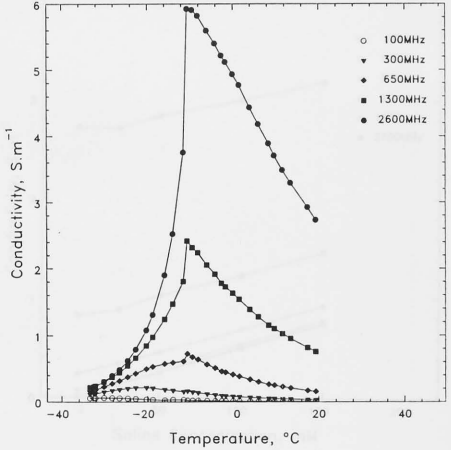

dielectric loss produces the observed effective conductivity profiles.

If the dc conductivity could be decreased, this would allow heating to be performed at lower frequencies, where power deposition would be more uniform, without incurring the penalty of a strong positive temperature coefficient.

3.2. Decreasing the Conductivity

Coffey and Andrews (1983) investigated the various preserving solutions used for hypothermic (0-2°C) preservation of renal tissue. The composition of such solutions, which are the basis of many cryoprotectant solutions, attempt to mimic the intracellular environment. Coffey and Andrews suggested that this might not be appropriate at low temperatures when the transmembrane ion pumps are severely disabled, and that some of the electrolytes could be replaced by sugars. They performed experiments which showed that the post preservation tissue morphology was greatly improved by replacing one half or more of the electrolytes by sucrose. Clearly this would reduce the dc conductivity of the cryoprotectant, as required, suggesting the experiments described below.

Figure 7.6 shows the effect of changing the saline concentration from 150mM to 0mM on the room temperature (20°C) permittivity and effective conductivity of 3M glycerol. At each concentration, sufficient sugar (mannitol here) is added to maintain the osmolarity of the impermeant species at 300mOsM. The changing saline concentration has little effect on the real part of the permittivity, but the effective conductivity shows an approximately linear variation with concentration. Similar behaviour is observed for both sucrose and glucose.

Figure 7.7 shows the dielectric properties of 3M glycerol with 269mM glucose added over -34°C to +19°C. This can be thought of as the 'best possible' behaviour in that there are no ions, and hence no dc conductivity, consequently, the temperature coefficient of the effective conductivity is always negative above

Figure 7.8 Electrical properties of rabbit kidney perfused with C&A+3Mg low conductivity cryoprotectant solution.

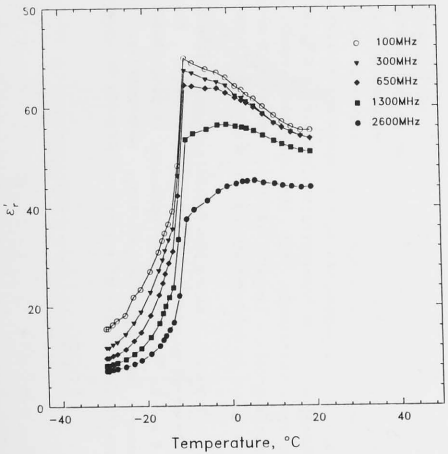

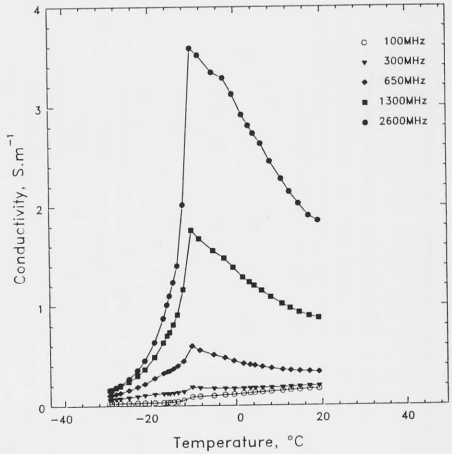

Figure 7.9 Electrical properties of C&A+3Mg low conductivity cryoprotectant solution.

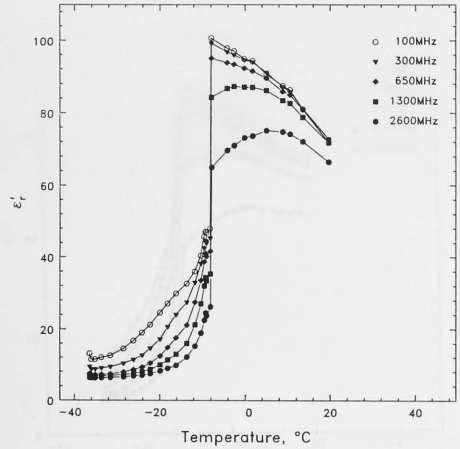

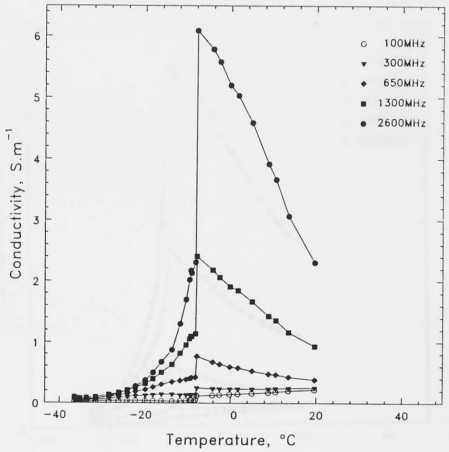

Figure 7.10 Power penetration depth in (a) perfused tissue and (b) C&A+3Mg low conductivity cryoprotectant solution

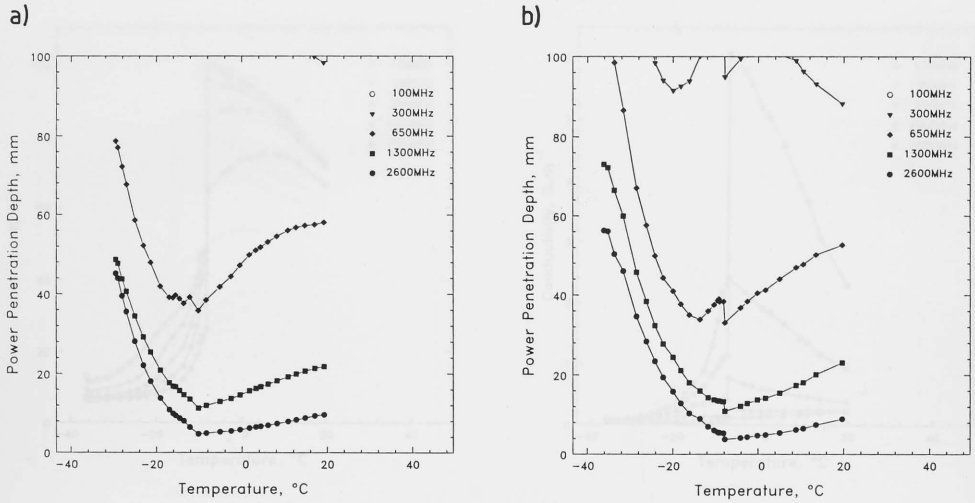

the phase transition for the frequencies shown here. Note that at 300MHz, the temperature coefficient is negative even below the phase transition (-10°C). Of course, the electrolytes within the cells of tissue to be preserved cannot be removed, so it is unlikely this 'zero dc conductivity' state could be achieved.

3.3. An Experimental Cryoprotectant

After consultation with our colleagues at the Department of Surgery, we decided to examine the effect of such a modified cryoprotectant on tissue, to see if it did produce improved dielectric behaviour. The final composition used was 50mM saline, 169.7mM sucrose and 3M glycerol; this experimental cryoprotectant solution is referred to as 'C&A+3Mg'. Figure 7.8 shows the permittivity and effective conductivity of rabbit kidney tissue perfused with C&A+3Mg over -30°C to +19°C. Figure 7.9 shows the permittivity and effective conductivity of C&A+3Mg over -37°C to +20°C. Figure 7.10 is the power penetration depth for the (a) the perfused tissue and (b) C&A+3Mg cryoprotectant. As with HP6+3Mg, the temperature dependence of the dielectric properties of the cryoprotectant and the perfused tissue are very similar in form. Note, however, that above the phase transition the temperature coefficient of the effective conductivity is now negative at 650MHz, and flat at 300MHz, confirming the ideas outlined above. Also, the power penetration depth at 300MHz is greater than 90mm over the whole temperature range for C&A+3Mg, whereas it drops to about half this value in HP6+3Mg.

4. Experimental Details and Practical Problems

4.1. Cooling and Warming Curves

For all measurements, separate freezing and warming curves were recorded however, only cooling curves have been given so far. This is because the probe tended to lift off the material being measured when it was close to the melting point, giving erratic results around those temperatures. Figure 7.11 shows the

Figure 7.11 Cooling and warming curves for measurements of C&A+3Mg low conductivity cryoprotectant solution at 1300MHz.

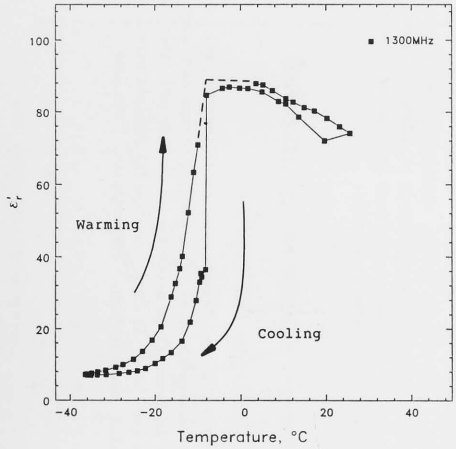

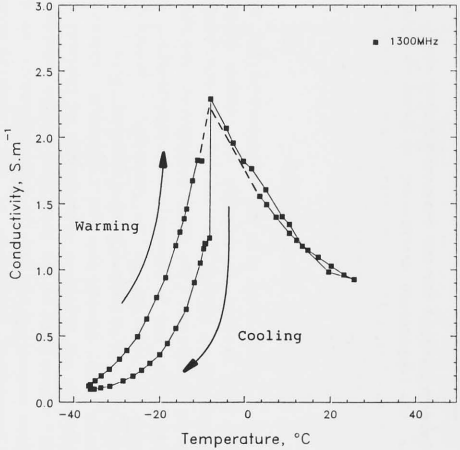

permittivity and effective conductivity of C&A+3Mg cryoprotectant solution; both the cooling curve and the warming curves are shown at 1300MHz.

Above the phase transition, there is relatively good agreement between the two curves, however there is a significant discrepancy below the phase transition. This discrepancy may be caused by a non-uniform temperature distribution in the liquid/solid under test as it is cooled/warmed. Figure 6.6 shows the measurement geometry. When the cryoprotectant is liquid, it is lossy, and the field at the probe tip is sharply confined. Conversely, when the cryoprotectant is frozen, the probe effectively 'sees' further into the solid mass. During cooling the probe measures the dielectric properties of the lossy liquid, close to where the temperature is measured by the thermocouple. Warming proceeds from the bottom of the beaker upwards; because the material at the top is frozen, the probe 'sees' lossier material below which is at a higher temperature than the material surrounding the thermocouple. Thus the warming curve is displaced to apparently lower temperatures.

Clearly, further experiments are required to investigate this effect, for example, a linear array of thermocouples could be used to investigate the temperature distribution. The measurements of all the cryoprotectant solutions were repeated at least twice, with little variation in the results obtained for the cooling curves. Nevertheless, it is clear that better temperature control is required, particularly below the phase transition. A significant constraint on the design of the cooling system is the need to avoid bringing cooling pipes too close to the probe tip.

4.2. Measurements Using the Strip-Line Sample Holder

All the measurements presented here were performed using the open-ended probe, since the measurements made with the strip-line sample holder were much less accurate, and covered a narrower temperature range. However, the results obtained were broadly similar, and the correlation between the dielectric properties of the perfused tissue and the cryoprotectant first noted with the

Figure 7.12 Electrical properties of C&A+3Mg low conductivity cryoprotectant solution, de-embedded using the non-linear admittance model with methanol as an additional reference.

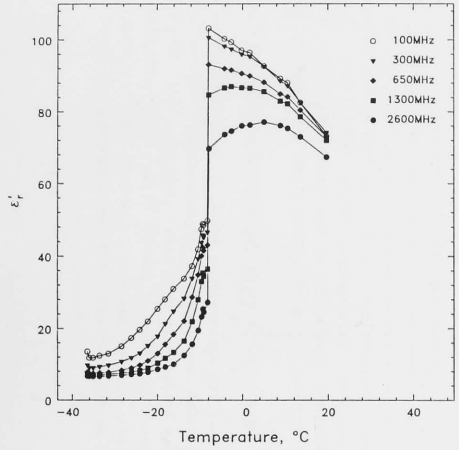

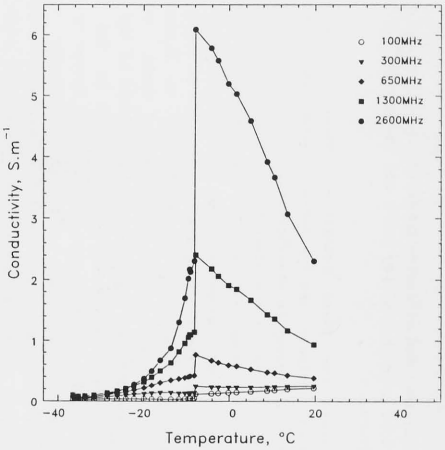

time domain system.

4.3. Biological Variation

The measurements presented of the electrical properties of perfused tissue are each from a single measurement of one kidney from two different animals (of the same strain). Consequently no estimate of the effects of biological variation can be made, nor the effect of position within the tissue on the measured dielectric properties. However, the fact that the measurements on both perfused tissue and plain cryoprotectants are so similar in form suggests that this source of non-systematic error may not be too serious.

4.4. Admittance Models

The linear admittance model was used for all the measurements on perfused tissue and cryoprotectants presented here, except for those on the MS+DMSO cryoprotectant solution. Reference materials used were short circuit, air and 100mM saline, with an additional reference of methanol for MS+DMSO. This was because the techniques for dealing with the non-linear model were not developed until close to the end of the experimental programme. As noted in chapter 6, all that is required are recordings of four rather than three reference materials; irritatingly this was not anticipated.

Fortunately, the effect of this omission does not seem to be too serious. An additional reference material (methanol) was recorded when the C&A+3Mg cryoprotectant was being measured. Figure 7.12 shows the dielectric properties of C&A+3Mg evaluated using the non-linear admittance model, which can be compared with Figure 7.9 which used the linear model.

5. Design of a Practical Rapid Rewarming System

In designing a rapid warming system for cryopreserved organs, there are essentially two interrelated choices to make. First,

what frequency is to be used, and second, what form of applicator should be used to transfer power to the tissue ? Both of the choices depend entirely on the dielectric properties of the material to be warmed.

5.1. Choice of Operating Frequency

The results presented in this chapter show that rapid warming at frequencies greater than 1300MHz is unlikely to be successful with the cryoprotectant solutions that have been investigated. This is basically because of the shallowness of the power penetration depth, and the drastic change of the effective conductivity across the phase transition. At low frequencies, the effective conductivity of the tissue becomes dominated by dc conductive loss, which has a positive temperature coefficient - even above the phase transition.

Exactly what constitutes a 'low' frequency depends on how far the dc conductivity of the tissue can be reduced. Using the C&A+3Mg cryoprotectant we have developed, it appears that the temperature coefficient of dielectric loss above the phase transition can be made negative, even at frequencies as low as 300MHz. The other advantage of going to lower frequencies is that the penetration depth can be made much greater than the smallest dimensions of the organ, ensuring uniform power deposition.

There is also a practical constraint on the choice of frequency for warming which concerns the availability of powerful microwave sources. There are a set of distinct frequencies, allocated by international agreement for industrial, scientific and medical (ISM) purposes. Now, providing the apparatus can be completely shielded, which can be arranged for any organ warming system, then any frequency can be used. However, RF power sources that operate at or near one of the ISM frequencies are generally cheaper and easier to obtain, so the ISM frequencies are of considerable practical interest. In the frequency range 10MHz to 5GHz, the ISM frequencies allocated in Europe, Africa, the Middle East and Russia are as follows: 13.6MHz, 27.1MHz, 40.7MHz, 434MHz and 2.45GHz. In the UK, additional frequencies are allocated:

42MHz, 49MHz, 56MHz, 61MHz, 66MHz, 84MHz, 168MHz, and 896MHz (Metaxas and Meredith 1983; p281-282).

So, from the point of view of uniformity of power deposition and the negative temperature coefficient in perfused tissue, it appears that 434MHz is a suitable frequency to use. As to cost, this may not be so favourable - most UK industrial microwave heating plants use either 27.12MHz, 896MHz or 2450MHz.

5.2. Choice of Applicator Geometry

This is a much more difficult decision, since the power deposition, in all but the most trivial cases, depends in a complex way upon both real and imaginary parts of the permittivity (see chapter 2). This will be the subject of further investigation; clearly much can be learned from the techniques used in hyperthermia treatment of tumours, and in industrial heating of foodstuffs.

One significant problem will be to ensure adequate shielding of the applicator from the operator. The ANSI recommended* safety limits at 434MHz are 1.4mW/cm^2 equivalent plane-wave power density, and 0.4W/kg specific absorption rate. However, there is a body of experimental evidence that suggests that biological effects can be elicited by pulsed electromagnetic fields orders of magnitude below this level (Adey 1981, Lerner 1984). Thus it is likely that a totally enclosed applicator geometry will be needed.

6. Conclusions and Suggestions for Further Work

6.1. Rapid Organ Rewarming

The central reason for making the dielectric measurements described in this dissertation is to provide the technology for rapid and uniform rewarming of cryopreserved organs. As suggested

* American National Standards Institute:
ANSI C95.1-1982

in the previous section, 434MHz seems the most promising frequency to use, for a several reasons, but applicator design will be an important factor in the success of a rapid warming system.

A further difficulty implicit in the use of electromagnetic techniques is that of temperature measurement during rewarming. It is unlikely that metallic thermocouples can be used, and more recent technologies such as optical fibre sensors may be more suitable.

6.2. Dielectric Measurements with an Open-Ended Probe

Clearly, the measurement techniques described in this dissertation are not limited to cryoprotectants. The open-ended probe has already been used on a range of biological materials, and we hope the simple direct de-embedding technique will further extend the areas of its application.

Although the linear admittance model offers approximate results very quickly, it would be useful to find a more accurate equivalent circuit model for the open-ended probe admittance by calculating the fields at the end of the probe.

6.3. Further Measurements

First, some of the problems described in this chapter must be addressed i.e. the effects of biological variation and the differences between the cooling and warming curves. It is also possible that the dielectric properties of the tissue may vary significantly with position. It would also be extremely useful to make simultaneous thermal property measurements (see Appendix 1).

If a higher capacity refrigerator were available so that rapid cooling and warming could be produced, measurements could be made on vitrified cryoprotectants, which is currently an area of great interest in cryobiology. Indeed, electromagnetic heating is thought to be the only practical way to devitrify a large tissue mass, such as an organ.

Before attempting rapid rewarming experiments on real organs, it is likely that some work will be needed on organ phantoms i.e. physical models of the organ to be rewarmed with similar electrical properties. Dielectric measurements will need to be made on this phantom material to ensure that the electrical properties are similar over the temperature range.

6.4. Instrumentation

It would be useful to decrease the measurement time, particularly if measurements are to be made on vitrified materials. Apart from hardware and software improvements, this can be achieved by recording fewer points from a narrower bandwidth with a frequency domain Network Analyzer. Alternatively, the time domain version can be used, this has the advantage that only one recording need be made at each temperature (as opposed to both magnitude and phase).

A dedicated high performance microcomputer, which would allow fast data processing, would be extremely useful for both these measurement systems in order to improve the turnround time between making a measurement and seeing the result.

References

Adam S F: "Microwave Theory and Applications", 1969
Englewood Cliffs: Prentice-Hall

Adam S F: "Automated Microwave Network Measurements",
IEEE Proc. **66**(4), Apr 1978, p384-391

Adey W R: "Tissue Interactions with Nonionizing Electromagnetic Fields",
Physiological Reviews, **61**, Apr 1981, p435-514

Anderson L S: "Analysis of an Open-Ended Coaxial Line Sensor in Inhomogeneous Dielectrics",
MSc Thesis, University of Ottowa, Canada 1984. BLLD: 85/25893

Andrews J R: "Automatic Network Measurements in the Time Domain",
IEEE Proc. **66**(4), Apr 1978, p414-423

Ashwood-Smith M J: "Low Temperature Preservation of Cells, Tissues and Organs", in "Low Temperature Preservation in Medicine and Biology", Ashwood-Smith M J and Farrant J (eds.), 1980, pp19-44
Tunbridge Wells: Pitman Medical Ltd.

Athey T W, Stuchly M A and Stuchly S S: "Measurement of Radio Frequency Permittivity of Biological Tissues with an Open-Ended Coaxial Line: Part I",
IEEE Trans. **MTT-30**(1), Jan 1982, p82-86

Bahl I J and Stuchly S S: "Effect of Finite Size of Ground Plane on the Impedance of a Monopole Immersed in a Lossy Medium",
IEE Electron. Lett. **15**(22), Oct 1979, p728-729

Balasubramaniam T A and Bowman H F: "Thermal Conductivity and Thermal Diffusivity of Biomaterials: A Simultaneous Measurement Technique",
ASME Trans. J. Biomech. Eng. **99**, Aug 1977, p148-154

Bamber J C and Hill C R: "Ultrasonic Attenuation and Propagation Speed in Mammalian Tissues as a Function of Temperature",
Ultrasound in Med. and Biol. **5**, 1979, p149-157

Bauer R F and Penfield P: "De-Embedding and Unterminating",
IEEE Trans. **MTT-22**(3), Mar 1974, p282-288

Bengtsson N E and Ohlsson T: "Microwave Heating in the Food Industry",
IEEE Proc. **62**(1), Jan 1974, p44-55

Bennett C L and Ross G F: "Time-Domain Electromagnetics and Its Applications",
IEEE Proc. **66**(3), Mar 1978, p299-318

Brady M M, Symons S A and Stuchly S S: "Dielectric Behaviour of Selected Animal Tissues in vitro at Frequencies from 2 to 4GHz",
IEEE Trans. **BME-28**(3), Mar 1981, p305-307

Burdette E C and Karow A M Jr.: "Kidney Model for Study of Electromagnetic Thawing",
Cryobiology **15**, 1978a, p142-151

Burdette E C, Karow A M and Jeske A H: "Design, Development and Performance of an Electromagnetic Illumination System for Thawing Cryopreserved Kidneys of Rabbits and Dogs",
Cryobiology **15**, 1978b, p152-167

Burdette E C, Cain F L and Seals J: "In Vivo Probe Measurement Technique for Determining Dielectric properties at VHF Through Microwave Frequencies",
IEEE Trans. **MTT-28**(4), Apr 1980a, p414-427

Burdette E C, Wiggins S, Brown R and Karow A M Jr.: "Microwave Thawing of Frozen Kidneys: A Theoretically Based Experimentally Effective Design",
Cryobiology **17**, 1980b, p393-402

Burdette E C: "Engineering Considerations in Hypothermic and Cryogenic Preservation", in "Organ Preservation for Transplantation", Karow A M and Pegg D E (eds.), 2nd Ed., pp213-259, 1981
New York: Marcel Dekker

Burdette E C: Private communication, Jul 1984

Bussey H E: "Dielectric Measurements in a Shielded Open Circuit Coaxial Line",
IEEE Trans. **IM-29**(2), Jun 1980, p120-124

Carslaw H S and Jaeger J C: "Conduction of Heat in Solids", 2nd Ed., 1959, pp53-56
Oxford: Clarendon Press

Cochrane P: "Sampling Principles" and "Sampling Systems" in "Microwave Measurements", Bailey A E (ed.), 1985, pp223-263
London: Peter Peregrinus

Christensen G C: "The Urogenital Apparatus", in "Miller's Anatomy of the Dog", Evans and Christensen (eds.), 1979, pp544-554
Philadelphia: Saunders

Coffey A K and Andrews P M: "Ultrastructure of Kidney Preservation: Varying the Amount of an Effective Osmotic Agent in Isotonic and Hypertonic Preservation Solutions",
Transplantation **35**(2), Feb 1983, p136-143

Cruzan O R and Garver R V: "Characteristic Impedance of Rectangular Coaxial Transmission Lines", IEEE Trans. **MTT-12**, Sep 1964, p488-495

Davidson D W and Cole R H: "Dielectric Relaxation in Glycerol, Propylene Glycol, and n-Propanol", J. Chem. Phys. **19**(12), 1951, p1484-1490

Dawkins A W J, Sheppard R J and Grant E H: "An on-line computer-based system for performing time domain spectroscopy I. Main features of the basic system", J. Phys. E: Sci. Instrum. **12**, 1979, p1091-1099

Dawkins A W J, Sheppard R J and Grant E H: "An on-line computer-based system for performing time domain spectroscopy II. Analysis of the errors in total reflection TDS", J. Phys. E: Sci. Instrum. **14**, 1981a, p1260-1265

Dawkins A W J, Sheppard R J and Grant E H: "An on-line computer-based system for performing time domain spectroscopy III. Presentation of results for total reflection TDS", J. Phys. E: Sci. Instrum. **14**, 1981b, p1429-1434

Dawkins A W J, Gabriel C, Sheppard R J and Grant E H: "Electrical properties of lens material at microwave frequencies", Phys. Med. Biol., **26**(1), 1981c, p1-9

Deschamps G A: "Impedance of an Antenna in a Conducting Medium", IRE Trans. **AP-10**(5), Sep 1962, p648-650

Edwards P H: "Radio Frequency Measurements on Liquid Dielectrics at Low Temperatures", EST Project Report, CUED 1982

Electricity Council: "Microwave Meat Tempering Recovers Costs in Six Months", Dielectric Heating Case History, leaflet EC 4212/7.81, 1981

Fahy G M and Hirsch A: "Prospects for Organ Preservation by Vitrification", in "Organ Preservation: Basic and Applied Aspects", Pegg D E, Jacobsen I A and Halasz N A (eds.), 1982, pp399-404 Lancaster: MTP Press

Fahy G M, MacFarlane D R, Angell C A and Meryman H T: "Vitrification as an Approach to Cryopreservation", Cryobiology **21**, 1984, p407-426

Farrant J: "General Observations on Cell Preservation", in "Low Temperature Preservation in Medicine and Biology", Ashwood-Smith M J and Farrant J (eds.), 1980, pp1-18 Tunbridge Wells: Pitman Medical Ltd.

Fellner-Feldegg H: "A Thin-Sample Method for the Measurement of Permeability, Permittivity, and Conductivity in the Frequency and Time Domain",
J. Phys. Chem. **76**(15), 1972, p2116-2122

Fessenden P, Lee E R, Anderson T L, Strohbehn J W, Meyer J L, Samulski T V and Marmor J B: "Experience with a Multitransducer Ultrasound System for Localized Hyperthermia of Deep Tissues",
IEEE Trans. **BME-31**(1), Jan 1984, p126-135

Field R F: "II. Dielectric Measuring Techniques: A. Permittivity: 1. Lumped Circuits", in "Dielectric Materials and Applications", Von Hippel A R (ed.), 1954, pp47-62
New York: Wiley & MIT Press

Gajda G and Stuchly S S: "Numerical Analysis of Open-Ended Coaxial Lines",
IEEE Trans. **MTT-31**(5), May 1983, p380-384

Garg S K and Smyth C P: "Microwave Absorption and Molecular Structure in Liquids. LXII. The Three Dielectric Dispersion Regions of the Normal Primary Alcohols."
J. Phys. Chem. **69**(4), Apr 1965, p1294-1301

Grant E H, Sheppard R J and South G P: "Dielectric Behaviour of Biological Molecules in Solution", 1978
Oxford: Clarendon Press

Guttman F M, Lizin J, Robitaille P, Blanchard H and Turgeon-Knaack C: "Survival of Canine Kidneys after Treatment with Dimethyl-sulfoxide, Freezing at -80°C, and Thawing by Microwave Illumination",
Cryobiology **14**, 1977, p559-567

Guttman F M, Segal N and Borzone J: "Cryopreservation of Canine Kidneys with Dimethylsulphoxide: Further Studies", in "Organ Preservation II", Pegg D E and Jacobsen I A (eds.), 1979, pp185-199
Edinburgh: Churchill Livingstone

Guttman F M, Bosisio R G, Bolongo D, Segal N and Borzone J: "Microwave Illumination for Thawing Frozen Canine Kidneys: (A) Assessment of Two Ovens by Direct Measurement and Thermography. (B) The Use of Effective Dielectric Temperature to Monitor Change during Microwave Thawing",
Cryobiology **17**, 1980, p465-472

Hallett J: "Nucleation and Growth of Ice Crystals in Water and Biological Systems", in "Low Temperature Biology of Foodstuffs", Hawthorn J and Rolfe E J (eds.), 1968, pp23-52
Oxford: Pergamon Press

Hasted J B: "Aqueous Dielectrics", 1973
London: Chapman and Hall Ltd.

Hearn A C: "REDUCE 2 User's Manual (2nd Ed.)", 1974
University of Utah, Salt Lake City, Utah 84112, USA

Hessary M and Chen K-M: "EM Local Heating with HF Electric Fields",
IEEE Trans. **MTT-32**(6), Jun 1984, p569-576

Hewlett-Packard: "Semi-Automatic RF Network Measurements using the HP8754A Network Analyzer and the HP9825A desk top computer",
Hewlett-Packard AN 294, Nov 1979

Hollinshead W H: "Anatomy for Surgeons: Volume 2", 1971, 2nd Ed., pp518-536
New York: Harper and Row

Hurt W D: "Multiterm Debye Dispersion Relations for Permittivity of Muscle",
IEEE Trans. **BME-32**(1), Jan 1985, p60-64

Jacobsen I A, Pegg D E, Wusteman M C and Robinson S M: "Transplantation of Rabbit Kidneys Perfused with Glycerol Solutions at 10°C",
Cryobiology **15**, 1978, pp18-26

Jacobsen I A and Pegg D E: "Cryopreservation of Organs: A Review",
Cryobiology **21**, 1984a, p377-384

Jacobsen I A, Pegg D E, Starklint H, Chemnitz J, Hunt C, Barfort P and Diaper M P: "Effect of Cooling and Warming Rate on Glycerolized Rabbit Kidneys",
Cryobiology **21**, 1984b, p637-653

Jonscher A K: "Dielectric Relaxation in Solids", 1983
London: Chelsea Dielectrics Press Ltd.

Jordan B P, Sheppard R J and Szwarnowski S: "The Dielectric Properties of Formamide, Ethanediol and Methanol",
J. Phys D: Appl. Phys. **11**, 1978, p695-701

Karow A M: "Problems of Organ Cryopreservation", in "Organ Preservation for Transplantation", Karow A M and Pegg D E (eds.), 2nd Ed., 1981, pp213-259
New York: Marcel Dekker

Ketterer F, Holst H I and Lehr H B: "Microwave Thawing of Frozen Organs", in "Organ Preservation II", Pegg D E and Jacobsen I A (eds.), 1979, pp200-206
Edinburgh: Churchill Livingstone

Kraszewski A, Stuchly S S, Stuchly M A and Symons S A: "On the Measurement Accuracy of the Tissue Permittivity In Vivo",
IEEE Trans. **IM-32**(1), Mar 1983a, p37-42

Kraszewski A, Stuchly M A and Stuchly S S: "ANA Calibration Method for Measurements of Dielectric Properties", IEEE Trans. **IM-32**(2), Jun 1983b, p385-387

Lawinski C P, Shepherd J C W and Grant E H: "Measurement of Permittivity of Solution of Small Biological Molecules at Radiowave and Microwave Frequencies", J. Microwave Power **10**(2), 1975, p147-162

Lerner E J: "Biological Effects of Electromagnetic Fields", IEEE Spectrum Magazine, May 1984, p57-69

Levine H and Papas C H: "Theory of the Circular Diffraction Antenna", J. Appl. Phys. **22**(1), Jan 1951, p29-43

Ligthart L P: "A Fast Computational Technique for Accurate Permittivity Determination Using Transmission Line Methods", IEEE Trans. **MTT-31**(3), Mar 1983, p249-254

Lorrain P and Corson D R: "Electromagnetic Fields and Waves", 2nd Ed., 1970
San Francisco: W H Freeman and Co.

McGrath J J: "Editorial", Cryo-Letters **6**, 1985, p211-213

Macklis J D and Ketterer F D: "Microwave Properties of Cryoprotectants", Cryobiology **15**, 1975, p627-635

Macklis J D, Ketterer F D and Cravalho E G: "Temperature Dependence of the Microwave Properties of Aqueous Solutions of Ethylene Glycol Between +15°C and -70°C", Cryobiology **16**, 1979, p272-286

Marcuvitz N (ed.): "The Waveguide Handbook", 1951, pp213-216
MIT Radiation Laboratory & McGraw-Hill

McDuffie G E Jr., Quinn R G and Litovitz T A: "Dielectric Properties of Glycerol-Water Mixtures", J. Chem. Phys. **37**(2), Jul 1962, p239-242

McDuffie G E Jr. and Litovitz T A: "Dielectric Relaxation in Associated Liquids", J. Chem. Phys. **37**(8), Oct 1962, p1699-1705

Meffert H F Th: "History, Aims, Results and Future of Thermophysical Properties Work within COST 90", in "Physical Properties of Foods", Jowitt R, Escher F, Hallström B, Meffert H F Th, Spiess W E L and Voss G (eds.), 1983, pp229-267
Barking: Applied Science Publishers Ltd.

Mellor J D: "Critical Evaluation of Thermophysical Properties of Foodstuffs and Outline of Future Developments", in Jowitt et al. ibid., pp331-353

Metaxas A C and Meredith R J: "Industrial Microwave Heating", 1983 London: Peter Peregrinus

Miles C A, van Beek G, Veerkamp C H: "Calculation of Thermophysical Properties of Foods", in Jowitt et al. ibid., pp269-312

Mosig J R, Besson J-C E, Gex-Fabry M and Gardiol F E: "Reflection of an Open-Ended Coaxial Line and Application to Nondestructive Measurement of Materials", IEEE Trans. **IM-30**(1), Mar 1981, p46-51

Mudgett R E, Mudgett D R, Goldblith S A, Wang D I C, and Westphal W B: "Dielectric Properties of Frozen Meats", J. Microwave Power **14**(3), 1979, p209-216

Nevels R D, Butler C M and Yablon W: "The Annular Slot Antenna In a Lossy Biological Medium", IEEE Trans. **MTT-33**(4), Apr 1985, p314-319

Newnham P D: "Broadband Dielectric Measurements", EST Project Report, CUED 1985

Nicolson A M and Ross G F: "Measurement of the Intrinsic Properties of Materials by Time-Domain Techniques", IEEE Trans. **IM-19**(4), Nov 1970, p377-382

Nicolson A M, Bennett C L, Lamensdorf D and Susman L: "Applications of Time-Domain Metrology to the Automation of Broad-Band Microwave Measurements", IEEE Trans. **MTT-20**(1), Jan 1972, p3-9

Pegg D E: "Close Tolerance Cooling Apparatus for Cryobiological Studies", Laboratory Practice, Jul 1966

Pegg D E, Green C J and Walter C A: "Attempted Canine Renal Cryopreservation Using Dimethyl Sulphoxide, Helium Perfusion and Microwave Thawing", Cryobiology **15**, 1978, p618-626

Pegg D E: "The Effect of Cell Concentration on the Recovery of Human Erythrocytes after Freezing and Thawing in the Presence of Glycerol", Cryobiology **18**, 1981, p221-228

Pegg D E and Jacobsen I A: "Current Status of Cryopreservation of Whole Organs with Particular Reference to the Kidney", in "Renal Preservation", Marberger M and Dreikorm K (eds.), Vol. 8 of International Perspectives in Urology, 1983, pp301-322
Baltimore: Williams & Wilkins

Pegg D E, Diaper M P, Skaer H LeB and Hunt J C: "The Effect of Cooling Rate and Warming Rate on the Packing Effect in Human Erythrocytes Frozen and Thawed in the Presence of 2M Glycerol",
Cryobiology **21**, 1984, p491-502

Rall W F and Fahy G M: "Ice-free Cryopreservation of Mouse Embryos at -196C by Vitrification",
Nature **313**, No. 6003, 14th Feb 1985, p573-575

Ramo S, Whinnery J R and Van Duzer T: "Fields and Waves in Communications Electronics", 1965
New York: John Wiley

Reader H C: "Time Domain Techniques for Antenna Analysis", Ph.D Thesis, University of Cambridge, Oct 1985

Rigg P R and Carroll J E: "Low-cost computer-based time-domain microwave network analyser",
IEE Proc. Pt.H **127**(2), Apr 1980, p107-111

Rubinsky B, Cravalho E G and Mikic B: "Thermal Stresses in Frozen Organs",
Cryobiology **17**, 1980, p66-73

Rubinsky B and Cravalho E G: "Transient Mass Transfer Processes during the Perfusion of a Biological Organ with a Cryophylactic Agent Solution",
Cryobiology **19**, 1982, p70-82

Schwan H P, Sheppard R J and Grant E H: "Complex Permittivity of Water at 25°C"
J. Chem. Phys. **64**(5), Mar 1976, p2257-2258

Sealectro Ltd.: "Tool Kit T1849 Instruction Manual", Sealectro Ltd., Portsmouth UK, 1984, Section 1, p1-4

Sells R A, Macpherson S and Salaman J R: "Assessment of Resources for Renal Transplantation in the United Kingdom",
The Lancet, 27th Jul 1985, p195-197

Smith A U: "Biological Effects of Freezing and Supercooling", 1961
London: Edward Arnold

Smith G S and Nordgard J D: "Measurement of the Electrical Constitutive Parameters of Materials Using Antennas",
IEEE Trans. **AP-33**(7), Jul 1985, p783-792

Southard J H and Belzer F O: "Principles of Renal Preservation for Transplantation", in "Renal Preservation", Marberger M and Dreikorm K (eds.), Vol. 8 of International Perspectives in Urology, 1983, pp188-210
Baltimore: Williams & Wilkins

Stauffer P R, Cetas T C and Jones R C: "Magnetic Induction Heating of Ferromagnetic Implants for Inducing Localized Hyperthermia in Deep-Seated Tumors",
IEEE Trans. **BME-31**(2), Feb 1984, p235-251

Stogryn A: "Equations for Calculating the Dielectric Constant of Saline Water",
IEEE Trans. **MTT-19**, Aug 1971, p733-736
[Note: The correct version of equation (6) is on p45 of Grant et al. ibid.]

Stuchly M A and Stuchly S S: "Coaxial Line Reflection Methods for Measuring Dielectric Properties of Biological Substances at Radio and Microwave Frequencies - A Review",
IEEE Trans. **IM-29**(3), Sep 1980, p176-183

Stuchly M A, Athey T W, Samaras G M and Taylor G E: "Measurement of Radio Frequency Permittivity of Biological Tissues with an Open-Ended Coaxial Line: Part II",
IEEE Trans. **MTT-30**(1), Jan 1982a, p87-92

Stuchly M A, Brady M M, Stuchly S S and Gajda G: "Equivalent Circuit of an Open-Ended Coaxial Line in a Lossy Dielectric",
IEEE Trans. **IM-31**(2), Jun 1982b, p116-119

Stuchly M A and Stuchly S S: "Permittivity of mammalian tissues in vivo and in vitro. Advances in experimental techniques and recent results",
Intl. J. Electronics **56**(4), 1984, p443-456

Stuchly S S, Stuchly M A and Carraro B: "Permittivity Measurements in a Resonator Terminated by an Infinite Sample",
IEEE Trans. **IM-27**(4), Dec 1978, p436-439

Stuchly S S: Private communication, Jul 1984

Tanabe E and Joines W T: "A Nondestructive Method for Measuring the Complex Permittivity of Dielectric Materials at Microwave Frequencies Using an Open Transmission Line Resonator",
IEEE Trans. **IM-25**(3), Sep 1976, p222-226

Tran V N, Stuchly S S and Kraszewski A: "Dielectric Properties of Selected Vegetables and Fruits 0.1-10.0GHz",
J. Microwave Power **19**(4), 1984, p251-258

Valvano J W, Allen J T, and Bowman H F: "The Simultaneous Measurement of Thermal Conductivity, Thermal Diffusivity, and Perfusion in Small Volumes of Tissue",
ASME Trans. J. Biomech. Eng. **106**, Aug 1984, p192-197

Van Gemert M J C: "Evaluation of Dielectric Permittivity and Conductivity by Time Domain Spectroscopy. Mathematical Analysis of Fellner-Feldegg's Thin Cell Method", J. Chem. Phys. **60**(10), May 1974, p3963-3974

Von Hippel A R (ed.): "Dielectric Materials and Applications", 1954
New York: Wiley & MIT Press

Von Hippel A R: "The Dielectric Relaxation Spectra of Water, Ice and Aqueous Solutions and Their Interpretation. I. Critical Survey of the Status Quo for Water", Technical report No. 1, Contract N00014-67A-0204-0003, Apr 1967, p3
Cambridge: MIT, Laboratory for Insulation Research.

Von Hippel A R: "The Dielectric Relaxation Spectra of Water, Ice, and Aqueous Solutions and Their Interpretation. III. Proton Organization and Proton Transfer in Ice", Technical report No. 3, Contract N00014-67A-0204-0003, Jan 1968, p8
Cambridge: MIT, Laboratory for Insulation Research.

Voss W A G, Rajotte R V and Dossetor J B: "Applications of Microwave Thawing to the Recovery of Deep Frozen Cells and Organs: A Review", J. Microwave Power **9**(3), 1974, p181-194

Westphal W B: "II. Dielectric Measuring Techniques: A. Permittivity: 2. Distributed Circuits", in "Dielectric Materials and Applications", Von Hippel A R (ed.), 1954, pp63-122
New York: Wiley & MIT Press

Whinnery J R and Jamieson H W: "Equivalent Circuits for Discontinuities in Transmission Lines", Proc. IRE **32**, Feb 1944, p98-114

Appendix 1

Thermal Relaxation and Thermal Runaway

This appendix describes some of the heat transfer phenomena which are relevant to organ warming. We investigate thermal relaxation and thermal runaway analytically, and examine the solutions using thermal property data for water and for meat.

1. Heat Transfer by Thermal Conduction

In principle at least, convective, conductive and radiative heat transfer mechanisms can all be used to transfer heat to the exterior of an organ. Electromagnetic energy can be used to deposit energy throughout; nevertheless, the dominant mechanism of heat transfer inside a frozen organ is thermal conduction.

1.1. The Conduction Equation

Consider a volume of material, V, with a temperature distribution $T(\underline{x},t)$, physical properties k, ρ and c_p, and complex conductivity σ^+, which is exposed to an electric field $\underline{E}(\omega,\underline{x})$ with time dependence $\exp j\omega t$. Here, k is the thermal conductivity, ρ is the density, c_p is the specific heat capacity at constant pressure, ω is the angular frequency, and $\underline{x}$ is a general position coordinate inside the volume.

One of the difficulties in modelling organ warming is that the thermal properties and the electrical conductivity are all functions of temperature, physical state, and to a lesser extent, position. Figure A1.1 shows the variation of k and c_p with temperature for a typical foodstuff; Table A1.1 in section 1.3 gives values of k, ρ and c_p for pure water and for meat at five temperatures. Because the the electrical properties change with temperature, it means that $\underline{E}$ is also a function of temperature. To make the problem tractable, we make some simplifying assumptions:

Figure A1.1 Thermal conductivity (a) and thermal diffusivity (b) of foodstuffs around the freezing point. After Meffert (1983).

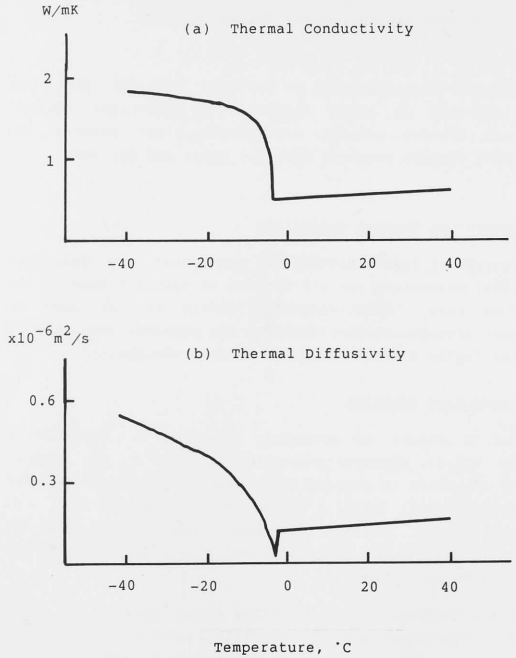

a) The thermal properties k, and c_p, and the density ρ are all independent of position in V, and independent of temperature. Also, we shall not attempt to use the model around the frozen/thawed phase transition, although we note in passing that the transition ice I -> water requires 333.6kJ/kg.

b) The electrical properties, represented by σ^+, are independent of position and temperature in V.

c) $\underline{E}$ is uniform throughout V, and is independent of σ^+.

With these assumptions, the heat conduction equation is

$$\nabla^2 T + \frac{1}{k} P = \frac{1}{\alpha} \frac{\partial T}{\partial t} \qquad \text{(A1.01)}$$

where $\alpha = k/\rho c_p$ is the thermal diffusivity, $P = \sigma |\underline{E}|^2$ is the power dissipated by the electric field, and $\sigma = \mathrm{Re}\sigma^+$ is the effective conductivity at frequency ω.

In the absence of any spatial variation of the temperature distribution, the temperature of the whole volume increases uniformly from the initial temperature T_o, with warming rate $W = \alpha P/k$. So, we substitute

$$T(\underline{x},t) = \Delta T.\theta(\underline{x},t) + T_o + Wt \qquad \text{(A1.02)}$$

into (A1.01) where $\theta(\underline{x},t)$ represents the departure from the spatially uniform warming, and ΔT is a constant to obtain

$$\nabla^2 \theta = \frac{1}{\alpha} \frac{\partial \theta}{\partial t} \qquad \text{(A1.03)}$$

Clearly, α controls how quickly a given spatial temperature distribution changes.

1.2. Thermal Relaxation of a Spherical Discontinuity

Before we can get much further with the analysis, we must introduce a specific set of boundary conditions. As an example, suppose that some small spherical sub-volume of V is initially at a temperature ΔT higher than the rest of V at temperature T. We assume that the radius of the sub-volume, a, is much smaller than

Figure A1.2 (a) Boundary condition on $\theta(r,t)$ at $t=0$.

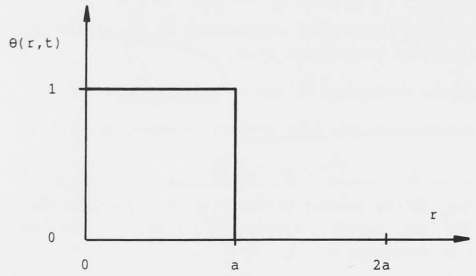

(b) Boundary condition on $u(r',t')$ at $t'=0$.

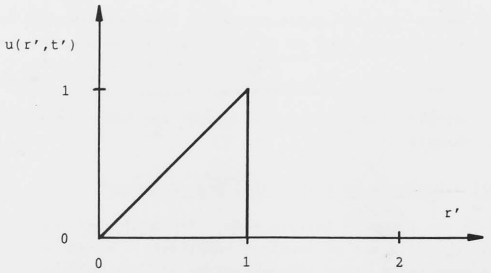

the dimensions of V, so that we may treat V as infinite. Because of the spherical symmetry, we need only work with a single radial coordinate so that (A1.05) becomes

$$\frac{\partial^2\theta}{\partial r^2} + \frac{2}{r}\frac{\partial\theta}{\partial r} = \frac{1}{\alpha}\frac{\partial\theta}{\partial t} \qquad \text{(A1.04)}$$

The boundary condition associated with (A1.04) is shown in Figure A1.2a. Substitute $\theta = u/r$, and normalize r and t so that $r' = r/a$ and $t' = \alpha t/a^2$ to obtain

$$\frac{\partial^2 u}{\partial r'^2} = \frac{\partial u}{\partial t'} \qquad \text{(A1.05)}$$

Analytical methods of solution for (A1.05) with the transformed boundary conditions shown in Figure A1.2b are available (Carslaw and Jaeger 1959); the solution to (A1.04) is

$$\theta(r,t) = \frac{1}{2}\left[\ \text{erf}\ \frac{1 - r'}{2\sqrt{t'}} + \text{erf}\ \frac{1 + r'}{2\sqrt{t'}}\ \right]$$

$$+ \frac{\sqrt{t'}}{r'\sqrt{\pi}}\left[\ \exp\frac{-(1 + r')^2}{4t'} - \exp\frac{-(1 - r')^2}{4t'}\ \right] \qquad \text{(A1.06)}$$

Note that in this equation, and in the remainder of this appendix, we use primes to indicate normalization i.e. $r' = r/a$, and $t' = \alpha t/a^2$. Figure A1.3 shows this normalized temperature distribution plotted at successive instants in time, showing how the initial temperature distribution decays. A useful way to interpret these curves is to note that the time taken for the temperature at the centre of the discontinuity to fall to 50% of its initial value is $t_{50} \simeq 0.2a^2/\alpha$. This gives an idea of how quickly heat can be transferred in the organ.

1.3. Numerical Examples

Little, if any, thermal property data is available for tissue which has been perfused with cryoprotectant over a range of temperatures. Techniques for making such measurements are available; one which has been used on biological materials uses a small thermistor as a sensing element to obtain both k and α (Valvano *et al.* 1984). In the absence of suitable data, we

Figure A1.3 Thermal relaxation of a spatial discontinuity. The temperature distribution is plotted at successive instants in a 1-2-5 sequence, t′ = 0, 0.01, 0.02 .. 2.0, 5.0

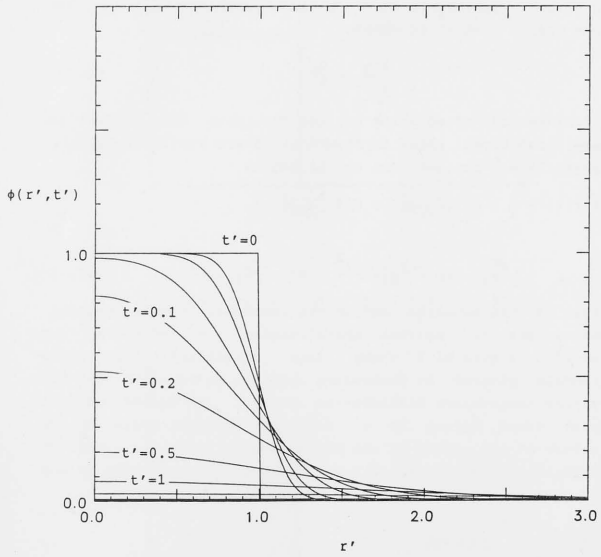

examine two materials for which data is available - water and meat (beef) whose thermal properties are listed in Table A1.1 below.

Table A1.1
Thermal Properties of Ice, Water and Meat

Material	Temperature °C	Conductivity W/mK	Diffusivity $x10^{-6} m^2/s$
Ice I[a]	-40	2.7	1.6
	-20	2.5	1.4
	-10	2.4	1.3
	0	2.2	1.2
Water[a]	0	0.55	0.13
	+10	0.57	0.14
	+20	0.59	0.14
	+40	0.65	0.16
Beef[a,b]	-10	1.1	0.30
	+10	0.45	0.13

Notes: 1. Density of ice taken as $917^{a} kg/m^3$
2. Density of beef taken as $974^{a,b} kg/m^3$

Sources: a) Miles et al. (1983), b) Mellor et al. (1983)

1.3.1. Example 1: Thermal Relaxation in Water and Ice

If we take values of α for water from Table A1.1 for ice I and liquid water at 0°C, we obtain

$$\frac{t_{50}|_{\text{Ice}}}{t_{50}|_{\text{Water}}} = 9.1$$

Thus any discontinuity disappears about nine times faster in ice than in water by conduction mechanisms.

1.3.2. Example 2: Thermal Relaxation in Meat

Beef freezes at about -1.1°C; we compare t_{50} at -10°C and +10°C using data from Table A1.1

$$\frac{t_{50}\,|\,-10^{\circ}C}{t_{50}\,|\,+10^{\circ}C} = 2.4$$

so that it appears that water provides a more pessimistic estimate of the difference in relaxation rates.

If we take a = 5mm, which is the approximate dimension of macroscopic structures in renal tissue, and use the value of α for beef at +10°C, then t_{50} is about 40 seconds. If our warming rate is, say 120K/min i.e. 2K/s, then the effect of thermal relaxation will be insignificant for such large discontinuities which means that we must ensure that power deposition in the tissue is as uniform as possible.

1.3.3. Cryoprotectants

There is little data on the thermal properties of cryoprotectant solutions; however, the thermal properties of pure associated liquids (which are the basis of many cryoprotectants) are known, at least near 20°C. The thermal diffusivity and conductivity of Glycerol, Ethanediol and Propanediol are given in Table A1.2. These show no marked difference from the properties of water alone.

2. Thermal Runaway

Thermal runaway occurs when the amount of energy absorbed by a material increases with temperature. If the increase in energy absorption with temperature is not too great, thermal runaway can be stabilized by thermal relaxation. This section presents a simple analytical model for thermal runaway, and shows how thermal relaxation affects the process.

2.1. Formulation of the model

The same method as the previous section is used, except that assumption b) is relaxed so that the dissipated power in the tissue volume is a function of temperature. The power dissipated

Table A1.2
Thermal Properties of Associated Liquids

Material	Conductivity W/mK	Diffusivity $x10^{-6} m^2/s$
Glycerol[a]	0.29	0.11
Ethanediol[a]	0.25	0.10
Propanediol[b]	0.20	-

Sources: a) Balasubramaniam and Bowman (1977).
Values are for 21°C.
b) CRC Handbook of Chemistry and Physics (61st Ed.).
Value for 20°C given.

per unit volume is $P(T)=\sigma(T)|\underline{E}|^2$, and we use a Taylor series around the initial temperature T_o to linearize P(T) i.e.

$$P_L(T) = P(T_o) + (T-T_o)\frac{\partial P}{\partial T}\Big|_{T_o} \qquad \text{(A1.07a)}$$

which is written

$$P_L(T) = \frac{kW_o}{\alpha}\,[\,1 + (T-T_o)\beta\,] \qquad \text{(A1.07b)}$$

where $W_o = \alpha P(T_o)/k$, and

$$\beta = \frac{1}{P(T_o)}\,\frac{\partial P}{\partial T}\Big|_{T_o} = \frac{1}{\sigma(T_o)}\,\frac{\partial \sigma}{\partial T}\Big|_{T_o} \qquad \text{(A1.08)}$$

is the temperature coefficient of the absorbed power. If $\underline{E}$ is uniform, β is also the temperature coefficient of the effective conductivity. Equation (A1.01) becomes

$$\nabla^2 T + \frac{\beta W_o}{\alpha}\,T + \frac{W_o}{\alpha}(1 - \beta T_o) = \frac{1}{\alpha}\,\frac{\partial T}{\partial t} \qquad \text{(A1.09)}$$

Figure A1.4 Spatial and temporal evolution of a discontinuous temperature distribution where power absorption increases with increasing temperature ($\beta W_o = 1$)

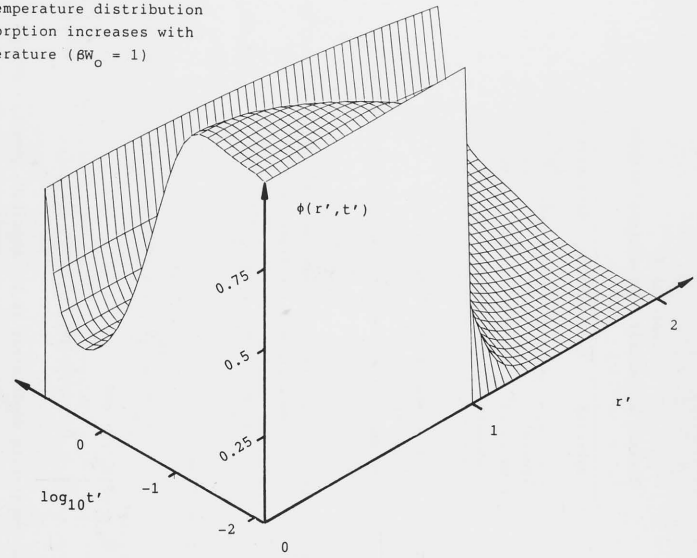

2.2. Analytical Solution

The expression analogous to (A1.02) is

$$T(\underline{x},t) = \Delta T.\phi(\underline{x},t) + T_o + \frac{1}{\beta}(\exp\beta W_o t - 1) \qquad (A1.10)$$

hence W_o is the initial warming rate of the bulk of the material. Substituting (A1.10) into (A1.09) yields

$$\nabla^2\phi + \frac{\beta W_o}{\alpha}\phi = \frac{1}{\alpha}\frac{\partial\phi}{\partial t} \qquad (A1.11)$$

With the same spherically symmetric geometry, boundary conditions, and normalization for r and t used in section 1, (A1.11) becomes

$$\frac{\partial^2\phi}{\partial r'^2} + \frac{2}{r'}\frac{\partial\phi}{\partial r'} + \frac{\beta W_o a^2}{\alpha}\phi = \frac{\partial\phi}{\partial t'} \qquad (A1.12)$$

If we make a change of variable so that $\phi = (u.\exp\beta W_o t)/r'$ then (A1.12) becomes (A1.05) (with the same boundary conditions), hence the solution to (A1.12) is

$$\phi(r,t) = \theta(r,t)\exp\beta W_o t \qquad (A1.13)$$

2.3. Investigation of the Solution

Figure A1.4 shows the spatial and temporal evolution of a discontinuity for the case $\beta W_o = 1$. The diagram shows that the temperature at the centre of the discontinuity initially begins to rise, then thermal relaxation appears to remove the discontinuity. After a longer period the temperature appears to increase without limit.

2.3.1. Behaviour for Large t

The form of ϕ, the normalized temperature of the discontinuity, is quite complex, and it is useful to obtain an approximate analytic form for the normalized temperature at the centre of the discontinuity valid for large t. From (A1.06)

$$\theta(0,t) = \lim_{r\to 0}\theta(r,t) = \operatorname{erf}\frac{1}{2\sqrt{t'}} - \frac{1}{\sqrt{\pi t'}}\exp\frac{-1}{4t'} \qquad (A1.14)$$

so for large t

$$\phi(0,t) \rightarrow \frac{\exp\beta W_o t}{6t'\sqrt{\pi t'}} \qquad \text{(A1.15)}$$

The case $\beta \leq 0$, is unconditionally stable; the relaxation of the discontinuity is accelerated by a factor $\exp\beta W_o t$. For $\beta > 0$, (A1.15) shows that the discontinuity grows without limit as $t \rightarrow \infty$, despite the effect of thermal relaxation.

2.3.2. Behaviour for Intermediate Values of t

The purpose of the model is to show how the value of β affects the evolution of the initial temperature distribution. Clearly $\beta < 0$ is preferable, but if this cannot be achieved, it is useful to know at what value of $\beta > 0$ thermal runaway overcomes thermal relaxation.

2.3.3. Warming Time, and Warming Stability

Suppose we are trying to warm an organ from temperature T_o to T_h. This will take t_h seconds, where

$$t_h = \frac{1}{\beta W_o} \ln[1 + (T_h - T_o)\beta] \qquad \text{(A1.16)}$$

At time t_h the temperature at the centre of the discontinuity is $T_h + \Delta T.\phi(0,t_h)$ where

$$\phi(0,t_h) = [\ \text{erf}\ \frac{1}{2\sqrt{t'_h}} - \frac{1}{\sqrt{\pi t'_h}} \exp\ \frac{-1}{4t'_h}\ ].[1 + (T_h - T_o)\beta] \qquad \text{(A1.17)}$$

If thawing is 'stable', then $\phi(0,t_h) < 1$, so one possible stability condition is of the form $\beta < \beta_{crit}$ where β_{crit} is the smallest positive root of f such that

$$f(\beta) = \phi(0,t_h) - 1 = 0 \qquad \text{(A1.18)}$$

This is a transcendental equation, which must be solved numerically or graphically. The next section, investigates the solution of (A1.18) for a set of numerical parameters which

Figure A1.5 Final temperature profile of an initially rectangular discontinuity (radius 5mm) after the bulk of the material has been warmed through 40K with an initial warming rate of 120K/min (2K/s).
The curves correspond to a 1-2-5 sequence of values of β in /K, the temperature coefficient of the absorbed power. For small β, thermal relaxation dominates, for larger β, thermal runaway dominates.
Material properties used correspond to those of raw beef at +10°C i.e. $\alpha = 0.13 \times 10^{-6}$ms, and k = 0.45W/mK.

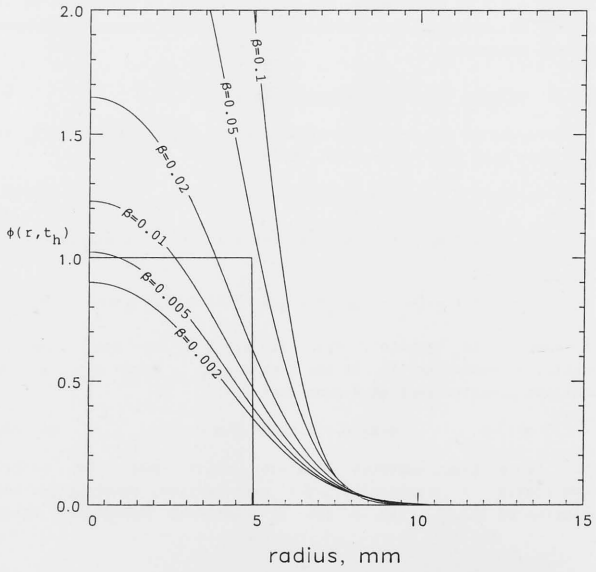

Figure A1.6 Final temperature at the centre of an initially rectangular discontinuity, plotted against the temperature coefficient β.
One possible stability criterion, which is illustrated here, is the 'net zero growth' condition i.e. the temperature at the centre of the discontinuity should be less than or equal to the initial temperature. The diagram shows that for $\beta \leq 0.004/K$ warming is stable by this criterion.
Material properties and warming conditions as Figure A1.5.

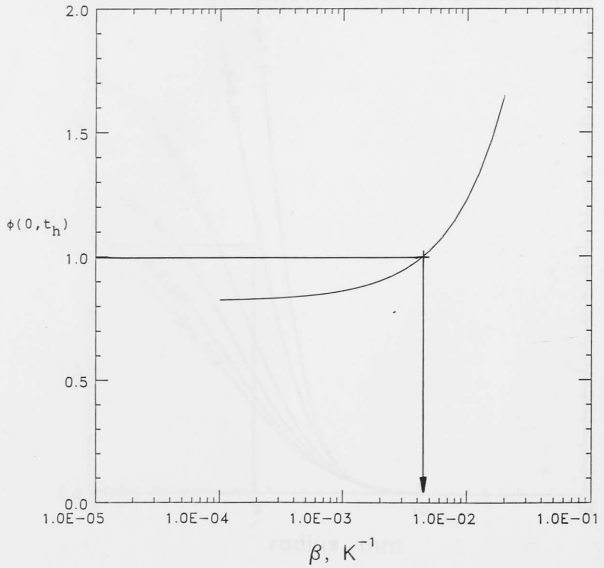

provide a pessimistic model of organ warming.

2.3.4. Example 3: Thermal Runaway and Thermal Relaxation

This example investigates the effect of β on the resulting temperature distribution after warming through a specific temperature interval with a given warming rate using thermal property data from Table A1.1.

Take $\alpha = 0.13 \times 10^{-6} m^2/s$ and $k = 0.45 W/mK$ which are the values for beef at +10°C; $T_h - T_o = 40K$; initial warming rate $W_o = 2K/s$ (120K/min); and $a = 5mm$ as before. This value of W_o corresponds to an input power of about 700W into a organ volume of 100ml. Figure A1.5 shows the shape of the discontinuity at time t_h for a range of values of β. Figure A1.6 is a plot of (A1.17), the temperature at the centre of the discontinuity evaluated at $t = t_h$, against β. This plot allows us to solve (A1.18) numerically; from the curve, $\beta_{crit} = 0.004/K$, so for $\beta < 0.004/K$, the discontinuity is stable, higher values of β are unstable according to this stability criterion.

3. Conclusions

Thermal relaxation is controlled by a material property known as the thermal diffusivity, or α. Published values of α for beef suggest that the diffusivity reduces by a factor of about 2.4 as the material thaws.

Thermal runaway generally occurs when the amount of energy absorbed by a material increases with temperature. However, if the increase in energy absorption with temperature is not too great, thermal runaway can be stabilized by thermal relaxation.

There is a need for measurements of the thermal conductivity and diffusivity concomitant with measurements of the electrical properties of perfused, frozen tissue.

Appendix 2

Inventory of Materials

This appendix is essentially a list of the materials used in this work. Section 1 lists the parameters used to generate the dielectric dispersions of reference materials i.e. materials with known dielectric properties. Section 2 gives the physical properties of glycerol and dimethyl sulphoxide (DMSO) and the 'recipes' for the cryoprotectant solutions investigated in this work.

1. Dielectric Reference Materials

1.1. Dispersion functions for Dielectric Measurements

Dielectric measurements in the literature are generally fitted to an appropriate empirical dispersion function.

1.1.1. Debye Dispersion

An n-term Debye dispersion (see chapter 2) is denoted by

$$\varepsilon_r^+ = \varepsilon_\infty + \sum_{i=1}^{n} \frac{\Delta_i}{1 + j\omega\tau_i} \qquad \text{(A2.1)}$$

where ε_∞ is the high frequency permittivity, Δ_i is the dielectric decrement associated with the time constant τ_i, and ω is the angular frequency. A useful special case of (A2.1) is a single Debye dispersion with an additional term to represent the effect of the dc conductivity

$$\varepsilon_r^+ = \varepsilon_\infty + \frac{\varepsilon_s - \varepsilon_\infty}{1 + j\omega\tau} + \frac{\sigma_{dc}}{j\omega\varepsilon_o} \qquad \text{(A2.2)}$$

where ε_s is the static permittivity, σ_{dc} is the dc conductivity,

and ε_o is the permittivity of free space.

1.1.2. Cole-Cole and Cole-Davidson Dispersion Functions

The Cole-Cole dispersion function is

$$\varepsilon_r = \varepsilon_\infty + \frac{\varepsilon_s - \varepsilon_\infty}{1 + (j\omega\tau)^{1-\alpha_{cc}}} \qquad \text{(A2.3)}$$

and the Cole-Davidson dispersion function is

$$\varepsilon_r = \varepsilon_\infty + \frac{\varepsilon_s - \varepsilon_\infty}{(1 + j\omega\tau)^{\beta_{cd}}} \qquad \text{(A2.4)}$$

1.2. Dielectric Properties of Reference Materials

1.2.1. Saline over a range of temperatures and concentrations

Stogryn published formulae to interpolate a large number of dielectric measurements on sodium chloride solutions (Stogryn 1971). The dispersion is represented by a single Debye term together with a dc conductivity term as in (A2.2). The parameters of the dispersion depend on the temperature, and on the sodium chloride concentration. Stogryn takes $\varepsilon_\infty = 4.9$ to be constant; ε_s and τ at temperature θ°C and sodium chloride normality N are given by

$$\varepsilon_s(\theta,N) = \varepsilon_s(\theta,0)a(N) \qquad \text{(A2.5a)}$$

$$\tau(\theta,N) = \tau(\theta,0)b(N,\theta) \qquad \text{(A2.5b)}$$

with a and b given by

$$a(N) = 1.000 - 0.2551N + 51.51\times10^{-3}N^2 - 6.889\times10^{-3}N^3 \qquad \text{(A2.5c)}$$

$$b(N,\theta) = 1.000 - 48.96\times10^{-3}N - 29.67\times10^{-3}N^2 + 5.644\times10^{-3}N^3 + 1.463\times10^{-3}N\theta \qquad \text{(A2.5d)}$$

and $\varepsilon_s(\theta,0)$ given by

$$\varepsilon_s(\theta,0) = 87.74 - 0.400080\theta + 0.9398\times10^{-3}\theta^2 - 1.410\times10^{-6}\theta^3 \qquad \text{(A2.5e)}$$

This is an expression due to Malmberg and Maryott (Hasted 1973; p37), although Stogryn (1971) does not correctly reproduce the signs of the terms (which are correct above). The relaxation time $\tau(\theta,0)$ is

$$2\pi\tau(\theta,0) = 111.09\times10^{-12} - 3.824\times10^{-12}\theta + 69.38\times10^{-15}\theta^2 - 509.6\times10^{-18}\theta^3 \qquad \text{(A2.5f)}$$

Stogryn gives two expressions for the conductivity $\sigma(\theta,N)$; one is for sea water, the other is more appropriate here

$$\sigma(\theta,N) = \sigma(25,N)c(\theta-25,N) \qquad \text{(A2.5g)}$$

where

$$\sigma(25,N) = N[\ 10.394 - 2.3776N + 0.68258N^2 - 0.13538N^3 + 10.086\times10^{-3}N^4\ ] \qquad \text{(A2.5h)}$$

and

$$c(\Delta,N) = 1.000 + 19.62\times10^{-3}\Delta + 80.8\times10^{-6}\Delta^2 + \Delta N[\ 30.20\times10^{-6} - 39.22\times10^{-6}\Delta + N(\ 17.21\times10^{-6} + 6.584\times10^{-6}\Delta\ )\ ] \qquad \text{(A2.5i)}$$

1.2.2. 100mM Saline at 20°C

From the Stogryn formula (Stogryn 1971). Saline is modelled by a single term Debye dispersion with $\varepsilon_\infty = 4.9$, $\varepsilon_s = 78.10$, $\tau = 9.225$ps and a conductivity term, $\sigma = 0.9185 Sm^{-1}$

1.2.3. Methanol (Methyl Alcohol) at 20°C

Cole-Cole dispersion from Jordan et al. (1978) with

ε_s = 34.8±0.5, ε_∞ = 4.5±0.7, τ = 56±2ps, α = 0.044±0.027

1.2.4. Ethanediol (Ethylene Glycol) at 20°C

From Jordan et al. (1978). Two term Debye dispersion with ε_∞ = 3.8±0.5; Δ_1 = 35.5±0.8, τ_1 = 145±3ps; Δ_2 = 3.5±1.0, τ_2 = 10±4ps.

2. Cryoprotectant Solutions

2.1. Physical Properties of Cryoprotectants

The following table shows physical property data for Glycerol [$HO.CH_2CH(OH)CH_2OH$], and Dimethyl Sulphoxide [$(CH_3)_2SO_2$] taken from the 61st edition of the CRC Handbook of Chemistry and Physics.

Table A2.1

Physical Properties of Glycerol and DMSO

Material	mw g	bp °C	mp °C	density kgm^{-3}	n_D
Glycerol	92.11	290	20	1261	1.4746
DMSO	78.13	189	18.4	1101.4	1.4770

2.2. HP6 + 3M Glycerol Cryoprotectant Solution

This glycerol based cryoprotectant has been used extensively in this work (referred to as HP6 + 3M glycerol or HP6+3Mg). Table A2.2 below gives the recipe, and Table A2.3 the composition of this cryoprotectant.

Haemaccel (Hoechst UK) is a plasma volume substitute, and contains other anions and cations - the final composition is shown in

Table A2.2

Recipe for HP6 with
3M Glycerol Cryoprotectant Solution

Compound	
NaCl	2.075g
KCl	5.775g
$NaHCO_3$	1.008g
MgS047H2	0.493g
Glycerol	276.27g
Haemaccel	500ml
Water	to 1 litre

Table A2.3. The final pH should be 7.4.

2.3. Modified Sachs + 1.4M DMSO Cryoprotectant Solution

This cryopreservation solution, referred to as 'MS+DMSO', was used by Guttman et al. (1977) in their successful cryopreservation experiments with dog kidney. The table below is taken from Pegg et al. (1978) who, after much consultation with Guttman, attempted to repeat his experiments.

2.4. Low Conductivity 3M Glycerol Cryoprotectant Solution

This is an experimental cryopreservation solution in which the majority of the electrolytes are removed and replaced with a sugar - in this case sucrose. This has the advantage of reducing the dc conductivity; successful successful hypothermic preservation experiments published by Coffey and Andrews (1983) (see chapter 7) suggest that it may also be better biomedically. In the text, this solution is referred to as 'C&A+3Mg'.

Table A2.3

Composition of HP6 with
3M Glycerol Cryoprotectant Solution

Cations	Na^+	120mM
	K^+	81mM
	Mg^{2+}	2mM
	Ca^{2+}	3mM
Anions	Cl^-	186mM
	HCO_3^-	12mM
	SO_4^{2-}	2mM
	PO_4^{3-}	traces
Others	Glycerol	3M
	Polygeline	17.5g
	Water	to 1 litre

Table A2.4

Composition of Modified Sachs with
1.4M DMSO Cryoprotectant Solution

Cations	Na^+	15mM
	K^+	143mM
	Mg^{2+}	4mM
Anions	Cl^-	4mM
	HCO_3^-	38mM
	Phos.	120mM
Others	DMSO	1.4M
	Mannitol	25g
	Hydrocortisone	100mg
	Heparin	2000IU
	Isoproterenol	1mg
	Water	to 1 litre

Table A2.5

Composition of Experimental
3M Glycerol Cryoprotectant Solution

Cations	Na^+	50mM
Anions	Cl^-	50mM
Others	Glycerol	3M
	Sucrose	169.7mM
	Water	to 1 litre

Appendix 3

Digital Recorders for Time and Frequency Domain Measurement Systems

This appendix describes the digital recorder hardware and software used to make dielectric measurements using time domain and frequency domain instrumentation. Chapter 4 gives a brief description of the function of the sampling oscilloscope used for time domain measurements. Chapter 6 describes the relevant details of the network analyzer used for frequency domain measurements.

Although the operation and function of these two instruments is very different, essentially the same scheme has been used for recording the data from both of them. Two separate digital recorders were used, both of which were originally intended for use with sampling oscilloscopes. Although the recording technique is similar, the implementation is different, so the two are described separately in sections 1 and 2 respectively.

1. Time Domain Measurement System

1.1. Introduction

The system comprises a Tektronix 7000-series sampling oscilloscope, together with a purpose built digital recorder, known as 'Summing Recorder 2'. Chapter 4 describes the experimental layout used, and some of the relevant features of the sampling oscilloscope. This section is concerned with practical details of the digital recorder, which was built to our specifications by H L Lowe of the CUED electronics workshop.

Figure A3.1 Block diagram of the time domain digital recorder system - Summing Recorder 2.

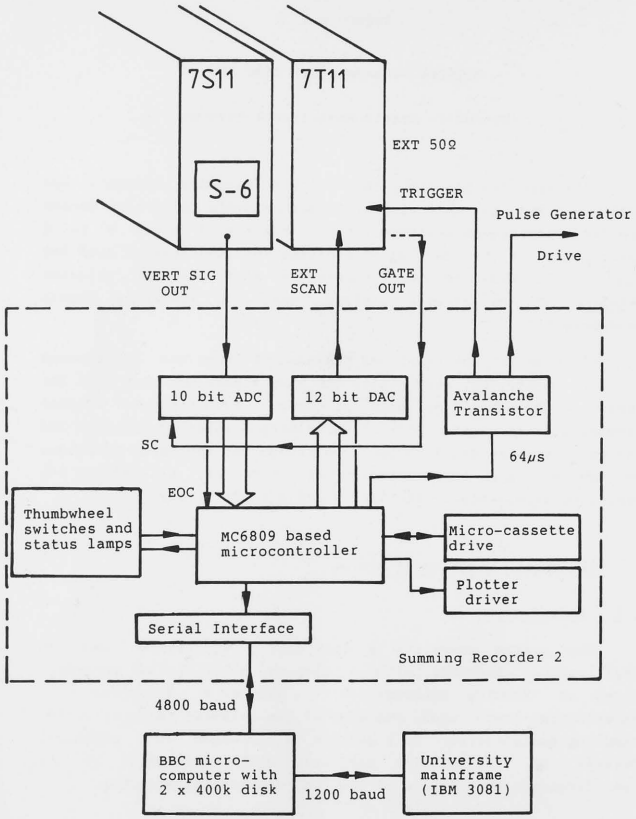

1.2. Sampling Oscilloscope System

The sampling oscilloscope system consists of a 7T11 sampling sweep unit and two 7S11 sampling units in a 7603 mainframe. This configuration allows two channel operation with a choice of either terminated (S-4) or 'loop-thru' (S-6) sampling heads, although only the S-6 has been used for this work.

The sampling oscilloscope constructs the displayed waveform by taking short duration (~20ps) samples of the fast, but necessarily repetitive input waveform at different part of the waveform with respect to the trigger event. The time at which the sample is taken is voltage controlled, normally this voltage is provided by an internal slow ramp generator, but this can be disconnected to allow external control of the sampling instant via the 'EXT SCAN' input jack on the 7T11 front panel (1V/div).

A small sample of charge is taken from the input waveform whilst the sampling gate in the S-6 is open. The output of the S-6 is amplified and stored by the 7S11 circuitry, and passed to the 7603 mainframe for display. The 7S11 provides a scaled version of the sampled input waveform on the 'VERT SIG OUT' jack (0.2V/div).

1.3. Digital Recorder Overview

1.3.1. Hardware

The recorder has the hardware and firmware to drive four devices - the sampling oscilloscope, an external XY pen recorder, a digital mini-cassette deck, and a standard full duplex RS232 serial line. Figure A3.1 is a block diagram of the system, showing the connections to the sampling oscilloscope. A single board microcontroller is used - based on a Motorola MC6809 microprocessor with 9K of RAM and 16K of EPROM.

1.3.2. Software

The recorder can be operated in 'local' or 'remote' mode. In 'local' mode it behaves as a stand-alone data recorder receiving its instructions from two thumbwheel switches on the front panel. In 'remote' mode it can be controlled via the RS232 serial interface, communicating with either a dumb terminal or a more intelligent host. To allow data collection remote from the laboratory, data may be recorded on a mini-cassette, using the digital tape recorder. Normally the recorder is used in 'remote' mode with a BBC microcomputer host. This approach has the advantage that the recorded data can be saved on floppy disk, also the rather primitive commands recognised by the recorder firmware can be enhanced or modified with little effort. The cassette recorder and plotter driver are rarely used in practice.

In principle, it would be possible to perform all our data processing on the BBC microcomputer. We have found it more convenient, for the same reasons as given in chapter 6, to transfer the data to the University mainframe - an IBM 3081 running Phoenix/MVS.

1.4. Sampling Oscilloscope Interface

1.4.1. Trigger Generator

The recorder contains an avalanche transistor pulse sharpener driven by a TTL divider from the 1MHz crystal-controlled microprocessor clock. This signal is used to provide a trigger both for the 7T11 timebase and for the pulse generator which provides the source waveform that is to be observed by the oscilloscope. The trigger runs continuously with a 64μs repetition period, without interference from any other circuit in the recorder. The 7T11 gives the best jitter performance (better than 10ps) when triggered repetitively in this way. Figure A3.2a is a timing diagram which shows the behaviour of the waveforms

Figure A3.2 Timing diagrams for time domain digital recorder system.

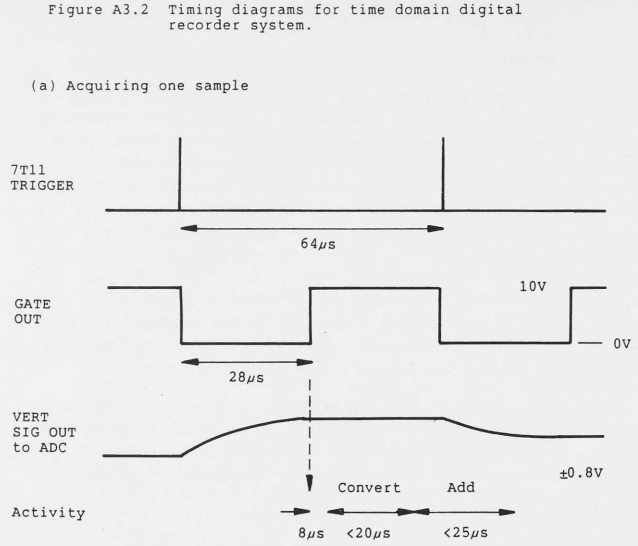

First four samples from ADC are discarded

discussed below after each trigger event.

1.4.2. Sampling the Vertical Signal

A 10-bit analogue to digital converter (ADC) is used to acquire data from the VERT SIG OUT of the 7S11. The signal provided at this output jack has settled to a constant level approximately 20μs after the trigger event, however this delay is not fixed and depends on the triggering conditions of the 7T11.

Now, the 7T11 provides a blanking signal to the 7603 mainframe which it uses to hide the spot on the display whilst the system is settling. This signal is brought out at the rear of the 7603 ('GATE OUT'). Between the trigger event and GATE OUT going high, small perturbations are present on the VERT SIG OUT signal, afterwards, for about 36μs, the 7S11 holds the sample level constant until the next trigger arrives. So, the recorder uses the GATE OUT signal to drive the 'Start Conversion' line of the ADC, which performs the conversion in about 20μs. The VERT SIG OUT signal is bipolar, so it is first passed through a carefully screened low noise preamplifier and level shifter before being presented to the unipolar ADC used here (ZN432).

The effect of noise in the sampling system can be reduced by signal averaging. In this implementation, the recorder moves to each time point in turn, forming the average of the samples acquired before moving on, so that only one scan of the time window is performed. Each 10-bit sample is accumulated in a 24-bit pseudo-register in the microcontroller, the arithmetic takes less than 25μs. The recorder can take up to 8192 samples at each time point, although this can be selected from 1, 2, 4, .. 8192 in multiples of 2. The average is formed by right-shifting the 24-bit result down to 12 bits, so although a 10-bit ADC is used, a 12-bit result is stored.

1.4.3. External Scan

The scan signal is generated under software control by an RS7542 12-bit digital to analogue converter (DAC) buffered by a

low noise preamplifier. Up to 4096 points may be digitized, though any of 4096, 2048, 1024, 512 or 256 may be selected from the time window. After each time step, the 7T11 has to be allowed about 0.3ms to settle, this is achieved by discarding the first 4 samples acquired after incrementing the DAC voltage, as is shown in Figure A3.2b.

1.5. Data Transfer

After all of the samples have been taken, the recorder stores them in its local memory, until it is requested to transmit the data to its host. In order to provide the most flexible format possible, the data is encoded into ASCII text i.e. the ADC value $010000111010_2 = 43A_{16}$ is transmitted as the characters '4' '3' 'A'. The samples are sent via the 4800 baud serial link to the BBC microcomputer in fixed length records, consisting of 16 sample values followed by a modulo 4096 checksum. There, a header containing a user supplied title and a representation of the vertical and horizontal settings is prepended, and the entire file saved onto floppy disk. After the end of an experimental run, the set of files is transferred from the floppy disk to the University mainframe via a 1200 baud serial link connected to the University data network (UDN). Figure A3.3 below shows the data format for a single time domain recording. The final row contains column checksums.

Figure A3.3 Time Domain Digital Recorder Data Record

```
May 1985  SSCOPE 2, SREC 2, HEAD 6
Scene on line, showing incident pulse + reflecti-
ons                                          .
N 1024, NQ 12, NSUM  1024, VDIV 1.000E-01, TDIV 5.000E-09
F4FF4FF4FF4FF4FF50F50F50F50F50F50F50F50F50F50F504FB
.
.     (64 lines of data in total)
.
F4EF4EF4DF4DF4DF4DF4CF4CF4CF4DF4DF4DF4DF4DF4E4D0
B68CE7CF192250C47E879D35F9F10C1720B6F14BF19F19B0
```

2. Frequency Domain Measurement System

2.1. Introduction

Chapter 6 describes the function of the Hewlett-Packard 8754A Network Analyzer and associated instrumentation, this section describes the digital recorder hardware used to acquire data from the 8754A. As noted in the previous section, the digital recorder ('Summing Recorder 3') had been designed with the sampling oscilloscope in mind. Fortunately, the design was sufficiently flexible to allow reconfiguration to suit the 8754A. The reconfigured interface hardware, and the driving software is described below. The recorder was designed and built chiefly by W K Yeung in this department. Details of interfacing the 8754A to Hewlett-Packard computers is given in AN294 (Hewlett-Packard 1979) - this proved invaluable when writing the software described below.

2.2. Network Analyzer System

The 8754A consists of a swept RF source and a dual receiver system. The receiver can measure the magnitude and phase of the ratio between two signals derived from the RF source. When used with the 8502A reflection test set, the resulting configuration can measure both magnitude and phase of the reflection coefficient.

The 8754A source covers 4-1300MHz; for our measurements the frequency range was extended to 2600MHz using the 08754-60057 frequency doubler. The frequency of the source is voltage controlled - normally this is driven by an internal slow ramp generator, but by switching to REMOTE operation, the frequency can be programmed externally by a 0-10V signal fed into the rear panel EXT SWEEP INPUT jack.

The outputs from the receiver include voltages proportional to phase and logarithmic magnitude, these are processed by the display circuitry to present a trace on the CRT. The display circuitry also provides rear panel VERT and HORIZ output jacks

Figure A3.4 Block diagram of the frequency domain digital recorder system - Summing Recorder 3.

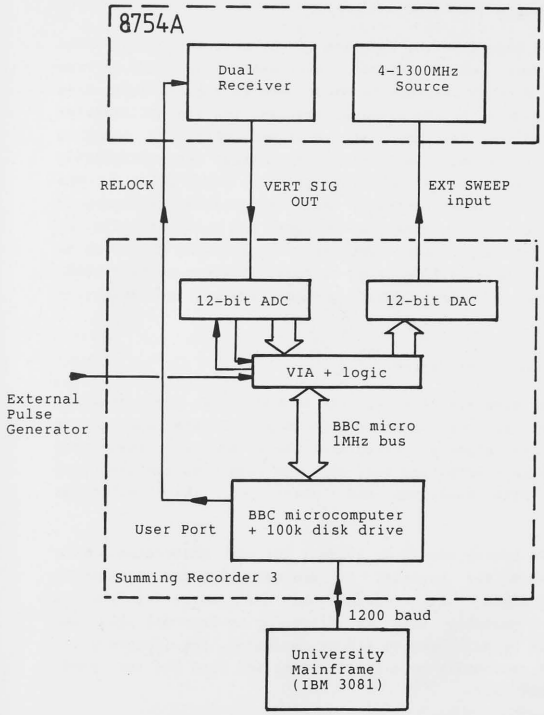

which effectively give an image of the displayed trace scaled to 100mV/div.

When operating in REMOTE mode over the whole frequency range available from the source, the receiver phase lock has to be relocked before moving to a new frequency; this requirement is explained in more detail in chapter 6. A rear panel programming connector is provided on the 8754A. Amongst other functions, the TTL compatible control inputs allow the initiation of a relock cycle for the receiver and the switching from LOCAL mode to REMOTE mode.

2.3. Digital Recorder Overview

2.3.1. Hardware

This interface is driven by a BBC microcomputer system which provides a user interface, and records the data taken from the NA on floppy disk. Rather than use a separate microprocessor to control the ADC and DAC, Summing Recorder 3 uses the BBC microcomputer itself for this task. This greatly improves the throughput - which is restricted in the other recorder by the speed of the serial line, although the maximum sampling rate achievable is a little lower, because of the more primitive architecture of the 6502 and the slower ADC. The other major advantage of this approach is flexibility - it is very much simpler to reconfigure Summing Recorder 3, since most of the functions are provided by software resident in the BBC micro address space. Figure A3.4 is a block diagram of the recorder showing the connections to the 8754A. The majority of the functional elements shown are on a single 100mm x 160mm Eurocard, which is a modified version of the board designed by N G Walker of this department.

The BBC micro 1MHz bus is used as the main channel of communication with the interface, sending control signals to both the ADC and the DAC and receiving data from the ADC. The interface board is buffered via a 6522 Versatile Interface Adapter (VIA), which provides the necessary latching and decoding

Figure A3.5 Timing diagram for the frequency domain digital recorder system.

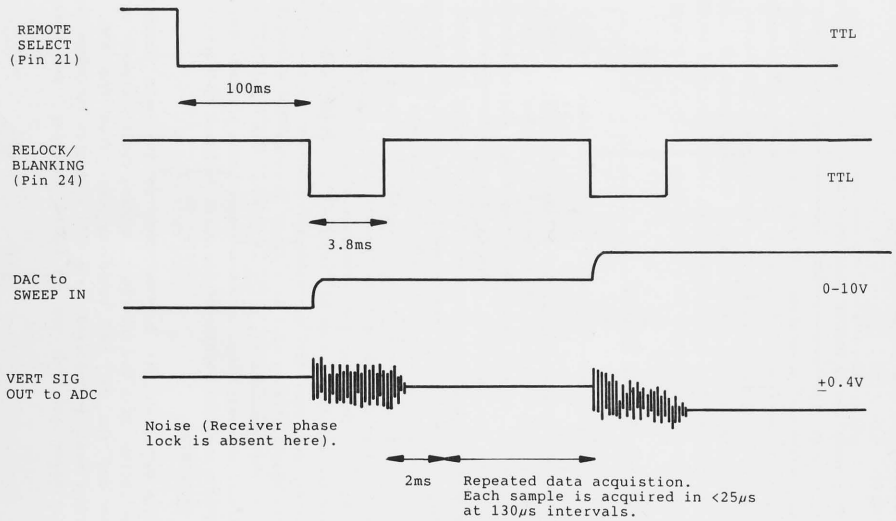

facilities needed, and a BEEBEX expansion board (Control Universal Limited). Other hardware is present on the Eurocard which is used to synchronize the timing of the ADC conversion with some external event (e.g. the GATE OUT signal from the sampling oscilloscope). This signal is merely provided by an external pulse generator in this application.

2.3.2. Software

The software that drives the recorder is split into two logically distinct sections: the user interface, written in BBC BASIC, and the low-level interface driver, written in 6502 Assembler. The hardware driver is called from the BASIC program in order to execute the various interface functions.

2.4. Network Analyzer Interface

2.4.1. Source Tuning and Receiver Outputs

The external tuning voltage for the 8754A is provided by a DAC1209 12-bit digital to analogue converter (DAC) under software control. The magnitude and phase outputs are sampled by an AD574 12-bit analogue to digital converter (ADC).

2.4.2. Sampling Algorithm

When instructed to record data from the 8754A, the hardware driver sets the DAC output to 0V, and the 8754A is switched from LOCAL to REMOTE mode. About 100ms is allowed for the system to settle. The sampling proceeds as follows (see Figure A3.5):

a) The CRT is blanked, by taking the RELOCK line from high to low, the DAC is selected, and the source (re)tuned by loading the DAC with an appropriate 12-bit number. About 3.8ms is allowed for the source plus DAC to settle. Next, the receiver PLL is instructed to relock, this sequence takes about 1.5ms and is initiated by taking the RELOCK line from low to high.

b) After a further 0.5ms, the ADC is selected, and a sample is

taken from the VERT SIG OUT voltage. In order to overcome the effects of system noise, many samples (typically 128) of this voltage are taken. The ADC takes 25μs to convert, meanwhile, the previous sample value, latched by the VIA, is fetched by the processor of the BBC micro and added into a temporary accumulator area. Each sampling cycle is completed in about 130μs.

c) After all the samples at a particular frequency have been taken, the average value is calculated and stored as a 12-bit number in ASCII hexadecimal. Control then returns to (a) unless all of the frequency points have been visited, in which case control is returned to the calling BASIC program.

After this procedure has been performed for both magnitude and phase the data, plus a five line header are written to floppy disk. The header contains information about the source and receiver settings together with a user supplied date and title to identify the data. The data format used is very similar to the time domain record given in section 1.

UNIVERSITY
LIBRARY
CAMBRIDGE